# Exploring the nature of fossil galaxy systems with simulations and X-ray observations

*by*

Alisha R. Kundert

A dissertation submitted in partial fulfillment of

the requirements for the degree of

Doctor of Philosophy

(Astronomy)

*at the*

University of Wisconsin–Madison

2018

Date of final oral examination: 25 May 2018

The dissertation is approved by the following members of the Final Oral Committee:
Elena D'Onghia, Assistant Professor, Astronomy
John S. Gallagher III, Professor, Astronomy
Dan McCammon, Professor, Physics
J. Alfonso L. Aguerri, Professor, Astronomy, Instituto de Astrofísica de Canarias

# Abstract

Fossil galaxy groups and clusters are characterized by an extreme difference in brightness between their central and satellite galaxies. This magnitude gap has been proposed to form as the result of significant mergers of massive satellite galaxies with the central galaxy over time which suggests fossils represent an interesting stage of galaxy system evolution and hierarchical structure formation. The objective of this thesis is to use X-ray observations and simulations to constrain the properties of fossil galaxy systems with the goal of understanding their nature and origin.

In this thesis, the properties of fossil systems are first examined by constructing the global optical and X-ray scaling relations of fossils across the group and cluster mass regimes. Then, using the Illustris cosmological simulation, the mass assembly histories of fossil central galaxies and their group halos are traced directly. Lastly, the X-ray properties of fossil system RX J1159.8+5531 are investigated in detail through radial profiles of intracluster medium temperature and density, which are used to determine the total mass profile and mass concentration parameter of this group. These studies point towards fossil systems as a temporary relaxed state in the evolution of galaxy groups and clusters.

# Acknowledgments

I am grateful to the many people who have helped and assisted in the development of this thesis work. Foremost thanks go to my advisor Elena D'Onghia for support and encouragement these past six years and for providing many opportunities to present and do research around the world. I am also thankful for the continued collaboration and guidance of Alfonso Aguerri since the beginning of my first thesis project. I would additionally like to thank Fabio Gastaldello for insightful discussions about X-ray astronomy and for being willing to answer my many questions about X-ray data analysis.

Thank you also to my friends at UW. To my classmates Emily, Erin, and David, thanks for your encouragement and optimism especially during tough times. To my research groupmates, Stephen and Tim, it has been wonderful working together - thanks for making group meetings so fun. Thanks also to my graduating cohort-mates, Ben and Anna, for helpful conversations during jobs meetings this final year. And thanks to my officemates, Diego and Yi-Hao, for a friendly working environment.

To Dad, Mom, Frederick, and Alexander, thanks for constantly cheering me on and motivating me to keep working hard. This thesis would not have been possible without you.

# Contents

Abstract . . . . . i

Acknowledgments . . . . . ii

Contents . . . . . iii

List of Tables . . . . . iv

List of Figures . . . . . v

**1 Introduction** **1**

1.1 Fossil galaxy system origin scenarios . . . . . 5

1.2 Overview of fossil galaxy system properties . . . . . 7

1.2.1 BCG properties . . . . . 7

1.2.2 Galaxy group scale properties . . . . . 9

1.3 Thesis outline . . . . . 11

References . . . . . 12

**2 Global X-ray scaling relations of fossil galaxy clusters** **15**

Abstract . . . . . 16

2.1 Introduction . . . . . 17

2.2 The Sample . . . . . 20

2.3 Observations and Data Reduction . . . . . 21

2.4 Treatment of non-ICM emission . . . . . 22

2.4.1 Background and foreground sources . . . . . 22
2.4.2 Solar wind charge exchange . . . . . 24
2.4.3 Point source contamination . . . . . 25
2.4.4 Implementation of RASS data . . . . . 26
2.5 Image Analysis . . . . . 26
2.5.1 Determination of the source aperture for the spectral analysis region 26
2.5.2 Surface brightness analysis . . . . . 28
2.6 Spectral Analysis . . . . . 31
2.6.1 Spectral fitting in the source region . . . . . 33
2.6.1.1 A soft energy excess . . . . . 34
2.6.2 Comparison and interpretation of the model fits . . . . . 35
2.7 Global ICM temperatures and luminosities . . . . . 36
2.8 Scaling Relations . . . . . 39
2.8.1 Sample assembly, correction, and fitting . . . . . 40
2.8.2 Comparison with previous studies . . . . . 45
2.9 Summary and conclusions . . . . . 46
2.10 Appendix: Testing FGS24 for SWCX contamination . . . . . 47
2.11 Appendix: Characterizing the Suzaku XRT PSF . . . . . 49
2.12 Appendix: Notes on the Sample . . . . . 51
References . . . . . 55

**3 Are fossil groups early-forming galaxy systems? 58**

Abstract . . . . . 59
3.1 Introduction . . . . . 60
3.2 The Illustris Simulation . . . . . 62

3.3 The Sample . . . 64
3.4 Results . . . 68
3.4.1 Evolution of the magnitude gap . . . 68
3.4.2 Properties of the BGG . . . 71
3.4.2.1 Scaling relations . . . 71
3.4.2.2 BGG stellar mass assembly history . . . 75
3.4.2.3 BGG merger history . . . 77
3.4.3 Group mass assembly history . . . 81
3.5 Discussion . . . 86
3.5.1 Comparison to other simulations . . . 86
3.5.2 Observational implications . . . 88
3.6 Summary and conclusions . . . 89
References . . . 92

**4 A mass modeling analysis of the fossil group RX J1159.8+5531 95**
Abstract . . . 96
4.1 Introduction . . . 97
4.2 Data analysis . . . 98
4.2.1 Data processing and calibration . . . 98
4.2.2 Imaging analysis . . . 99
4.2.3 Spectral analysis . . . 100
4.2.3.1 ICM model . . . 102
4.2.3.2 Photon background model . . . 102
4.2.3.3 Particle background model . . . 102
4.2.3.4 Fitting and deprojection . . . 103

4.2.4 Gas density profile . . . . . 103
4.2.4.1 Surface brightness counts to gas density . . . . . 103
4.2.4.2 Fitting the gas density profile . . . . . 105
4.3 Mass modeling . . . . . 106
4.3.1 The temperature model . . . . . 106
4.3.2 The total gravitating mass model . . . . . 107
4.3.2.1 Dark matter mass profile . . . . . 107
4.3.2.2 Stellar mass profile . . . . . 108
4.3.2.3 Gas mass profile . . . . . 109
4.3.3 MCMC . . . . . 110
4.4 Discussion . . . . . 111
4.4.1 $c - M$ relation . . . . . 111
4.4.2 A comparison of RX J1159.8+5531 studies . . . . . 113
4.4.3 The magnitude gap of RX J1159.8+5531 . . . . . 114
4.5 Summary and conclusions . . . . . 114
References . . . . . 115

**5 Summary and Conclusions** **117**

# List of Tables

2.1 Summary of Suzaku observations of fossil systems . . . . . 21
2.2 Properties of fossil systems observed with Suzaku . . . . . 29
2.3 Surface brightness profile model parameters . . . . . 31
2.4 Spectral analysis best-fitting model parameters . . . . . 37
2.5 Global properties of the ICM-dominated subsample of clusters. . . . . 39
2.6 Scaling relations . . . . . 44
2.7 FGS24: spectral model parameters during low proton flux interval . . . . . 48
2.8 Radial brightness profile of SS Cyg . . . . . 51

3.1 Illustris groups sample properties . . . . . 65
3.2 Mass assembly times of Illustris BGGs . . . . . 77
3.3 Mass assembly times of Illustris groups . . . . . 83

4.1 RX J1159.8+5531 observation properties . . . . . 99
4.2 RX J1159.8+5531 gas density model . . . . . 106
4.3 Central galaxy properties of RX J1159.8+5531 . . . . . 109
4.4 RX J1159.8+5531 total mass profile . . . . . 111
4.5 RX J1159.8+5531 extrapolated DM profile . . . . . 112

# List of Figures

1.1 Luminosity function of fossil group RX J1340.6+4018 . . . . . 3
1.2 X-ray and optical image of fossil cluster FGS26 . . . . . 4
1.3 Probability of obtaining a fossil group by chance . . . . . 5
1.4 Contribution of fossil BCGs to group optical luminosity . . . . . 8

2.1 Suzaku images of sample of fossil systems . . . . . 23
2.2 Surface brightness profiles of FGS30 . . . . . 30
2.3 Surface brightness profiles of the stacked XIS images . . . . . 32
2.4 Suzaku XIS spectra for sample of fossil systems . . . . . 38
2.5 Scaling relations of fossil and non-fossil systems . . . . . 43
2.6 The observed XIS1 light curve for FGS24 . . . . . 49
2.7 Radial brightness profile for point source SS Cyg . . . . . 50

3.1 Magnitude gap distribution for Illustris groups . . . . . 66
3.2 Evolution of the magnitude gap . . . . . 69
3.3 Distribution of BGGs' stellar masses, $r$-band magnitudes . . . . . 72
3.4 Stellar masses of BGGs compared to the $M_{200}$ masses of their groups . . . 73
3.5 Illustris $z = 0$ properties for BGGs . . . . . 74
3.6 Stellar mass assembly histories of central galaxies . . . . . 76

3.7 Number of major mergers experienced by BGGs . . . . . 78

3.8 Contribution of BGG stellar mass originating from mergers . . . . . 79

3.9 Group $M_{200}$ mass assembly histories of fossils and non-fossils . . . . . 82

3.10 Comparison of fossil and non-fossil group $z_{50}$ and $z_{80}$ assembly times . . . . 84

4.1 The inner $< 100$ kpc cluster core of RX J1159, X-ray and optical imaging . 100

4.2 Annular regions for spectral analysis of RX J1159.8+5531 . . . . . 101

4.3 RX J1159 mass modeling analysis - gas density, temperature, mass profiles 104

4.4 RX J1159.8+5531 and the $c - M$ relation . . . . . 112

# Chapter 1

# Introduction

In galaxy groups, galaxies merge over time to assemble luminous central elliptical galaxies. The mergers of the most massive satellite galaxies in a group are expected to occur in less than a Hubble time (Barnes 1989; Boylan-Kolchin et al. 2008), and these mergers act to progressively increase the mass and luminosity of a group's bright central galaxy (BCG). However, the dynamical friction timescale for the merging of the most massive group galaxies is shorter than the timescale for the X-ray bright intragroup gas to cool. Thus, galaxy groups that assemble their mass early and remain undisturbed are predicted to be observed at the present with an optical luminosity function dominated in the bright-end by an exceptionally luminous BCG (Fig. 1.1) that resides in the center of an extended group-size X-ray halo (Fig. 1.2). Galaxy systems with these properties were proposed to be named fossil groups, since their bright central elliptical galaxies are expected to form from the mergers of the previous group galaxy members (Ponman & Bertram 1993). And fossil groups have indeed been observed with the first fossil candidate, RX J1340.6+4018, found by Ponman et al. (1994) as an X-ray detected group where the bright central elliptical contributes the majority of the total group optical light and $L*$ satellite galaxies similar in luminosity to the Milky Way are missing (Jones et al. 2000).

Jones et al. (2003, hereafter J03) established the first observational definition of fossil systems with criteria for both their X-ray and optical properties. First, these systems must possess an extended X-ray halo of $L_{\rm X} \geq 10^{42} h_{50}^{-2}$ ergs/s which selects group and cluster mass objects. Second, the BCG of a fossil system must be 2 $R$-band magnitudes brighter than the next brightest group galaxy within half the projected virial radius. This difference in brightness between the first- and second-ranked galaxies is referred to as the magnitude gap $\Delta m_{12}$. The magnitude gap requirement was chosen to match the predicted effects of dynamical friction: for a typical group, $L*$ satellite galaxies within half the virial radius will merge with the central galaxy within a Hubble time. This motivates the specific cut at

$\Delta m_{12} \geq 2$ mag which is sufficient to select galaxy systems missing their $L*$ galaxies within the region in which the gap criterion is applied.

Space density estimates of fossil systems indicate fossils represent a significant fraction of X-ray luminous groups and clusters. Numerous estimates of the fossil space density have been determined from observations (Vikhlinin et al. 1999; Jones et al. 2003; Santos et al. 2007; La Barbera et al. 2009) and simulations (Dariush et al. 2007; Sales et al. 2007; von

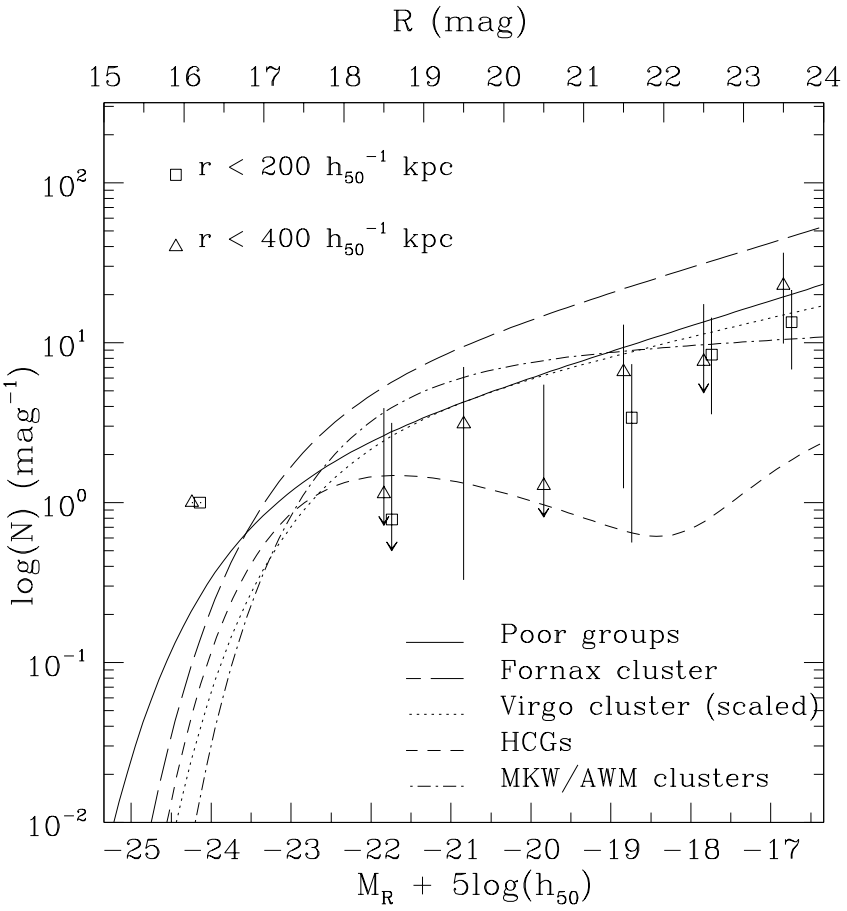


**Figure 1.1** : The luminosity function of fossil group RX J1340.6+4018, plotted with square and triangle points, compared against luminosity functions of other types of galaxy systems. Fossil systems display an unusual luminosity function at the bright end, unique from that of rich clusters, like Fornax and Virgo, as well from that of poor groups and clusters. Figure from Jones et al. (2000).

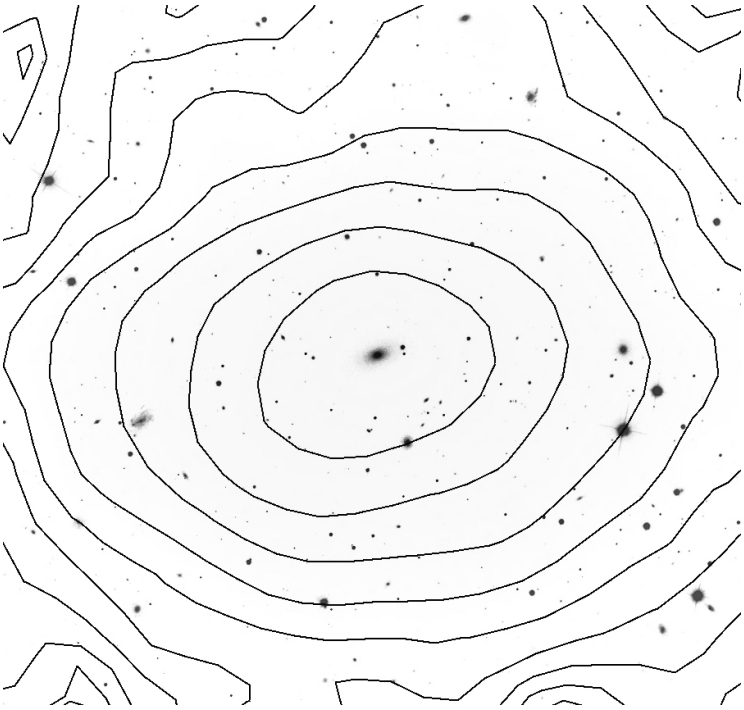

**Figure 1.2** : Fossil cluster [SMS2007]26 ($z = 0.072$) shown with a 12'×12' combined SDSS $r$- and $g$-band optical image with overplotted *Suzaku* 0.5-10 keV contours. Note the relaxed intracluster medium X-ray contours centered around the bright central elliptical; from the sample of Kundert et al. (2015).

Benda-Beckmann et al. 2008; Díaz-Giménez et al. 2008), ranging from $(0.48-19)\times10^{-6}h_{70}^{3}$ Mpc$^{-3}$. This large range in value is due in part to the small sample sizes of the studies as well as the use of varying fossil definitions; in practice most fossil studies use the J03 criteria as a guideline instead of a strict definition. In general though it seems fossils represent $\sim$ 20% percent of observed galaxy systems in the same X-ray luminosity range as the J03 criteria (Jones et al. 2003; Gozaliasl et al. 2014b). Analytics based on the Press-Schechter formalism indicate the highest incidence of fossils in the group mass regime, with $\sim$ 40% of systems identified as fossil at $M \sim 10^{13}M_{\odot}$, and declining incidence towards the cluster regime, with $\sim$ 1% of systems identified as fossil at $M \sim 10^{15}M_{\odot}$ (Milosavljević et al. 2006). Furthermore, the $\Delta m_{12} > 2$ mag gap of fossil systems is unlikely to occur by cosmic variance in rich systems, as shown in Fig. 1.3 (Dariush et al. 2007).

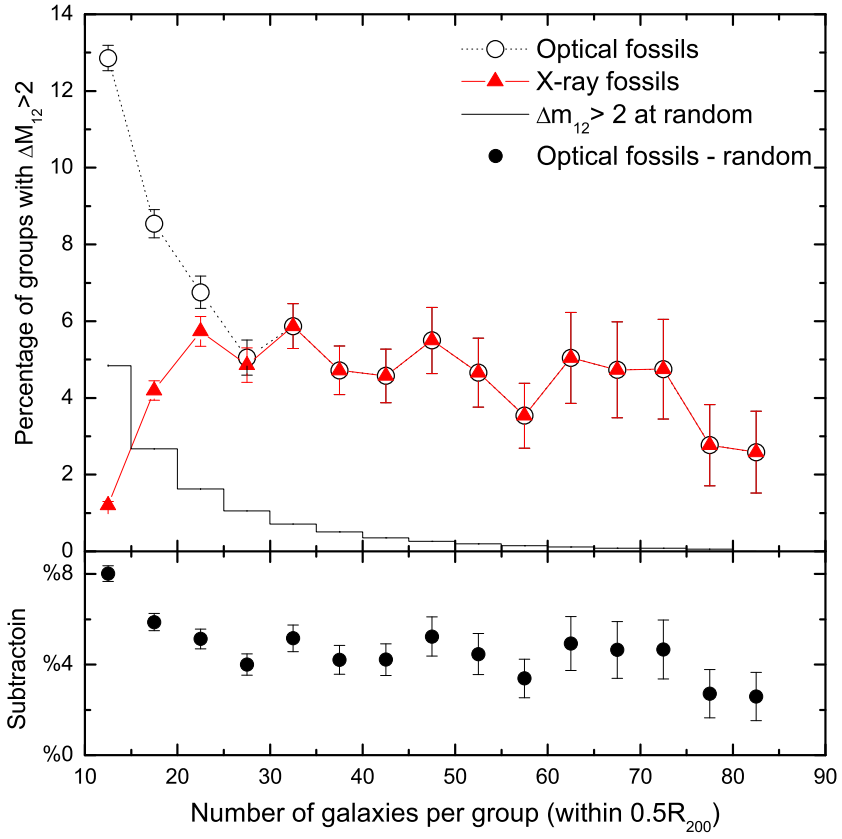


**Figure 1.3** : From Dariush et al. (2007), the probability of obtaining the J03 fossil criteria by chance. Distributions of the optical and X-ray fossils are from the Millennium Simulation (Springel et al. 2005). The 'at random' results are the output of randomly sampling a Schechter function $10^6$ times, with luminosity function parameters $M*$ and $\alpha$ typical of galaxy systems in the Millennium Simulation. It is unlikely for groups and clusters with more than 30 galaxy members to have the characteristic J03 fossil properties due to cosmic variance.

## 1.1 Fossil galaxy system origin scenarios

With an appreciable fraction of galaxy groups and clusters classifying as fossil systems, understanding the origin of the extreme magnitude gaps of fossils may reveal important insights into how galaxies and galaxy systems evolve.

Initial observations of fossils showed systems with relaxed group scale X-ray isophotes

centered around BCGs that displayed no signatures of merging or recent star formation (Jones et al. 2003). From these observations it was interpreted that this sample of fossil systems had both halos without recent group-group mergers as well as central galaxies without recent galaxy-galaxy mergers. It was proposed then that fossils had assembled their mass at relatively early times in the universe and, remaining undisturbed, had passively evolved until the present. In this origin scenario, fossils represent the end stage of galaxy system evolution and are relics of an early formation time. In simulations, where the mass assembly histories can be directly traced, fossils have indeed been found to have earlier formation times on average (D'Onghia et al. 2005; Dariush et al. 2007; von Benda-Beckmann et al. 2008; Díaz-Giménez et al. 2008; Dariush et al. 2010), although there is a significant contamination of young systems with large magnitude gaps, as well as old systems with small gaps.

Simulations also show that galaxy systems may possess the characteristic large gap of fossil systems for only a few Gyr (von Benda-Beckmann et al. 2008; Kanagusuku et al. 2016). In this case a group or cluster with a large magnitude gap is in a transient relaxed "fossil phase", but does not necessarily have an earlier formation time. This relaxed state may result from lack of recent major mergers with other similar mass galaxy systems which would inhibit replenishment of the massive satellite population as they merge with the central galaxy.

Complicating the understanding of how fossils obtain their magnitude gap is the likelihood of some mass dependence on the origin scenario. Fossil clusters are unlikely to form the characteristically bright fossil BCG through galaxy-galaxy mergers as a result of their high velocity dispersion. A possible explanation then for this phenomenon is that fossil clusters are the result of a fossil group merging with another group or cluster having comparatively less bright galaxies such that the magnitude gap of the fossil group

is preserved during the merger (Harrison et al. 2012). And indeed, one example of a fossil group merging with a poor cluster has been observed (Schirmer et al. 2010). The magnitude gap of fossil clusters may eventually be filled in due to infall from the environment (von Benda-Beckmann et al. 2008; Dariush et al. 2010; Cui et al. 2011; Gozaliasl et al. 2014a), and thus fossil systems may be a transitory phase between highly merged galaxy groups and galaxy clusters.

## 1.2 Overview of fossil galaxy system properties

Whether fossils represent examples of early forming groups or clusters, transient relaxed phases in galaxy system mass assembly, or systems with an unusual mass assembly history is still a matter of debate. Nevertheless, determining how fossils form is important for understanding the evolution of groups and clusters - fossils do not appear to be a distinct class of galaxy system as their properties lie on the extremes of the distributions followed by normal groups and clusters with smaller magnitude gaps. Particularly important for discerning which origin scenario is most likely for fossils is understanding in which ways fossil systems have atypical or consistent properties with other galaxy systems. Here I present a brief overview of fossil properties with regards to their central galaxy properties (Sec. 1.2.1) and group scale properties (Sec. 1.2.2).

### 1.2.1 BCG properties

Observationally, increasing values of the magnitude gap are correlated with increases in the stellar mass of the BCG, the luminosity of the BCG, and the BCG's fractional contribution to the total group optical luminosity (e.g., Fig. 1.4), which strongly indicates galaxy mergers with the BCG play a role in the formation of the fossil system magnitude gap (Harrison et al. 2012; Zarattini et al. 2014).

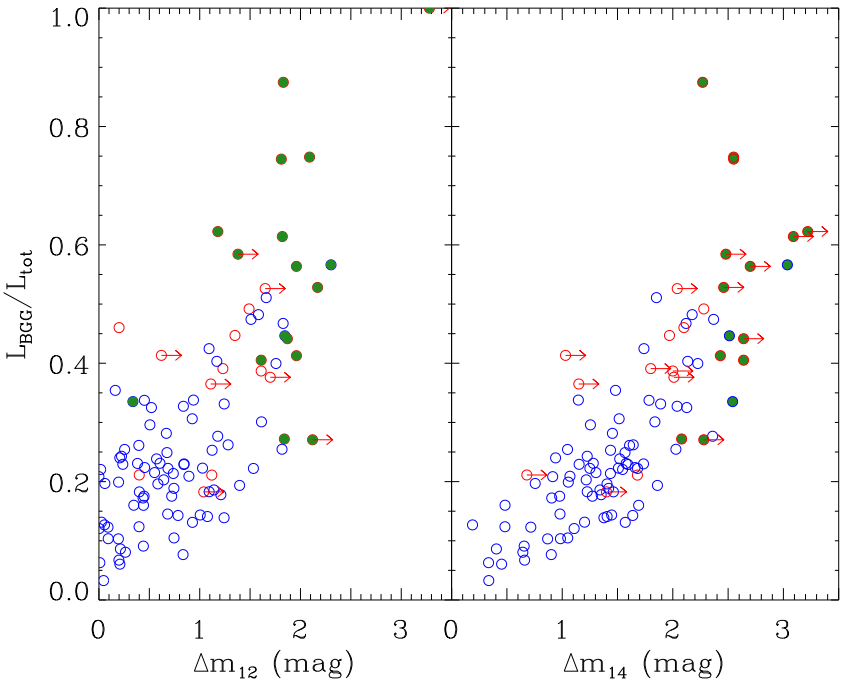


**Figure 1.4** : From Zarattini et al. (2014), the relation between the magnitude gap and the fraction of total group optical luminosity contributed by the BCG. BCGs of the large magnitude gap fossil groups (green filled-in circles) contribute more to their group's total optical light than the BCGs of non-fossil systems (red and blue unfilled circles).

However, despite the exceptional mass and luminosity of fossil BCGs, in many aspects they are similar to bright ellipticals in normal groups and clusters. The properties of fossil BCG stellar populations appear to be nearly entirely consistent with those of other bright ellipticals; for example, when compared to ellipticals of similar mass, fossil centrals show similar structural parameters, ages, metallicities, and abundances (La Barbera et al. 2009; Cui et al. 2011; Harrison et al. 2012; La Barbera et al. 2012; Eigenthaler & Zeilinger 2013; Proctor et al. 2014; Trevisan et al. 2017). Furthermore, fossil BCGs follow the Fundamental Plane, Kormendy relation, and Faber-Jackson relation of normal ellipticals (Méndez-Abreu et al. 2012).

While simulations show a bias for large magnitude gap systems to assemble the majority of their final group halo mass earlier than non-fossils, the BCGs of fossils in

these same simulations assemble their mass more recently than the BCGs of non-fossils. In the Millennium Simulation, 50% of the final group halo mass was assembled by $z = 0.46$ for fossils and at $z = 0.17$ for non-fossils. The BCGs, however, assembled 50% their final stellar mass by $z = 0.56$ for fossils compared to $z = 0.69$ for non-fossils, with the last major merger experienced by the fossil and non-fossil BCGs occuring at $z = 0.28$ and $z = 0.46$ respectively (Díaz-Giménez et al. 2008). The late time fossil BCG stellar mass assembly and last major merger in simulations has support in observations: some fossil BCGs have been found to show signs of recent active evolution in the optical (Ulmer et al. 2005; Alamo-Martínez et al. 2012; Eigenthaler & Zeilinger 2012; Lieder et al. 2013), radio (Hess et al. 2012; Miraghaei et al. 2014), and X-ray (Khosroshahi et al. 2006; Miller et al. 2012). Thus it appears that fossil systems, and in particular fossil BCGs, are not as passively evolving as initially hypothesized.

### 1.2.2 Galaxy group scale properties

If fossils are early-forming and undisturbed, they should be an optimal environment for a cooling flow to develop. Initial studies of individual temperature profiles found fossils with no cool cores (Khosroshahi et al. 2004, 2006), cool cores smaller than expected and likely heated by AGN (Sun et al. 2004), as well as temperature profiles with cool cores similar to other relaxed galaxy systems (Démoclès et al. 2010). In a large study of 17 fossils, Bharadwaj et al. (2016) found 82% of their fossil sample classified as cool core systems, compared to $\sim 72 - 77\%$ of normal groups and clusters. However, this study also finds that only a few fossils in their sample have a short central cooling time ($t_{cool} < 1$ Gyr) with a pronounced decrease in the temperature profile and most fossils have instead a weak cool core ($1 < t_{cool} < 7.7$ Gyr) showing little or no central temperature profile decrease.

Another test of the fossil system formation time is whether these systems have a

greater NFW profile concentration parameter (Navarro et al. 1997) compared to similar mass non-fossil systems. In the Millennium Simulation where fossils are on average earlier forming, fossil halos are also more concentrated than control samples (Farhang et al. 2017). This parameter has been measured for a few fossils via a hydrostatic mass analysis of X-ray observations and both normal concentration values (Sun et al. 2009; Démoclès et al. 2010; Pratt et al. 2016) and above average values (Buote et al. 2016; Buote 2017) have been found. Recently, a study of mass profiles using weak lensing found large magnitude gap systems identified at high redshifts (i.e., $0.2 < z < 0.6$) are more concentrated than smaller gap systems of the same mass and redshift (Vitorelli et al. 2018).

The global mass-to-light ratio of fossil systems is a contentious issue and perhaps also suggests multiple fossil formation histories could exist. The optical luminosity of a system will be conserved during galaxy-galaxy merging (Vikhlinin et al. 1999; Girardi et al. 2014), and many studies observe fossil systems with total group mass to total group optical luminosity ratio, $M_{\rm tot}/L_{\rm opt,tot}$, consistent with those of similar mass galaxy systems (Mulchaey & Zabludoff 1999; Khosroshahi et al. 2006; Mendes de Oliveira et al. 2009; Démoclès et al. 2010; Eigenthaler & Zeilinger 2012). However, high $M_{\rm tot}/L_{\rm opt}$ ratios have also been observed (Vikhlinin et al. 1999; Jones et al. 2003; Yoshioka et al. 2004; Khosroshahi et al. 2004, 2007; Proctor et al. 2011; Su et al. 2013). Early-forming systems may have higher $M_{\rm tot}/L_{\rm opt}$ for their mass (Khosroshahi et al. 2007; Proctor et al. 2011), and indeed in the Millennium simulation, groups that assemble the majority of their final mass at $z \sim 1$ were found to have on average a higher $M_{\rm tot}/L_{\rm opt}$ than those that had assembled only 30% of their final mass at the same epoch (Raouf et al. 2014). However, analysis of fossil systems in the Millennium Simulation by Cui et al. (2011), revealed no difference in the $M_{\rm tot}/L_{\rm opt}$ of fossils and non-fossils.

It is possible the environment in which fossil systems are located may play an

important role in their formation. Initially, it was proposed that fossils may exist in isolated regions of the large scale structure - in an isolated environment, the magnitude gap characterizing fossils can form as the $L*$ satellite galaxies merge due to dynamical friction, without being filled in by infalling galaxies from the environment or from mergers with other groups and clusters (Jones et al. 2000, 2003). Isolated fossil systems have been discovered (Adami et al. 2007; Pierini et al. 2011), although a fossil system existing in an overdense region has also been observed (Aguerri et al. 2018).

Simulations by von Benda-Beckmann et al. (2008) revealed no propensity for fossils to occupy underdense regions and Cui et al. (2011) found environment had no effect on the number of simulated fossils meeting the optical criterion of J03 in the GIMIC project. Further understanding of the relation of fossils and the surrounding large-scale structure was revealed by Díaz-Giménez et al. (2011) with a dedicated analysis of the global and local density profiles of fossil systems in the Millennium Simulation. This study confirmed the early formation time of fossils, finding 90% of their fossil population reach half of their final present day mass at $z = 0.69$ compared to $z = 0.36$ for non-fossils. And prior to $z = 0.69$, fossil systems exist in overdense regions compared to the environments of non-fossils, while at $z = 0$ fossils inhabit comparatively underdense regions. Earlier forming systems in general are expected to form in higher density regions (Sheth & Tormen 2004), yet when Díaz-Giménez et al. (2011) compared fossils and non-fossils identified at $z = 0$ with the same formation epoch and mass, the fossil sample was still found in denser environments than non-fossils at high redshifts implying the environment in which fossils formed may indeed influence the formation of their magnitude gap.

## 1.3 Thesis outline

The characteristic extreme magnitude gap of fossil systems indicates these systems represent an interesting stage in the evolution of groups and clusters and hierarchical structure growth. In this thesis, I aim to constrain some of the properties of fossil systems in order to understand their nature and origin.

In Chapter 2, global X-ray luminosities and temperatures of a sample of fossil systems are determined using *Suzaku* observations for the purpose of constructing the scaling relations of fossil systems in the group and cluster mass regimes. In Chapter 3, using the Illustris cosmological simulation, fossil halo and BCG properties are studied in unison with particular emphasis on their mass assembly histories. In Chapter 4, radial profiles of intracluster medium temperature and density are used to measure the mass profile for a fossil group with archival *Chandra* observations. In Chapter 5, conclusions of this thesis work are summarized.

## References


Adami, C., Russeil, D., & Durret, F. 2007, A&A, 467, 459

Aguerri, J. A. L., Longobardi, A., Zarattini, S., et al. 2018, A&A, 609, A48

Alamo-Martínez, K. A., West, M. J., Blakeslee, J. P., et al. 2012, A&A, 546, A15

Barnes, J. E. 1989, Nature, 338, 123

Bharadwaj, V., Reiprich, T. H., Sanders, J. S., & Schellenberger, G. 2016, A&A, 585, A125

Boylan-Kolchin, M., Ma, C.-P., & Quataert, E. 2008, MNRAS, 383, 93

Buote, D. A. 2017, ApJ, 834, 164

Buote, D. A., Su, Y., Gastaldello, F., & Brighenti, F. 2016, ApJ, 826, 146

Cui, W., Springel, V., Yang, X., De Lucia, G., & Borgani, S. 2011, MNRAS, 416, 2997

Dariush, A., Khosroshahi, H. G., Ponman, T. J., et al. 2007, MNRAS, 382, 433

Dariush, A. A., Raychaudhury, S., Ponman, T. J., et al. 2010, MNRAS, 405, 1873

Démoclès, J., Pratt, G. W., Pierini, D., et al. 2010, A&A, 517, A52

Díaz-Giménez, E., Muriel, H., & Mendes de Oliveira, C. 2008, A&A, 490, 965

Díaz-Giménez, E., Zandivarez, A., Proctor, R., Mendes de Oliveira, C., & Abramo, L. R. 2011, A&A, 527, A129

D'Onghia, E., Sommer-Larsen, J., Romeo, A. D., et al. 2005, ApJ, 630, L109

Eigenthaler, P., & Zeilinger, W. W. 2012, A&A, 540, A134

—. 2013, A&A, 553, A99

Farhang, A., Khosroshahi, H. G., Mamon, G. A., Dariush, A. A., & Raouf, M. 2017, ApJ, 840, 58

Girardi, M., Aguerri, J. A. L., De Grandi, S., et al. 2014, A&A, 565, A115

Gozaliasl, G., Khosroshahi, H. G., Dariush, A. A., et al. 2014a, A&A, 571, A49

Gozaliasl, G., Finoguenov, A., Khosroshahi, H. G., et al. 2014b, A&A, 566, A140

Harrison, C. D., Miller, C. J., Richards, J. W., et al. 2012, ApJ, 752, 12

Hess, K. M., Wilcots, E. M., & Hartwick, V. L. 2012, AJ, 144, 48

Jones, L. R., Ponman, T. J., & Forbes, D. A. 2000, MNRAS, 312, 139

Jones, L. R., Ponman, T. J., Horton, A., et al. 2003, MNRAS, 343, 627

Kanagusuku, M. J., Díaz-Giménez, E., & Zandivarez, A. 2016, A&A, 586, A40

Khosroshahi, H. G., Jones, L. R., & Ponman, T. J. 2004, MNRAS, 349, 1240

Khosroshahi, H. G., Maughan, B. J., Ponman, T. J., & Jones, L. R. 2006, MNRAS, 369, 1211

Khosroshahi, H. G., Ponman, T. J., & Jones, L. R. 2007, MNRAS, 377, 595

Kundert, A., Gastaldello, F., D'Onghia, E., et al. 2015, MNRAS, 454, 161

La Barbera, F., de Carvalho, R. R., de la Rosa, I. G., et al. 2009, AJ, 137, 3942

La Barbera, F., Paolillo, M., De Filippis, E., & de Carvalho, R. R. 2012, MNRAS, 422, 3010

Lieder, S., Mieske, S., Sánchez-Janssen, R., et al. 2013, A&A, 559, A76

Mendes de Oliveira, C. L., Cypriano, E. S., Dupke, R. A., & Sodré, Jr., L. 2009, AJ, 138, 502

Méndez-Abreu, J., Aguerri, J. A. L., Barrena, R., et al. 2012, A&A, 537, A25

Miller, E. D., Rykoff, E. S., Dupke, R. A., et al. 2012, ApJ, 747, 94

Milosavljević, M., Miller, C. J., Furlanetto, S. R., & Cooray, A. 2006, ApJ, 637, L9

Miraghaei, H., Khosroshahi, H. G., Klöckner, H.-R., et al. 2014, MNRAS, 444, 651

Mulchaey, J. S., & Zabludoff, A. I. 1999, ApJ, 514, 133

Navarro, J. F., Frenk, C. S., & White, S. D. M. 1997, ApJ, 490, 493

Pierini, D., Giodini, S., Finoguenov, A., et al. 2011, MNRAS, 417, 2927

Ponman, T. J., Allan, D. J., Jones, L. R., et al. 1994, Nature, 369, 462

Ponman, T. J., & Bertram, D. 1993, Nature, 363, 51

Pratt, G. W., Pointecouteau, E., Arnaud, M., & van der Burg, R. F. J. 2016, A&A, 590, L1

Proctor, R. N., de Oliveira, C. M., Dupke, R., et al. 2011, MNRAS, 418, 2054

Proctor, R. N., Mendes de Oliveira, C., & Eigenthaler, P. 2014, MNRAS, 439, 2281

Raouf, M., Khosroshahi, H. G., Ponman, T. J., et al. 2014, MNRAS, 442, 1578

Sales, L. V., Navarro, J. F., Lambas, D. G., White, S. D. M., & Croton, D. J. 2007, MNRAS, 382, 1901

Santos, W. A., Mendes de Oliveira, C., & Sodré, Jr., L. 2007, AJ, 134, 1551

Schirmer, M., Suyu, S., Schrabback, T., et al. 2010, A&A, 514, A60

Sheth, R. K., & Tormen, G. 2004, MNRAS, 350, 1385

Springel, V., White, S. D. M., Jenkins, A., et al. 2005, Nature, 435, 629

Su, Y., White, III, R. E., & Miller, E. D. 2013, ApJ, 775, 89

Sun, M., Forman, W., Vikhlinin, A., et al. 2004, ApJ, 612, 805

Sun, M., Voit, G. M., Donahue, M., et al. 2009, ApJ, 693, 1142

Trevisan, M., Mamon, G. A., & Khosroshahi, H. G. 2017, MNRAS, 464, 4593

Ulmer, M. P., Adami, C., Covone, G., et al. 2005, ApJ, 624, 124

Vikhlinin, A., McNamara, B. R., Hornstrup, A., et al. 1999, ApJ, 520, L1

Vitorelli, A. Z., Cypriano, E. S., Makler, M., et al. 2018, MNRAS, 474, 866

von Benda-Beckmann, A. M., D'Onghia, E., Gottlöber, S., et al. 2008, MNRAS, 386, 2345

Yoshioka, T., Furuzawa, A., Takahashi, S., et al. 2004, Advances in Space Research, 34, 2525

Zarattini, S., Barrena, R., Girardi, M., et al. 2014, A&A, 565, A116

# Chapter 2

# Fossil group origins – VI. Global X-ray scaling relations of fossil galaxy clusters

*A version of this chapter has previously appeared in the* Monthly Notices of the Royal Astronomical Society

Kundert, A., Gastaldello, F., D'Onghia, E., et al. 2015, MNRAS, 454, 161

## Abstract

We present the first pointed X-ray observations of 10 candidate fossil galaxy groups and clusters. With these *Suzaku* observations, we determine global temperatures and bolometric X-ray luminosities of the intracluster medium (ICM) out to $r_{500}$ for six systems in our sample. The remaining four systems show signs of significant contamination from non-ICM sources. For the six objects with successfully determined $r_{500}$ properties, we measure global temperatures in the range $2.8 \leq T_{\rm X} \leq 5.3$ keV, bolometric X-ray luminosities of $0.8 \times 10^{44} \leq L_{\rm X,bol} \leq 7.7 \times 10^{44}$ erg s$^{-1}$, and estimate masses, as derived from $T_{\rm X}$, of $M_{500} > 10^{14}$ M$_{\odot}$. Fossil cluster scaling relations are constructed for a sample that combines our *Suzaku* observed fossils with fossils in the literature. Using measurements of global X-ray luminosity, temperature, optical luminosity, and velocity dispersion, scaling relations for the fossil sample are then compared with a control sample of non-fossil systems. We find the fits of our fossil cluster scaling relations are consistent with the relations for normal groups and clusters, indicating fossil clusters have global ICM X-ray properties similar to those of comparable mass non-fossil systems.

## 2.1 Introduction

Fossil galaxy systems are group and cluster mass objects characterized by extended, relaxed X-ray isophotes and an extreme magnitude gap in the bright end of the optical luminosity function of their member galaxies. Typically, fossils are identified with the criteria of a halo luminosity of $L_{\rm X,bol} \geq 0.5 \times 10^{42}$ erg s$^{-1}$ and a first ranked galaxy more than 2 $R$-band magnitudes brighter than the second brightest galaxy within half the virial radius (Jones et al. 2003). Fossil systems comprise 8-20 per cent of groups and clusters in the same X-ray luminosity regime (Jones et al. 2003), and thus determining the origin of the features characterizing these systems is important for understanding the nature and evolution of a significant fraction of galaxy groups and clusters.

The features of fossil systems seem to fulfill theoretical predictions that the Milky Way luminosity ($L^*$) galaxies in a group will merge into a central bright elliptical in less than a Hubble time, but the time-scale for the cooling and collapse of the hot gas halo is longer (Barnes 1989; Ponman & Bertram 1993). Indeed the first fossil group discovered, RX J1340.6+4018 (Ponman et al. 1994), appeared as a solitary bright elliptical located in the centre of a group-sized X-ray luminous halo. It was thought the central galaxy of this group was the final merger remnant of the former group galaxies, and hence this object was named a 'fossil group'. Since then, deeper observations have found this system to consist of galaxies other than the bright central galaxy (BCG; Jones et al. 2000) and as a result the magnitude gap criterion of fossils has been established. The motivation for this criterion is that over time, an increasingly growing difference between the two brightest galaxies will form as a result of the merging of the most massive galaxies into a single bright central elliptical if no infall occurs. This formation scenario is well suited for group mass fossils

where the velocity dispersion is low and the dynamical friction time-scale is short.

A number of objects meeting the fossil criteria have also been observed in the cluster mass regime as well (Cypriano et al. 2006; Khosroshahi et al. 2006; Voevodkin et al. 2010; Aguerri et al. 2011; Harrison et al. 2012). It is possible fossil clusters may form as the result of two systems merging, where one group has had its bright galaxies merge due to dynamical friction, and the other has comparatively fainter galaxies (Harrison et al. 2012). Should merging occur between systems with similarly bright galaxies, any previously existing magnitude gaps may become filled in. Therefore, meeting the fossil criteria may only be a transitory phase in the evolution of a group or cluster (von Benda-Beckmann et al. 2008; Dariush et al. 2010).

Numerical and hydrodynamic simulations indicate the large magnitude gaps characterizing fossil groups and clusters are associated with an early formation time: fossil systems have been found to assemble more of their total dynamical mass than non-fossil systems at every redshift (Dariush et al. 2007), where half the dynamical mass is assembled by $z > 1$ (D'Onghia et al. 2005). Evidence that fossils have formed and evolved in a different manner than normal groups and clusters should then manifest in differences in their respective properties.

The bright central galaxy which dominates the optical output of fossil systems has a number of unique characteristics, although whether this demonstrates a clearly distinct formation scenario from non-fossil BCGs is still uncertain. The BCGs of fossils are more massive in both the stellar component and in total than the central ellipticals in non-fossil systems of the same halo mass (Harrison et al. 2012). Méndez-Abreu et al. (2012) find fossil BCGs are consistent with the Fundamental Plane of non-fossil BCGs, but show lower velocity dispersions and higher effective radii when compared to non-fossil intermediate-mass elliptical BCGs of the same $K_{\rm s}$-band luminosity. These results suggest the fossil

BCG has experienced a merger history of early gas-rich dissipational mergers, followed by gas-poor dissipationless mergers later.

On the global scale, the scaling relations of fossil systems remain a point of contention due to limited data and inhomogeneities between studies. Khosroshahi et al. (2007, hereafter KPJ07) performed a comprehensive analysis of a sample of group mass fossil systems and found their sample fell on the same $L_{\rm X}$–$T_{\rm X}$ relation as non-fossils. However, the fossil groups were found to have offset $L_{\rm X}$ and $T_{\rm X}$ for a given optical luminosity $L_{\rm opt}$ or velocity dispersion $\sigma_v$ when compared to normal groups, which was interpreted as an excess in the X-ray properties of fossil systems for their mass. In a comparable study, Proctor et al. (2011) found similar deviations between fossils and non-fossils. This offset, however, was interpreted as fossils being underluminous in the optical which is supported by their large mass-to-light ratios. These features would not result from galaxy-galaxy merging in systems with normal luminosity functions, and thus this analysis calls into question the formation scenario commonly attributed to generating the characteristic large magnitude gap of fossil systems. Later studies, such as Harrison et al. (2012) and Girardi et al. (2014, hereafter G14), find no difference in the $L_{\rm X}$–$L_{\rm opt}$ relation of fossil systems and non-fossils. Even so, most recently Khosroshahi et al. (2014) present a sample of groups, one of which qualifies as a fossil, that lies above the $L_{\rm X}$–$L_{\rm opt}$ relation of non-fossil systems, reopening the debate on fossil system scaling relations.

In this paper we have undertaken an X-ray study of 10 candidate fossil systems, never previously studied with detailed pointed observations in the X-ray regime. Using *Suzaku* data, we present the first measurements of intracluster medium (ICM) temperatures, bolometric X-ray luminosities, and estimates of the $M_{500}$ masses of our systems. This work comprises the sixth instalment of the FOssil Group Origins (FOGO) series. The FOGO project is a multiwavelength study of the Santos et al. (2007) candidate fossil system

catalogue. In FOGO I (Aguerri et al. 2011), the FOGO project is described in detail and the specific goals of the collaboration are outlined. FOGO II (Méndez-Abreu et al. 2012) presents a study of the BCG scaling relations of fossil systems and the implications for the BCG merger history. Global optical luminosities of our FOGO sample are measured in FOGO III (G14) and used to construct the global $L_{\rm X}$–$L_{\rm opt}$ relation which reveals no difference between the fossil and non-fossil fits. Deep $r$-band observations and an extensive spectroscopic database were used to redetermine the magnitude gaps of the FOGO sample and reclassify our fossil candidate catalogue in FOGO IV (Zarattini et al. 2014, hereafter Z14). In FOGO V (Zarattini et al. 2015), the correlation of the size of the magnitude gap and the shape of the luminosity function is investigated. In this work (FOGO VI) we advance the characterization of the X-ray properties of fossil systems and constrain the global scaling relations of these objects.

The details and observations of our *Suzaku* sample are described in Sections 2.2 and 2.3. A discussion on how non-ICM sources may contribute to the observed emission of our systems follows in Section 2.4. Tests to determine the contribution of these non-ICM sources are presented in Sections 2.5 and 2.6. Measurements of the global ICM properties of the thermally dominated subset of our sample are recorded in Section 2.7. Global scaling relations and their implications are presented in Section 2.8. For our analysis, we assume a $\Lambda$CDM cosmology with a Hubble parameter $H_0$=70 km s$^{-1}$ Mpc$^{-1}$, a dark energy density parameter of $\Omega_\Lambda$=0.7, and a matter density parameter $\Omega_{\rm M}$=0.3.

## 2.2 The Sample

Our sample of 10 observed galaxy groups and clusters was selected from the Santos et al. (2007, hereafter S07) catalogue of candidate fossil systems. The S07 catalogue was assembled by first identifying luminous $r$ <19 mag red galaxies in the luminous red galaxy

(LRG) catalogue (Eisenstein et al. 2001), and selecting only those galaxies associated with extended X-ray emission in the *ROSAT* All-Sky Survey (RASS). Sloan Digital Sky Survey (SDSS) Data Release 5 was then used to spatially identify companion galaxies to these bright galaxies. Group or cluster membership was assigned to galaxies identified within a radius of 0.5 $h_{70}^{-1}$ Mpc from one of the bright LRGs and with a redshift consistent with that of the LRG. While spectroscopic redshifts were used when available, galaxy membership was primarily determined using photometric redshifts. Groups and clusters with more than a 2 $r$-band magnitude difference between the brightest and second brightest member galaxies within the fixed 0.5 $h_{70}^{-1}$ Mpc system radius were then selected, and those with an early-type BCG were identified as fossils.

Z14 observed the S07 fossil candidate list with the Nordic Optical Telescope, the Isaac Newton Telescope, and the Telescopio Nazionale Galileo to obtain deeper $r$-band images and spectroscopic redshifts for candidate group members allowing for improved system membership. Additionally, the search radius for galaxy system members was extended to the virial radius of the system as calculated from the RASS X-ray luminosity. The Z14 study confirms 15 targets out of 34 S07 candidates are fossil galaxy systems. According to this characterization, our sample contains five confirmed fossil systems and five non-confirmed or rejected fossil systems (see Table 2.1).

## 2.3 Observations and Data Reduction

The 10 systems in our sample were observed with the *Suzaku* X-ray telescope between 2012 May and October (Table 2.1). Our analysis uses the data from *Suzaku*'s three X-ray Imaging Spectrometers (XIS) sensitive to the 0.5–10 keV band. Our single-pointing observations were taken with a normal clocking mode, and an editing mode of 3×3 or 5×5 which were combined when both were available. The stacked XIS0+XIS1+XIS3 raw count

Table 2.1 : Summary of observations.

| Object | Sequence number | RA | Dec. | Start date | Exposure [ks] | Type[†] |
|---|---|---|---|---|---|---|
| FGS03 | 807052010 | 07:52:44.2 | +45:56:57.4 | 2012 Oct 28 18:39:14 | 14.3 | F |
| FGS04 | 807053010 | 08:07:30.8 | +34:00:41.6 | 2012 May 06 16:24:20 | 10.1 | NC |
| FGS09 | 807050010 | 10:43:02.6 | +00:54:18.3 | 2012 May 30 05:18:38 | 9.9 | NC |
| FGS14 | 807055010 | 11:46:47.6 | +09:52:28.2 | 2012 May 29 17:06:08 | 12.4 | F |
| FGS15 | 807057010 | 11:48:03.8 | +56:54:25.6 | 2012 May 26 17:58:41 | 13.6 | NF |
| FGS24 | 807058010 | 15:33:44.1 | +03:36:57.5 | 2012 Jul 28 08:10:10 | 13.2 | NF |
| FGS25 | 807049010 | 15:39:50.8 | +30:43:04.0 | 2012 Jul 28 18:06:02 | 10.6 | NF |
| FGS26 | 807054010 | 15:48:55.9 | +08:50:44.4 | 2012 Jul 29 02:05:54 | 8.6 | F |
| FGS27 | 807056010 | 16:14:31.1 | +26:43:50.4 | 2012 Aug 05 07:14:36 | 10.6 | F |
| FGS30 | 807051010 | 17:18:11.9 | +56:39:56.1 | 2012 May 02 11:43:31 | 14.0 | F |

[†] The fossil status column contains the Z14 updated fossil characterizations of the S07 catalogue. In the fossil status column, 'F' is a confirmed fossil, 'NF' is a rejected fossil, and 'NC' is not confirmed as either a fossil or non-fossil according to Z14 and remains a fossil candidate.

images of the sample are shown in Fig. 2.1.

The analysis of our study was conducted using the HEASOFT version 6.15 software library with the calibration database CALDB XIS update version 20140520. Spectra were extracted using XSELECT version 2.4c and fit using XSPEC version 12.8.1g. The event files were reprocessed using `aepipeline` with the CALDB XIS update 20140203 using the default settings with an additional criterion of COR>6. In our spectral analysis, emission from the $^{55}$Fe calibration sources, located in the corners of each XIS detector, was removed. Additionally, the XIS0 damaged pixel columns caused by micro-meteorites were masked.

A Redistribution Matrix File (RMF) was created for all spectral extraction regions with `xisrmfgen`. For each RMF, two Ancillary Response Files (ARFs) were created with `xissimarfgen`, one to be convolved with the background spectral model, and the other to be convolved with the source model following the method of Ishisaki et al. (2007). Background ARFs were created out to a radius of 20 arcmin using a uniform emission source mode. For the source ARFs, an image of the stacked XIS field-of-view (FOV) was used to model the emission.

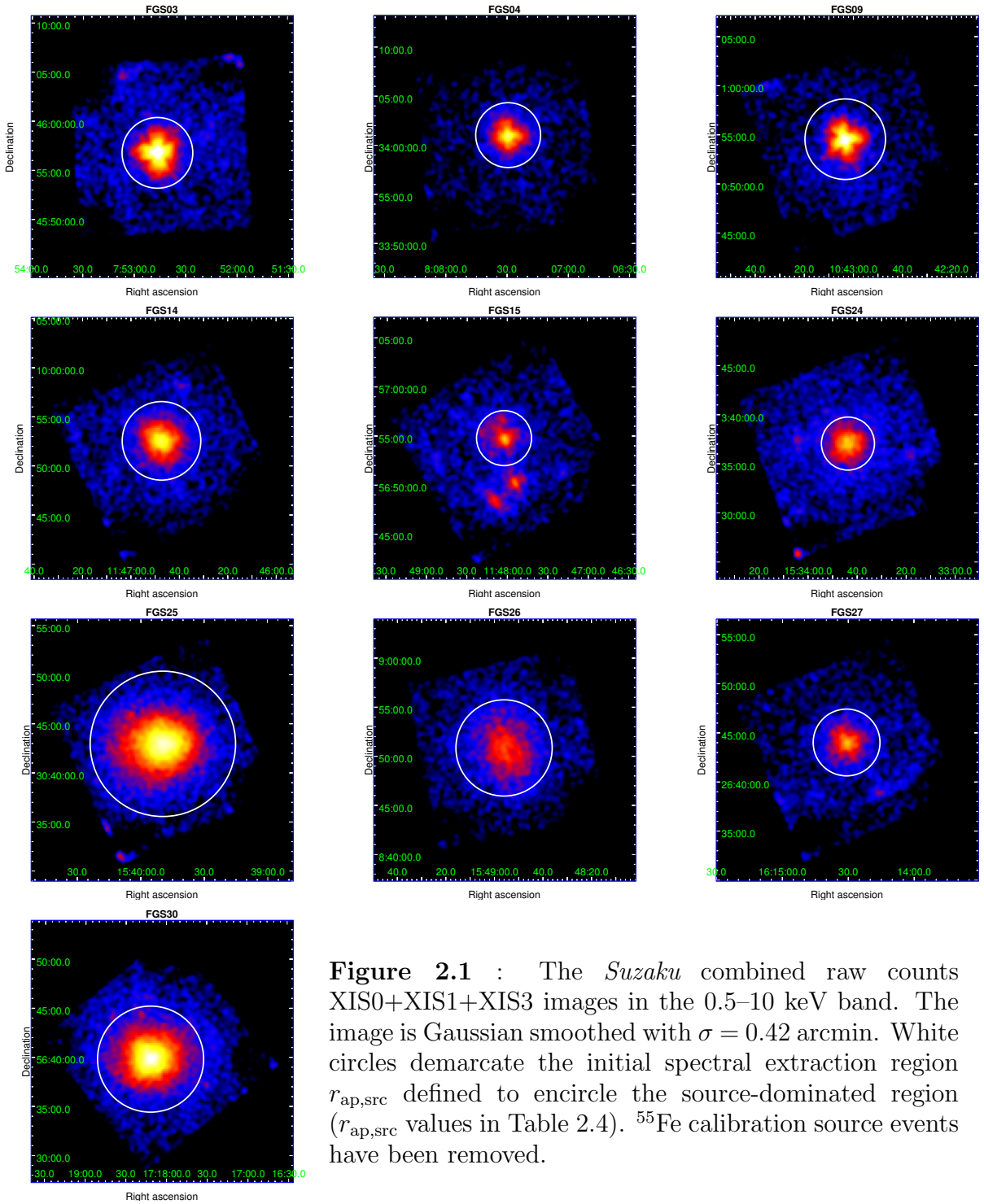


**Figure 2.1** : The *Suzaku* combined raw counts XIS0+XIS1+XIS3 images in the 0.5–10 keV band. The image is Gaussian smoothed with $\sigma = 0.42$ arcmin. White circles demarcate the initial spectral extraction region $r_{\rm ap,src}$ defined to encircle the source-dominated region ($r_{\rm ap,src}$ values in Table 2.4). $^{55}$Fe calibration source events have been removed.

## 2.4 Treatment of non-ICM emission

High fidelity measurements of the ICM temperature and luminosity require careful consideration of non-ICM sources of emission during our analysis.

### 2.4.1 Background and foreground sources

The standard *Suzaku* XIS background consists of a non-X-ray particle background (NXB; Tawa et al. 2008), the cosmic X-ray background (CXB; Fabian & Barcons 1992), and foreground Galactic emission from the Local Hot Bubble (LHB) and the Milky Way Halo (MWH; Kuntz & Snowden 2000).

The contribution of the NXB for each object was assessed using the night earth database within 150 days of the observation using the FTOOL `xisnxbgen` (Tawa et al. 2008). Our XIS1 observations were taken in a charge injection mode of CI = 6 keV which increases the NXB. Accordingly, the `nxbsci6` calibration file was used as input for XIS1 to counteract this.

The contribution of the galactic foreground to a XIS spectrum is well described by two thermal plasma models: $\textsc{apec}_{\rm LHB}+(\textsc{wabs} \times \textsc{apec}_{\rm MWH})$ where $z_{\rm LHB} = z_{\rm MWH} = 0$, $Z_{\rm LHB} = Z_{\rm MWH} = 1\ Z_{\odot}$, and $kT_{\rm LHB} = 0.1$ keV (Kuntz & Snowden 2000). The CXB was modelled by an absorbed power-law: $\textsc{wabs} \times \textsc{powerlaw}_{\rm CXB}$ with $\Gamma = 1.412$ (Kushino et al. 2002). During spectral analyses, the summed background and foreground model: $\textsc{apec}_{\rm LHB}+\textsc{wabs}(\textsc{apec}_{\rm MWH}+\textsc{powerlaw}_{\rm CXB})$ was convolved with the uniform emission ARF.

### 2.4.2 Solar wind charge exchange

The interaction of ions in the solar wind with neutral atoms in the heliosphere and in Earth's atmosphere can produce $E < 1$ keV photons in the X-ray regime (Cravens

2000; Fujimoto et al. 2007). To check for contamination from solar wind charge exchange (SWCX), proton flux light curves with a sampling frequency of 90 s were obtained from the NASA WIND-SWE database over the time span of each observation. The intensity of proton flux has been found to be related to the strength of geocoronal SWCX contaminating photons, where flux levels above $4 \times 10^8$ protons cm$^{-2}$ s$^{-1}$ commonly indicate potentially significant contamination to X-ray spectra from charge exchange (Yoshino et al. 2009). Following Fujimoto et al. (2007), 2700 s were added to the time points in the WIND-SWE light curve to account for the travel time between the WIND satellite, located at the L1 point, and Earth, where the geocoronal SWCX emission is produced.

Much of the FGS24 observation occurs during an elevated period of proton flux; however, the light curve of FGS24 displays no significant duration flares. Furthermore, as a check, we have performed our spectral analysis on the time windows where the proton flux was less than $4 \times 10^8$cm$^{-2}$s$^{-1}$ and found the results were consistent with the spectral analysis of the full baseline. We therefore consider the effects of SWCX to be small and have recorded the results of the analysis of the full observation in the main text and include the FGS24 light curve and shortened exposure time analysis in Appendix 2.10.

### 2.4.3 Point source contamination

Our *Suzaku* observations are the first pointed X-ray observations of the objects in our sample. Consequently we must assess point source contamination primarily relying on the *Suzaku* data alone. Visual inspection of the XIS images (Fig. 2.1) reveal two obvious point sources in the FGS15 FOV which we are able to exclude in our analysis using circular regions of radius 2.5 arcmin. Additionally, FGS03 and FGS09 show diffraction spikes from a strong point-like sources near the peak of the X-ray emission. However, the large 2 arcmin half-power diameter (HPD) of the *Suzaku* X-ray Telescope (XRT; Serlemitsos et al. 2007)

inhibits the exclusion of these sources and the robust identification of other point sources.

Optical and radio studies of the objects in our sample have found a number of active galactic nuclei (AGN) in spatial proximity to our galaxy systems. Especially concerning are the radio-loud AGN, located near the projected location of the BCGs, found in 7 out of the 10 objects in our sample (Hess et al. 2012). To determine if these radio-loud AGN, and other optical and radio AGN in the FOV, are significant contributors to the source emission in the X-ray regime, we perform image (Section 2.5) and spectral (Section 2.6) analyses. In the 0.5–10 keV range of the XIS, the strength of AGN emission increases towards the harder energies of the spectrum. As a result, the harder photons from an AGN may falsely boost the measured temperature of the ICM if only a thermal model is used to fit the spectrum. Assessing AGN contribution is therefore a crucial step in determining the properties of the ICM.

### 2.4.4 Implementation of RASS data

Because most of our objects extend over the entire single *Suzaku* pointing, a local *Suzaku* background region is not consistently available to assess the background contamination in our source regions. To aid in constraining the LHB, MWH, and CXB, we employ RASS background spectra sensitive to the 0.1–2.4 keV X-ray regime. RASS spectra were obtained through the High Energy Astrophysics Science Archive Research Center (HEASARC) X-ray background tool [1] in an annulus of inner radius 0.5 degrees and outer radius 1 degree centred on each of our sources. The size of this annulus is sufficient to minimize contamination from the source itself where the largest $r_{500}$ radius found for an object in our sample only extends to $\sim$20 per cent of the inner radius of the annular RASS

[1] http://heasarc.gsfc.nasa.gov/cgi-bin/Tools/xraybg/xraybg.pl

background region.

## 2.5 Image Analysis

### 2.5.1 Determination of the source aperture for the spectral analysis region

The region of our initial spectral analysis for each object was established to encircle where the emission from the source dominates the emission from the background, enabling the parameters describing the source spectrum to be determined in a high signal-to-noise ratio (S/N) region. We determine this source region using vignetting and exposure corrected images of the source as well as simulated images of the background estimated from RASS spectra.

For each *Suzaku* pointing, an exposure map was created with `xisexpmapgen` and a flat-field using `xissim`. The flat-field was simulated over the XIS 0.5–10 keV energy range at a monochromatic photon energy of 1 keV for a uniform sky out to 20 arcmin.

An image of the NXB particle background for each pointing was produced with `xisnxbgen` over the same energy range. This image was estimated from night Earth observations within 150 days of the *Suzaku* observation date. The NXB image was uniformly corrected by dividing the count rates by the exposure time.

Emission from the CXB, LHB, and MWH was estimated from RASS background spectra. These spectra were fit with the background model: $\mathrm{APEC_{LHB}}$ + $\mathrm{WABS(APEC_{MWH}}$ + $\mathrm{POWERLAW_{CXB}})$. Because the RASS background spectrum consists of only 7 data points, only the normalizations of the three background components were allowed to vary; the other parameters were fixed at the standard literature values as described in Section 2.4.1. The *ROSAT* PSPC response matrix provided by the background tool was implemented for the fit. In calculating the background photon flux in the *Suzaku* XIS 0.5–10 keV energy

range, the XSPEC `dummyrsp` command was used to extrapolate beyond the *ROSAT* PSPC sensitivity range of 0.1–2.4 keV.

An image of the estimated CXB+LHB+MWH emission was produced with `xissim` out to a radius of 20 arcmin from the coordinates of the X-ray centre of the systems. The emission was modeled with the best-fitting spectral model and photon flux of the RASS background data. Because of the low count rate of CXB+LHB+MWH photons over the exposure time for each object, the exposure time was increased by a factor of 10, and corrected later, to improve the statistics of the surface brightness profile of the resulting image following the method of Kawaharada et al. (2010).

An image of the source could then be created from the images constructed during this procedure. Because the NXB background is not affected by vignetting, the exposure corrected image of the NXB was subtracted from the exposure corrected image of the XIS detector. The resulting image was then vignetting corrected with the flat-field and the vignetting and exposure corrected image of the CXB+LHB+MWH was subtracted to obtain the estimated vignetting corrected image of source emission.

Surface brightness profiles were created using ds9 for the vignetting corrected source, NXB, and CXB+LHB+MWH images as shown for example in Fig. 2.2. The coordinates of peak X-ray emission (Table 2.2) were used as the centre of the surface brightness profile. The profile was constructed from 20 uniformly spaced circular annuli out to the radius of the largest circle that could be inscribed within the XIS FOV from the centre coordinates. The source and combined background profiles were then averaged for the three XIS detectors and the radius at which the source and background emission are equal was identified. We find that within this radius the source contributes on average $\sim$80 per cent of the total counts, with no less than a $\sim$70 per cent source contribution for all objects in our sample. It is this radius, the source radius $r_{\rm ap,src}$, which we have used to define our region of initial

Table 2.2 : General information.

| FGS[a] | Coordinates of Peak X-ray [b] | | $z$[c] | $n_{\rm H}$[d] |
|---|---|---|---|---|
| | RA | Dec. | | $[10^{20}{\rm cm}^{-2}]$ |
| 03* | 07:52:46.48 | +45:56:48.40 | 0.052 | 5.06 |
| 04 | 08:07:29.47 | +34:01:02.95 | 0.208 | 4.27 |
| 09 | 10:43:03.33 | +00:54:33.26 | 0.125 | 3.88 |
| 14* | 11:46:47.37 | +09:52:33.38 | 0.221 | 2.89 |
| 15 | 11:48:02.43 | +56:54:49.57 | 0.105 | 0.998 |
| 24 | 15:33:43.74 | +03:37:03.74 | 0.293 | 3.65 |
| 25 | 15:39:49.57 | +30:42:58.40 | 0.097 | 2.29 |
| 26* | 15:48:56.03 | +08:50:51.27 | 0.072 | 3.14 |
| 27* | 16:14:30.77 | +26:44:02.18 | 0.184 | 3.61 |
| 30* | 17:18:11.79 | +56:39:51.33 | 0.114 | 2.21 |

[a] [SMS2007] ID
[b] Coordinates determined from the stacked XIS0+XIS1+XIS3 raw count image in the 0.5–10 keV band
[c] Spectroscopic redshift of the central bright galaxy in the fossil cluster (S07)
[d] Weighted average galactic hydrogen column density in the direction of the target (Kalberla et al. 2005)
* Confirmed fossil system

source spectral analysis.

### 2.5.2 Surface brightness analysis

Radial surface brightness profiles were constructed for each object using stacked 0.5–10 keV XIS0+XIS1+XIS3 observed images. For the purpose of this profile analysis, we apply an additional satellite attitude correction to the event files used to create the images. *Suzaku* XIS images can contain up to a 1 arcmin position error as a result of a recurrent offset between the XRT optical axis and the satellite attitude (Uchiyama et al. 2008). With the application of a corrected attitude file, the XIS images can thus be sharpened. This correction was performed by generating corrected attitude files with `aeattcor`, and then applying these corrected attitude files to our cleaned event files using `xiscoord`. The new corrected event files are used to produce the images used in our brightness profile analysis,

the brightness profiles of which are shown in Fig. 2.3. The number of annuli for each profile was determined such that each annulus had at minimum 225 counts, which, assuming Poissonian noise, requires the number of counts to be 15 times the error.

The brightness profile of a spherically symmetric and isothermal ICM in hydrostatic

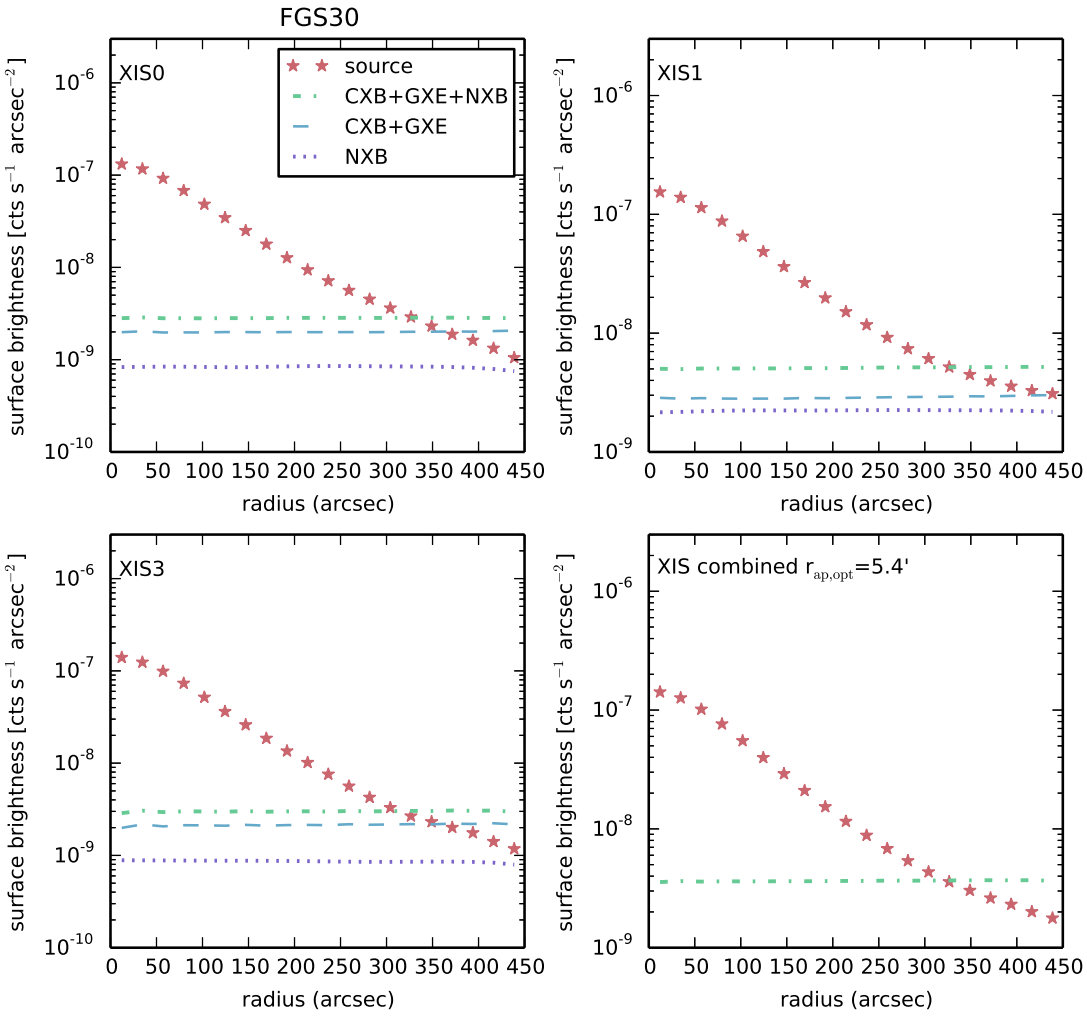


**Figure 2.2** : An example of the estimated source and background surface brightness profiles for FGS30. The bottom right-hand panel shows the average source and background profile for the three XIS detectors.

equilibrium will follow a $\beta$-model (Cavaliere & Fusco-Femiano 1976, 1978). These are appropriate assumptions for virialized and relaxed groups and clusters. Disparity between the data and the single $\beta$-model can therefore result from processes such as merger asymmetries, multiple thermal components, and non-thermal emission, for example, as produced by an AGN. Our initial fit of the profiles consists of a $\beta$-model plus a background constant:

$$S(r) = S_0(1 + (r/r_{\rm c})^2)^{-3\beta+1/2} + k, \tag{2.1}$$

where $S_0$ is the central surface brightness, $r_{\rm c}$ is the core radius, and $k$ is the background surface brightness. In this model, the $\beta$-model component was convolved with a radial model of the *Suzaku* XRT PSF (see Appendix 2.11). Fits were performed with the Sherpa Python module (Doe et al. 2007).

The returned best-fitting parameters are recorded in Table 2.3 and the convolved best-fitting model is shown in Fig. 2.3. We note that FGS03, FGS09, FGS15 have $\chi^2_r > 3$ indicating the $\beta$-model poorly describes the observed emission. For these objects, we test adding to the original model a point-like component consisting of a $\delta$ function convolved with the PSF model. This additional point-source component does not offer an improvement in $\chi^2_r$ compared to the original $\beta$-model fits. Nevertheless, the emission from these three objects seems to indicate that either the ICM is not relaxed, or there is some significant source of non-ICM emission.

Because the annuli used are smaller than the *Suzaku* XRT PSF and, additionally, discrepancy from a $\beta$-model could be attributed to multiple phenomena, we consider the results as merely suggestive and to be used and interpreted in conjunction with our spectral analysis.

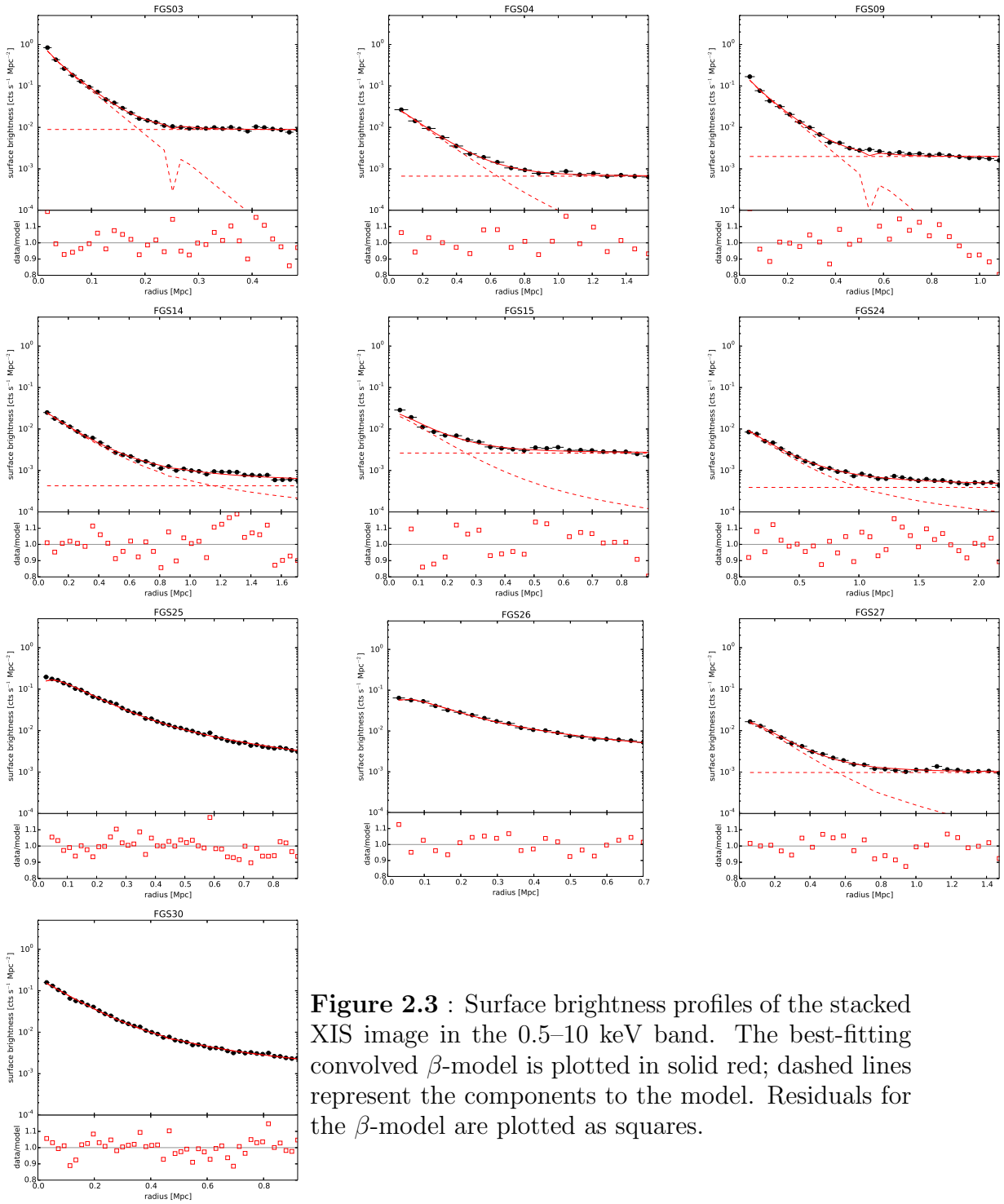


**Figure 2.3** : Surface brightness profiles of the stacked XIS image in the 0.5–10 keV band. The best-fitting convolved $\beta$-model is plotted in solid red; dashed lines represent the components to the model. Residuals for the $\beta$-model are plotted as squares.

Table 2.3 : Best-fitting parameters of the surface brightness profiles.

| FGS | $\beta$-model + background constant | | | | |
|---|---|---|---|---|---|
| | $S_0^\dagger$ [$10^{-2}$] | $r_c$ [kpc] | $\beta$ | $k^\dagger$ [$10^{-4}$] | $\chi^2$/d.o.f. ($\chi^2_r$) |
| 03* | $299.9^{+32.9}_{-37.3}$ | $14^{+2}_{-2}$ | $1.00^{+\infty}_{-0.05}$ | $89.2^{+1.3}_{-1.3}$ | 90/27 (3.3) |
| 04 | $26.7^{+\infty}_{-5.2}$ | $48^{+7}_{-2}$ | $0.64^{+0.02}_{-0.02}$ | $6.7^{+0.2}_{-0.2}$ | 25/15 (1.6) |
| 09 | $50.4^{+4.3}_{-4.5}$ | $38^{+5}_{-5}$ | $1.00^{+\infty}_{-0.05}$ | $19.9^{+0.3}_{-0.3}$ | 126/22 (5.7) |
| 14* | $8.3^{+2.3}_{-1.4}$ | $28^{+11}_{-10}$ | $0.41^{+0.02}_{-0.02}$ | $4.3^{+0.6}_{-0.7}$ | 65/30 (2.2) |
| 15 | $28.7^{+\infty}_{-5.8}$ | $16^{+3}_{-1}$ | $0.49^{+0.02}_{-0.02}$ | $26.3^{+0.7}_{-0.8}$ | 99/19 (5.2) |
| 24 | $2.7^{+0.8}_{-0.5}$ | $38^{+19}_{-17}$ | $0.40^{+0.03}_{-0.03}$ | $3.9^{+0.4}_{-0.5}$ | 49/28 (1.8) |
| 25 | $34.4^{+2.8}_{-0.4}$ | $56^{+3}_{-2}$ | $0.45^{+0.01}_{-0.00}$ | $0.0^{+1.4}_{-\infty}$ | 80/40 (2.0) |
| 26* | $12.7^{+0.9}_{-0.9}$ | $47^{+7}_{-5}$ | $0.37^{+0.01}_{-0.00}$ | $0.0^{+5.8}_{-\infty}$ | 23/17 (1.4) |
| 27* | $3.0^{+0.4}_{-0.3}$ | $88^{+22}_{-20}$ | $0.55^{+0.06}_{-0.05}$ | $9.8^{+0.4}_{-0.4}$ | 37/21 (1.8) |
| 30* | $80.0^{+16.0}_{-15.7}$ | $11^{+3}_{-2}$ | $0.39^{+0.01}_{-0.00}$ | $0.4^{+2.5}_{-2.7}$ | 60/40 (1.5) |

$^\dagger$ Units of counts $s^{-1}$ $Mpc^{-2}$
* Confirmed fossil system

## 2.6 Spectral Analysis

Our spectral analysis consists of measuring spectral properties within a region of high S/N (Section 2.6.1) and using these results to classify these objects as thermally dominated or AGN contaminated (Section 2.6.2). The results of this section will then be used to measure or estimate the global properties of the ICM-dominated systems within $r_{500}$ (Section 2.7).

### 2.6.1 Spectral fitting in the source region

In order to disentangle ICM emission from potential contaminating point source emission, we perform our analysis on the source aperture region where the source emission is more than half of the total emission from the object. By determining this source aperture radius, $r_{\rm ap,src}$ as described in Section 2.5.1, we make no assumptions on the type of source emission. Extracting a spectrum from this region therefore improves the spectral analysis of any type of source over the background whether the source is dominated by thermal

emission from the ICM or non-thermal emission from an AGN.

The results of our surface brightness profile analysis indicate some objects in our sample may have a strong non-thermal point-like component to the total emission. As a result, we compare the fit of three source models to our spectra:

(i) an absorbed thermal plasma model, WABS×APEC, to model the ICM;

(ii) an absorbed power-law, WABS×POWERLAW, to model an AGN;

(iii) an absorbed combined thermal and power-law model, WABS(APEC+POWERLAW), to describe contribution from both the ICM and an AGN;

where the WABS absorption component accounts for galactic absorption in all three models.

The background and foreground sources consist of the NXB, LHB, MWH, and CXB. The NXB spectrum was used as the background file for the extracted $r_{\rm ap}$ region to be subtracted directly during the spectral fit. The CXB, LHB, and MWH were accounted for through modelling as described in Section 2.4.1.

The XIS spectra were grouped with `grppha` such that each bin had a minimum of 25 counts. The binned *Suzaku* XIS0, XIS1, and XIS3 spectra were fit simultaneously with the RASS background spectrum. The *Suzaku* spectra were fit with the source and background model while the RASS spectra were fit only with the background model. The RASS best-fitting parameters were tied to that of the *Suzaku* spectra with a scaling factor to account for the difference in the angular size of the spectral extraction regions. Bad channels were ignored for all spectra. The *Suzaku* XIS0 and XIS3 spectra were fit over 0.7–10 keV (Section 2.6.1.1), the XIS1 spectra over 0.7–7 keV, and the RASS spectra over the range 0.1–2.4 keV.

In all three models, the neutral hydrogen column density was assigned the weighted average galactic value in the direction of the source (Kalberla et al. 2005). The redshifts

of our systems were taken to be the spectroscopic redshifts of the bright central galaxies as determined by S07. During the fit, the column density and redshift were always fixed. The metal abundance $Z$ component of the APEC model was calculated using the abundance tables of Anders & Grevesse (1989). The photon index of the POWERLAW model was constrained to be within $\Gamma = 1.5 - 2.5$ (Ishibashi & Courvoisier 2010). Initially, all other parameters were left free to be fit. However, if during the fit convergence on an APEC or POWERLAW parameter within the physically reasonable limits did not occur or the parameter was returned with infinite error bars, the fit was performed again with that parameter fixed. In all further tables, quantities presented without error bars have been fixed to a reasonable value.

The resulting best-fitting parameters are listed in Table 2.4 and the best-fitting models to the spectra are shown in Fig. 2.4. The background parameters resulting from each of the model fits were consistent with each other within $1\sigma$ errors.

#### 2.6.1.1 A soft energy excess

While the XIS is sensitive to photons with energy as low as 0.5 keV, we have excluded the $E < 0.7$ keV energy channels from our spectral analysis. In the majority of our observations, an apparent excess in counts was found in the 0.5–0.7 keV range when compared to the fit of the APEC or POWERLAW models in the $E > 0.7$ keV range.

Potential origins of this soft excess include a second thermal component in the ICM, an AGN, calibration issues, SWCX, or statistical fluctuations. Adding a second thermal model to the ICM model did not improve the fit. If an AGN were the origin of the excess, removing the softest energies should not greatly deter detecting the presence of its emission in the spectra because an AGN will contribute most strongly to the harder energies of the spectrum. Calibration issues with proportional removal of flickering pixels

from observations of the source and the NXB may also contribute to energy channels below 0.6 keV. Additionally, it is possible there is some contribution from SWCX in the soft energy regime, although the solar wind proton flux light curves of most of our sample are of a low intensity indicating geocoronal SWCX emission is unlikely to be a significant contaminant (see Section 2.4.2).

Because the origin of this excess is uncertain and thus cannot be appropriately modelled in the spectra, and furthermore the excess only affects the first few low energy channels in the spectrum, we exclude this softest energy regime from our fits. This has little effect on the returned best-fitting parameters and in general the reduced $\chi^2$ of the fits improves with the exclusion of the soft excess energy channels.

### 2.6.2 Comparison and interpretation of the model fits

In comparing the fits of the three models, the APEC+POWERLAW model does not appear to significantly improve the characterization of the spectra over the individual APEC and POWERLAW fits. Indeed in the combined fit, the APEC and POWERLAW components are never simultaneously constrained. As a result, while some APEC+POWERLAW fits return $\chi^2_r$ with values slightly less than that for the less complex fits of APEC or POWERLAW only, we decide to choose the simpler model that has all parameters constrained.

By the $\chi^2_r$ values, the POWERLAW model provides a better fit over the thermal APEC model for FGS03, FGS09, FGS15, and FGS24. We consider these four objects to be dominated by a non-ICM source and with our current observations, we cannot disentangle the ICM and non-ICM emission. Further discussion on these objects is provided in Appendix 2.12.

For the remainder of our analysis, we focus on those objects in our sample with spectra that are best fit by the APEC model and are thus galaxy systems dominated by

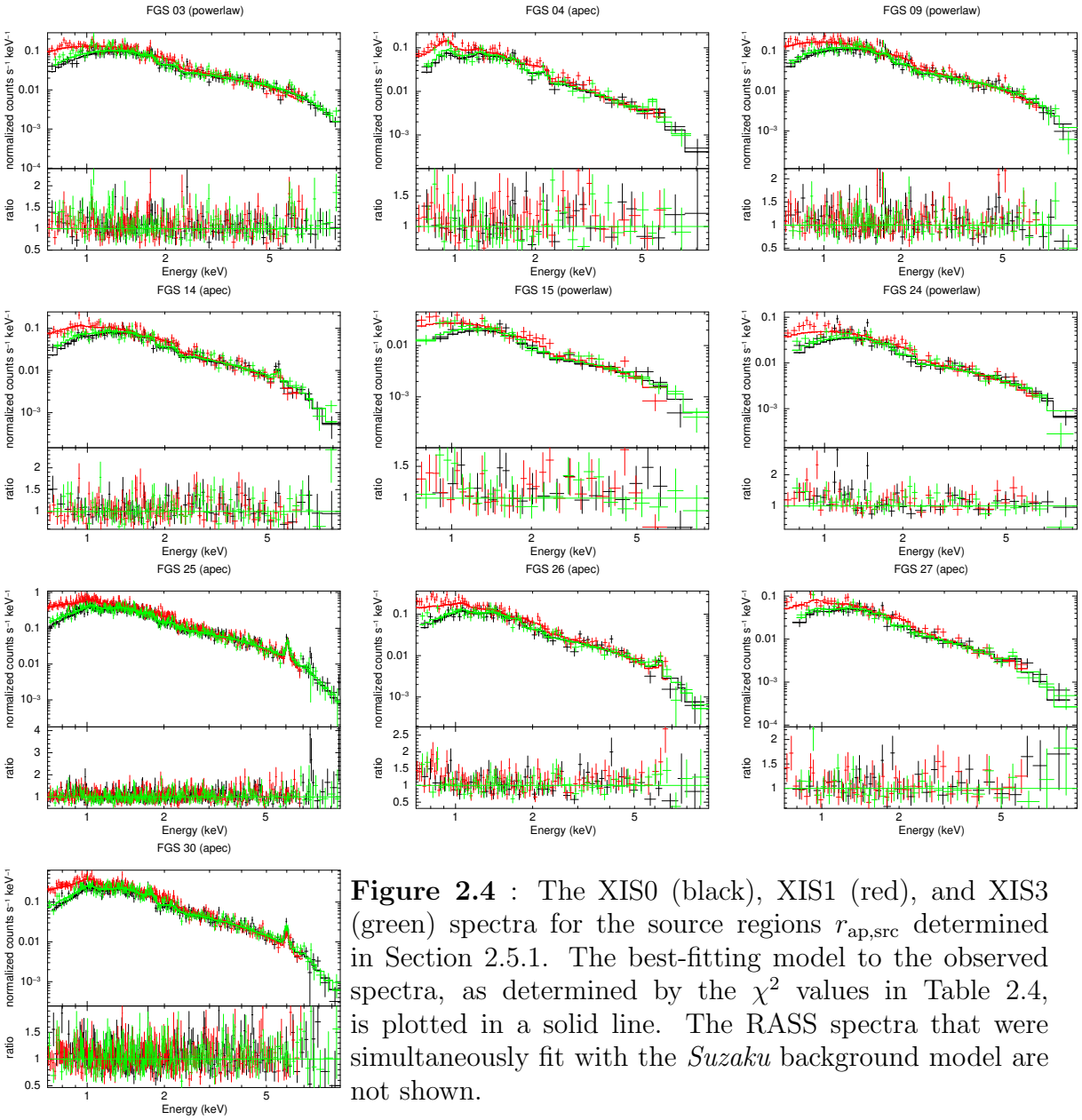


**Figure 2.4** : The XIS0 (black), XIS1 (red), and XIS3 (green) spectra for the source regions $r_{\rm ap,src}$ determined in Section 2.5.1. The best-fitting model to the observed spectra, as determined by the $\chi^2$ values in Table 2.4, is plotted in a solid line. The RASS spectra that were simultaneously fit with the *Suzaku* background model are not shown.

ICM emission.

## 2.7 Global ICM temperatures and luminosities

In order to compare the ICM temperatures and luminosities of our fossil systems with those of other groups and clusters, we calculate these properties within the fiducial radius of $r_{500}$, the radius at which the average enclosed density is 500 times the critical density

Table 2.4 : Best-fitting spectral parameters in the $r_{\rm ap,src}$ region.

| FGS | $r_{\rm ap,src}$ | APEC | | | | POWERLAW | | | APEC+POWERLAW | | | | | |
|---|---|---|---|---|---|---|---|---|---|---|---|---|---|---|
| | | $kT_{\rm apec}$ | $Z_{\rm apec}$ | norm$^a_{\rm apec}$ | $\chi^2$/d.o.f ($\chi^2_r$) | $\Gamma_{\rm PL}$ | norm$^b_{\rm PL}$ | $\chi^2$/d.o.f ($\chi^2_r$) | $kT_{\rm apec}$ | $Z_{\rm apec}$ | norm$^a_{\rm apec}$ | $\Gamma_{\rm PL}$ | norm$^b_{\rm PL}$ | $\chi^2$/d.o.f ($\chi^2_r$) |
| | ['(Mpc)] | [keV] | [$Z_\odot$] | [$10^{-3}$] | | | [$10^{-4}$] | | [keV] | [$Z_\odot$] | [$10^{-3}$] | | [$10^{-4}$] | |
| 03* | 3.6(0.22) | $6.71^{+0.91}_{-0.47}$ | $0.14^{+0.08}_{-0.14}$ | $4.8^{+0.1}_{-0.1}$ | 409/351 (1.17) | $1.72^{+0.03}_{-0.03}$ | $11.9^{+0.4}_{-0.4}$ | 361/352 (1.02) | 2 | 0.3 | $0.3^{+0.5}_{-0.3}$ | $1.68^{+0.07}_{-0.09}$ | $10.9^{+1.3}_{-1.6}$ | 360/351 (1.02) |
| 04 | 3.3(0.67) | $2.84^{+0.18}_{-0.19}$ | $0.40^{+0.12}_{-0.10}$ | $4.3^{+0.3}_{-0.3}$ | 169/148 (1.14) | $2.30^{+0.06}_{-0.06}$ | $10.3^{+0.4}_{-0.4}$ | 212/149 (1.43) | $2.46^{+0.32}_{-0.37}$ | $0.42^{+0.16}_{-0.13}$ | $3.4^{+0.7}_{-0.7}$ | 1.8 | $1.7^{+1.3}_{-1.3}$ | 165/147 (1.12) |
| 09 | 4.1(0.55) | $4.73^{+0.35}_{-0.34}$ | $0.13^{+0.07}_{-0.13}$ | $5.8^{+0.2}_{-0.2}$ | 287/265 (1.08) | $1.94^{+0.04}_{-0.04}$ | $13.6^{+0.4}_{-0.4}$ | 246/266 (0.92) | 2 | 0.3 | $0.0^{+0.6}_{-0.0}$ | $1.94^{+0.04}_{-0.07}$ | $13.6^{+0.4}_{-1.7}$ | 246/265 (0.93) |
| 14* | 4.0(0.86) | $5.23^{+0.44}_{-0.38}$ | $0.21^{+0.08}_{-0.08}$ | $4.9^{+0.2}_{-0.2}$ | 212/237 (0.90) | $1.87^{+0.04}_{-0.04}$ | $9.8^{+0.4}_{-0.4}$ | 262/238 (1.10) | $5.23^{+0.44}_{-0.45}$ | $0.21^{+0.09}_{-0.08}$ | $4.9^{+0.1}_{-1.1}$ | 1.8 | $0.0^{+2.1}_{-0.0}$ | 212/236 (0.90) |
| 15 | 2.8(0.32) | $5.41^{+1.26}_{-0.80}$ | 0.3 | $2.5^{+0.1}_{-0.1}$ | 66/79 (0.83) | $1.79^{+0.09}_{-0.09}$ | $6.0^{+0.4}_{-0.4}$ | 63/79 (0.80) | 2 | 0.3 | $0.0^{+0.3}_{-0.0}$ | 1.8 | $5.9^{+0.4}_{-0.8}$ | 63/79 (0.80) |
| 24 | 2.7(0.71) | $5.67^{+0.88}_{-0.76}$ | $0.21^{+0.15}_{-0.21}$ | $4.7^{+0.3}_{-0.3}$ | 174/126 (1.38) | $1.88^{+0.07}_{-0.07}$ | $8.9^{+0.5}_{-0.5}$ | 169/127 (1.33) | $4.10^{+1.95}_{-2.82}$ | 0.3 | $1.7^{+1.9}_{-1.4}$ | 1.8 | $5.7^{+2.6}_{-3.6}$ | 167/126 (1.33) |
| 25 | 7.4(0.80) | $3.91^{+0.14}_{-0.14}$ | $0.31^{+0.04}_{-0.04}$ | $12.3^{+0.3}_{-0.3}$ | 742/777 (0.96) | $2.04^{+0.02}_{-0.02}$ | $31.5^{+0.6}_{-0.6}$ | 983/778 (1.26) | $3.76^{+0.22}_{-0.26}$ | $0.33^{+0.06}_{-0.05}$ | $11.0^{+1.4}_{-1.5}$ | 1.8 | $3.0^{+3.2}_{-3.0}$ | 740/776 (0.95) |
| 26* | 4.9(0.40) | $3.39^{+0.28}_{-0.24}$ | $0.25^{+0.10}_{-0.10}$ | $5.2^{+0.3}_{-0.3}$ | 325/220 (1.48) | $2.14^{+0.06}_{-0.06}$ | $14.2^{+0.6}_{-0.6}$ | 331/221 (1.50) | $3.10^{+0.45}_{-0.75}$ | $0.24^{+0.13}_{-0.12}$ | $4.3^{+1.0}_{-1.1}$ | 1.8 | $2.3^{+3.0}_{-2.3}$ | 323/219 (1.48) |
| 27* | 3.4(0.63) | $3.42^{+0.34}_{-0.28}$ | $0.20^{+0.13}_{-0.20}$ | $4.0^{+0.3}_{-0.3}$ | 107/121 (0.88) | $2.14^{+0.07}_{-0.07}$ | $8.9^{+0.5}_{-0.5}$ | 115/122 (0.94) | $3.06^{+0.60}_{-0.91}$ | $0.19^{+0.16}_{-0.19}$ | $3.3^{+0.9}_{-1.0}$ | 1.8 | $1.6^{+2.2}_{-1.6}$ | 106/120 (0.88) |
| 30* | 5.4(0.67) | $3.43^{+0.15}_{-0.11}$ | $0.30^{+0.05}_{-0.05}$ | $8.0^{+0.2}_{-0.2}$ | 627/599 (1.05) | $2.08^{+0.03}_{-0.03}$ | $20.0^{+0.4}_{-0.4}$ | 844/600 (1.41) | $3.26^{+0.18}_{-0.20}$ | $0.32^{+0.06}_{-0.06}$ | $7.0^{+0.9}_{-0.8}$ | 1.8 | $2.2^{+1.8}_{-1.8}$ | 623/598 (1.04) |

Note: quantities without errors have been fixed at the listed value

[a] $\text{norm}_{\rm apec} = \frac{10^{-14}}{4\pi[D_A(1+z)]^2}\int n_e n_H dV \text{cm}^{-5}$

[b] $\text{norm}_{\rm PL}$ has units of photons keV$^{-1}$ cm$^{-2}$ s$^{-1}$ arcmin$^{-2}$ at 1 keV

* Confirmed fossil system

of the Universe. We calculate $r_{500}$, and the spectral properties within this radius, using an iterative procedure.

Using the temperature calculated within some aperture, $T_{\rm ap}$, we calculate $r_{500}$ using the $r_{500}$–$T_{\rm X}$ relation of Arnaud et al. (2005):

$$r_{500} = 1.104\ h_{70}^{-1}\ E(z)^{-1} \left(\frac{kT}{5\ \mathrm{keV}}\right)^{0.57} \mathrm{Mpc}, \tag{2.2}$$

where $E(z) = H(z)/H_0 = \sqrt{\Omega_{\rm M}(1+z)^3 + \Omega_{\rm k}(1+z)^2 + \Omega_\Lambda}$ (Hogg 1999) and $h_{70} = H_0/(70\mathrm{km\ s^{-1}\ Mpc^{-1}})$. This value of $r_{500}$ is used as our next radius of extraction to determine a new $T_{\rm ap}$, and we continue this process until convergence is reached between $r_{500}$ and the temperature, and thus $T_{500}$ has been determined. This analysis is performed on the subset of our sample that is thermally dominated (Section 2.6.2). The iterative process is begun with the $T_{\rm ap}$ determined from the APEC only fit as recorded in Table 2.4.

For two of our objects, FGS25 and FGS26, the final estimation of $r_{500}$ extends beyond the largest aperture radius that can be inscribed within the XIS FOV. However, our estimated $r_{500}$ is very similar to the largest aperture size that was used to extract spectral parameters, where the ratio between the maximum $r_{\rm ap}$ and $r_{500}$ is 0.98 and 0.84 for FGS25 and FGS26, respectively. As a result the $T_{\rm ap}$ values for these two objects should reasonably describe the true global temperature within $r_{500}$. When considering the luminosity, $L_{\rm X,500}$ is estimated from $L_{\rm X,ap}$ using a surface brightness profile model that well describes the ICM emission. By integrating this surface brightness model over area, the conversion factor between $L_{\rm X,500}$ and $L_{\rm X,ap}$ is calculated using the relation

$$\frac{L_{\rm X,500}}{L_{\rm X,ap}} = \frac{\int_0^{r_{500}} S(r) r\ dr}{\int_0^{r_{\rm ap}} S(r) r\ dr} \tag{2.3}$$

where $S$ is an azimuthally averaged radial surface brightness profile. For our surface brightness model, we use the $\beta$-model where $S_0$, $r_c$, and $\beta$ have the values recorded in

Table 2.3.

With the global temperature values listed in Table 2.5, we estimate the masses within $r_{500}$ for our systems using the $M_{500}$–$T_{\rm X}$ relation of Arnaud et al. (2005):

$$M_{500} = 3.84 \times 10^{14}\ h_{70}^{-1}\ E(z)^{-1} \left(\frac{kT}{5\mathrm{keV}}\right)^{1.71}\ \mathrm{M}_{\odot}. \tag{2.4}$$

We find our thermally dominated objects have masses consistent with clusters ($M_{500} > 10^{14}$ M$_{\odot}$).

Table 2.5 : Global properties of the ICM-dominated subsample.

| FGS | $r_{\rm ap}/r_{500}$ | $kT_{\rm ap}$ [keV] | $Z_{\rm ap}$ [Z$_{\odot}$] | $L_{\rm X,bol,ap}$ [$10^{44}$ erg s$^{-1}$] | $r_{500}$ | $L_{\rm X,bol,r500}$ [$10^{44}$ erg s$^{-1}$] | $M_{500}$ [$10^{14}$M$_{\odot}$] |
|---|---|---|---|---|---|---|---|
| 04 | 1 | $2.81^{+0.19}_{-0.19}$ | $0.40^{+0.12}_{-0.11}$ | $5.03^{+0.19}_{-0.19}$ | 3.5' (0.71 Mpc) | $5.03^{+0.19}_{-0.19}$ | 1.3 ± 0.1 |
| 14* | 1 | $5.26^{+0.44}_{-0.39}$ | $0.21^{+0.09}_{-0.08}$ | $7.71^{+0.29}_{-0.29}$ | 4.8' (1.03 Mpc) | $7.71^{+0.29}_{-0.29}$ | 3.8 ± 0.5 |
| 25 | 0.98 | $3.92^{+0.15}_{-0.15}$ | $0.28^{+0.04}_{-0.04}$ | $3.80^{+0.09}_{-0.09}$ | 8.5' (0.92 Mpc) | $3.84^{+0.09}_{-0.09}$ | 2.4 ± 0.2 |
| 26* | 0.84 | $3.33^{+0.34}_{-0.30}$ | $0.19^{+0.09}_{-0.08}$ | $0.70^{+0.04}_{-0.04}$ | 10.3' (0.85 Mpc) | $0.82^{+0.05}_{-0.05}$ | 1.9 ± 0.3 |
| 27* | 1 | $3.30^{+0.33}_{-0.31}$ | $0.18^{+0.13}_{-0.18}$ | $3.38^{+0.16}_{-0.16}$ | 4.3' (0.80 Mpc) | $3.38^{+0.16}_{-0.16}$ | 1.7 ± 0.3 |
| 30* | 1 | $3.39^{+0.15}_{-0.11}$ | $0.30^{+0.05}_{-0.05}$ | $3.06^{+0.06}_{-0.06}$ | 6.8' (0.84 Mpc) | $3.06^{+0.06}_{-0.06}$ | 1.9 ± 0.1 |

Note: $L_{\rm X,bol}$ is the unabsorbed X-ray luminosity in the 0.1-100 keV energy range

* Confirmed fossil system

## 2.8 Scaling Relations

We combine our newly measured global $L_{\rm X,bol,500}$ and $T_{\rm X}$ with previously measured fossil systems properties, to constrain the scaling relations of these objects with the goal of assessing if fossil systems display different scaling relations than those for normal groups and clusters. Our analysis of fossil system scaling relations is distinguished from previous studies through several updates including the fitting of the largest assembled fossil system data set, using recent X-ray and optical data for our control sample of normal groups and clusters, and a substantial effort of homogenizing both the fossil and non-fossil data sets. We furthermore record the best-fitting $L_{\rm X}$–$L_r$ relation, and for the first time record the

slopes and $y$-intercepts of the $L_{\rm X}$–$T_{\rm X}$, $L_{\rm X}$–$\sigma_v$, $T_{\rm X}$–$\sigma_v$ scaling relation fits for fossil systems.

### 2.8.1 Sample assembly, correction, and fitting

We have assembled data from a number of studies to investigate how the global X-ray and optical properties of fossil systems compare to non-fossil groups and clusters. To ensure a reliable comparison, we have made an effort to use quantities determined within the same fiducial radius and defined the same way. For our analysis we use bolometric X-ray luminosities $L_{\rm X,bol}$, temperatures $T_{\rm X}$, and optical SDSS $r$-band luminosities $L_r$ all calculated within $r_{500}$, and global velocity dispersions $\sigma_v$. While we have removed known fossils from our sample of non-fossil groups and clusters, we do not have information on the magnitude gap between the first and second brightest galaxies in all of the systems making up our control sample. However, the large magnitude gap characterizing fossil systems should be found in only a fraction of $L_{\rm X,bol} \geq 5 \times 10^{41}$ erg s$^{-1}$ systems (Jones et al. 2003; Milosavljević et al. 2006). Thus, we expect our control sample is contaminated by at most a few unidentified fossil systems.

To assemble our group sample, we use the $\sigma_v$ of the 'G-sample' from Osmond & Ponman (2004). Group $T_{\rm X}$ values are pulled from Rasmussen & Ponman (2007), Sun et al. (2009), Hudson et al. (2010), Eckmiller et al. (2011), and Lovisari et al. (2015). Lovisari et al. (2015) $L_{\rm X,0.1-2.4keV}$ are transformed to $L_{\rm X,bol}$ using the conversion tables of Böhringer et al. (2004).

For the cluster sample, we use the G14 $r$-band optical luminosities calculated within $r_{500}$. The corresponding velocity dispersions are taken from Girardi et al. (1998, 2002), Girardi & Mezzetti (2001), Popesso et al. (2007), and Zhang et al. (2011). Bolometric X-ray luminosities within $r_{500}$ and temperatures were sourced from Pratt et al. (2009) and Maughan et al. (2012), and supplemented with additional $L_{\rm X,bol}$ from Zhang et al. (2011)

and $T_{\rm X}$ from Wu et al. (1999) and Hudson et al. (2010).

Taking our sample of fossil systems observed with *Suzaku*, we match the global X-ray properties of the systems in Table 2.5 with the corresponding $L_r$ from G14 and $\sigma_v$ from Z14. For the remainder of the Z14 confirmed fossil catalogue, we supplement the $L_{\rm X,bol}$ from G14. For improved consistency with the $L_{\rm X}$ of our cluster sample, we approximate X-ray luminosities that more closely resemble those computed using the growth curve analysis (GCA) method (Böhringer et al. 2000) from the G14 luminosities derived from RASS counts (see section 3.3 of G14 for details). These corrected luminosities also show good agreement with the *Suzaku* measured $L_{\rm X}$ for the sample of objects shared between both the G14 study and ours.

We add to the fossil sample with the X-ray luminosities and temperatures from KPJ07 and Miller et al. (2012), matched with the $L_r$ and $\sigma_v$ data from Proctor et al. (2011). The KPJ07 $L_{\rm X,bol,200}$ are rescaled to $r_{500}$ using their best-fitting $\beta$-model parameters and our luminosity conversion Eq. 2.3. To ensure consistency with our *Suzaku* sample, the $r_{500}$ of KPJ07 is recalculated from their temperatures using our Eq. 2.2 and we use this value to estimate $L_{\rm X,bol,500}$. To rescale the $L_{r,200}$ of Proctor et al. (2011) to $r_{500}$, we assume the light follows the mass, which is a good approximation on the global scale of groups and clusters (Bahcall & Kulier 2014). For a NFW density profile with concentration parameter $c = 5$, $M_{500}/M_{200} = 0.70$ (Navarro et al. 1997). The assumption of $c = 5$ was chosen for agreement with the concentrations of normal clusters of similar temperature and mass (Pointecouteau et al. 2005; Pratt & Arnaud 2005; Vikhlinin et al. 2006; Buote et al. 2007; Ettori et al. 2010) because the typical concentration parameter for fossil systems is poorly characterized. Thus, we can rescale using $L_{\rm opt,500}/L_{\rm opt,200} \propto 0.70$. Here, the correction relation is applied only to the non-BCG light.

We also implement the fossil catalogue of Harrison et al. (2012). We take their

$L_{\rm X,bol,200}$ and rescale by assuming a $\beta$-model with $r_{\rm c}$ estimated using the $r_{\rm c}$–$L_{\rm X}$ relation of Böhringer et al. (2000) and $\beta$=0.67, then correcting to $L_{\rm X,bol,500}$ using Eq. 2.3. The optical luminosities provided are calculated for $r = 0.5r_{200} \sim r_{1000}$. By the reasoning described previously, this luminosity is corrected to $L_{r,500}$ using the relation $M_{500}/M_{1000} \propto 1.3$. Because the magnitudes of the BCG were not recorded, we rescale all of the optical light for these objects. The Harrison et al. (2012) $\sigma_v$ are also used, and we assign a 0.1 dex error to these values during our fit of the fossil scaling relations.

With the above data sets, we have enough data to assemble and quantitatively compare the $L_{\rm X}$–$T_{\rm X}$, $L_{\rm X}$–$\sigma_v$, $L_{\rm X}$–$L_r$, $T_{\rm X}$–$\sigma_v$ scaling relations for a sample of fossils and a control sample of normal groups and clusters. We do not investigate the $T_{\rm X}$–$L_r$ relation due to the small subsample of our control population with both $T_{\rm X}$ and $L_r$ measurements.

We fit the equation

$$\log(Y) = a + b\log(X) \tag{2.5}$$

to the data using the BCES orthogonal method (Akritas & Bershady 1996) which accounts for measurement errors in the data as well as intrinsic scatter in the fitted relation. We choose to compare the fit of the fossil sample to a combined sample of groups and clusters (G+C) in the same parameter range as the fossil sample. For the fossil system data set we exclude NGC 6482 from KPJ07 and XMMXCS J030659.8+000824.9 from Harrison et al. (2012) as they are clear outliers.

We cross-checked the results obtained with the BCES method with the IDL Astronomy library tool LINMIX_ERR (Kelly 2007), a Bayesian fitting method for linear regression. The plotted scaling relations and BCES fits are shown in Fig. 2.5 and the best-fitting parameters of the relations are recorded in Table 2.6. Uncertainties on the BCES best-fitting parameters are estimated using 10,000 bootstrap resamplings. For the LINMIX_ERR fits, the quoted values are the mean and the standard deviation of the posterior

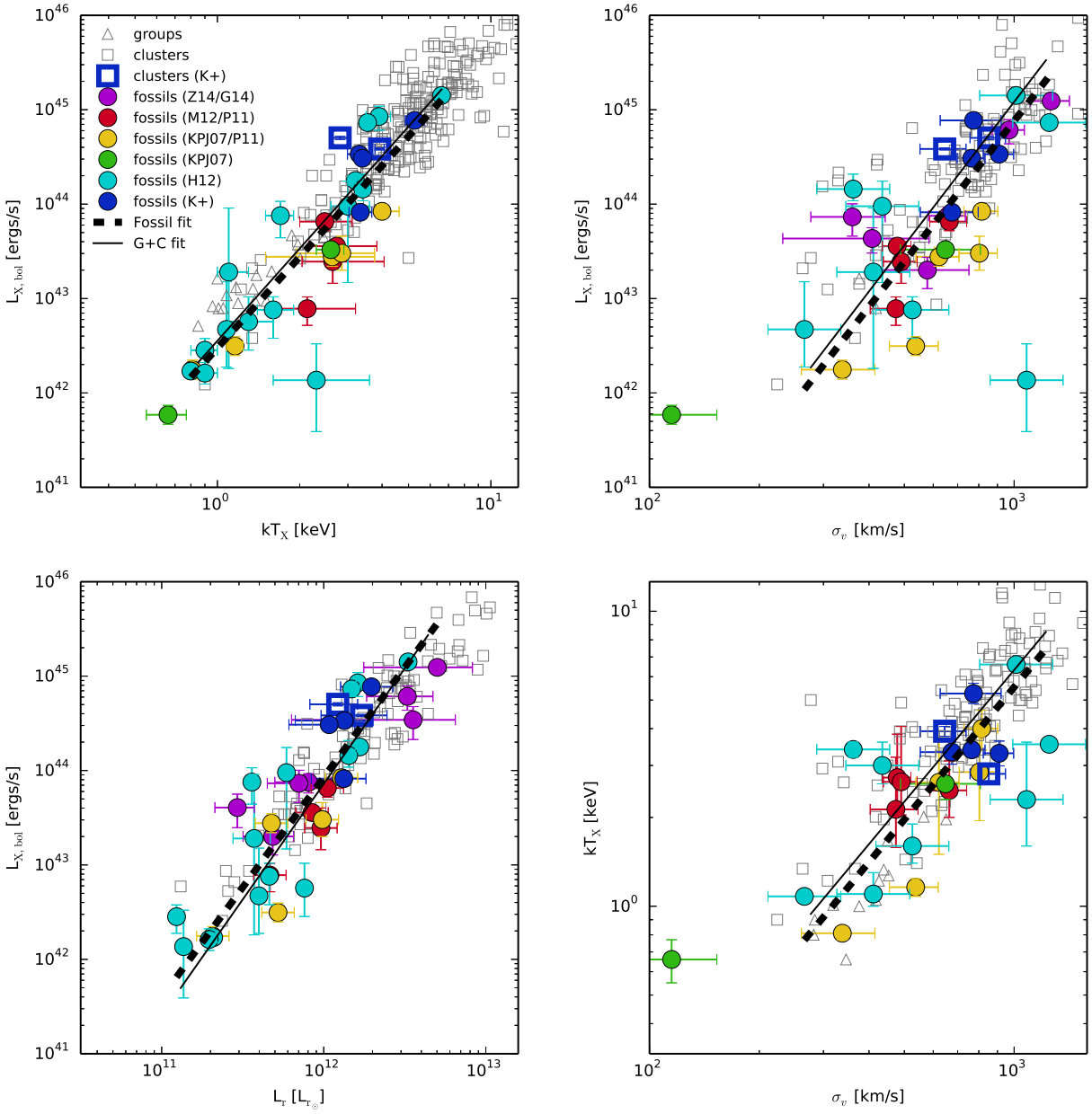


**Figure 2.5** : $L_{\rm X}$, $T_{\rm X}$, $L_r$, $\sigma_v$ scaling relations for fossil and non-fossil samples. We abbreviate this current work as K+, Zarattini et al. (2014) as Z14, Girardi et al. (2014) as G14, Miller et al. (2012) as M12, Proctor et al. (2011) as P11, Khosroshahi et al. (2007) as KPJ07, and Harrison et al. (2012) as H12. The plotted lines are the orthogonal BCES fits to the fossil sample (dashed line) and to the sample of groups and clusters (solid line) in the same parameter range as the fossils.

distributions for the regression parameters. We investigate changing the pivot point of the fits, i.e. rescaling the $X$ and $Y$ values in Eq. 2.5 by a constant, but no difference is found in the returned fits.

We find the BCES fits to the fossil sample are consistent within error to the combined groups and clusters fit for each scaling relation investigated in this work. The LINMIX fossil and non-fossil fits are for the most part consistent within $1\sigma$; the $y$-intercepts of $L_{\rm X,bol}$–$T_{\rm X}$ and the $y$-intercepts and slopes of $L_{\rm X}$–$\sigma_v$ are consistent within $2\sigma$. These slight discrepancies in the LINMIX fits are most likely due to inhomogeneities in the data or the small sample size of both the fossil and control populations.

The global properties involved in these scaling relations: $L_{\rm X}$, $T_{\rm X}$, $L_{\rm opt}$, $\sigma_v$, are determined predominantly by the shape and depth of the potential well, and are thus well-documented proxies for the total mass of the system. Additional important effects that determine the X-ray properties of the ICM include the entropy structure (Donahue et al. 2006) and non-gravitational heating and cooling processes, such as can be caused by AGN or mergers. These factors can produce dispersions in scaling relations between X-ray and optical mass proxies. Finding no difference in the scaling relations between fossil and

Table 2.6 : Best fits to the scaling relations.

| Relation ($Y$-$X$) | Sample | Fitting Procedure | | | |
|---|---|---|---|---|---|
| | | BCES Orthogonal | | LINMIX_ERR | |
| | | $a$ | $b$ | $a$ | $b$ |
| $L_{\rm X,bol}$–$T_{\rm X}$ | Fossils | 42.48 ± 0.17 | 3.21 ± 0.44 | 42.49 ± 0.13 | 3.39 ± 0.29 |
| | G+C | 42.55 ± 0.09 | 3.25 ± 0.14 | 42.74 ± 0.07 | 3.03 ± 0.11 |
| $L_{\rm X,bol}$–$\sigma_v$ | Fossils | 30.05 ± 3.60 | 4.94 ± 1.29 | 28.34 ± 3.22 | 5.51 ± 1.14 |
| | G+C | 29.95 ± 1.40 | 5.05 ± 0.49 | 33.30 ± 0.96 | 3.87 ± 0.33 |
| $L_{\rm X,bol}$–$L_r$ | Fossils | 15.98 ± 3.18 | 2.33 ± 0.27 | 17.18 ± 2.84 | 2.23 ± 0.24 |
| | G+C | 14.47 ± 2.03 | 2.45 ± 0.17 | 17.05 ± 2.73 | 2.24 ± 0.22 |
| $T_{\rm X}$–$\sigma_v$ | Fossils | -3.73 ± 2.44 | 1.49 ± 0.89 | -4.59 ± 1.67 | 1.79 ± 0.59 |
| | G+C | -3.65 ± 0.44 | 1.48 ± 0.15 | -3.92 ± 0.27 | 1.58 ± 0.09 |

non-fossil groups and clusters thus indicates fossil systems are of similar mass as non-fossils, and on the global scale, the combined effect of mass, ICM entropy, and non-gravitational processes that have occurred in fossil systems are similar to the combined effect of those that have occurred in normal groups and clusters.

### 2.8.2 Comparison with previous studies

Our result that fossils share the same $L_{\rm X}$–$T_{\rm X}$ relation as non-fossil groups and clusters is consistent with previous studies (KPJ07; Proctor et al. 2011; Harrison et al. 2012, G14). However, the comparison of optical and X-ray properties of fossil and non-fossil systems is a contentious issue in the literature.

The $L_{\rm X}$–$L_r$, $L_{\rm X}$–$\sigma_v$, $T_{\rm X}$–$\sigma_v$ scaling relation fits of our analysis show the relations of fossil systems are consistent within error to normal groups and clusters. This is in good agreement with the findings of Harrison et al. (2012) and G14. G14 recorded the first quantitative values of their fit to the $L_{\rm X}$–$L_r$ relation and found no difference between fossil systems ($L_{\rm X} \propto L_r^{1.8\pm0.3}$) and a sample of non-fossil clusters ($L_{\rm X} \propto L_r^{1.78\pm0.08}$). While qualitatively we both find no difference in the $L_{\rm X}$–$L_r$ fossil and non-fossil scaling relations, there are some numerical differences in the returned best-fitting parameters of our study and G14.

Our fossil fit of $L_{\rm X} \propto L_r^{2.33\pm0.27}$ is consistent within error to G14, although this is in large part due to the considerable error on both of our slopes. However, our non-fossil fit ($L_{\rm X} \propto L_r^{2.45\pm0.17}$) is not within error of the fit determined by G14. Differences in the slopes of our fits could be due to multiple reasons: (1) we use bolometric $L_{\rm X}$ in our fits, while G14 uses $L_{\rm X,0.1-2.4keV}$; (2) our $L_{\rm X}$ are defined within $r_{500}$ while the fitted G14 $L_{\rm X}$ represent a total luminosity that has not been defined within a precise radius; (3) we use different fitting methods; (4) we fit our control sample of non-fossils over a different parameter space

(i.e., one defined to match our fossil sample).

We check to see if we can return more consistent results with G14 by repeating our analysis of the $L_{\rm X}$–$L_r$ relation using $L_{\rm X,0.1-2.4keV}$ instead of $L_{\rm X,bol}$ and expanding the fit of our control 'G+C' sample to the full parameter space. We find the returned fit to the fossil sample ($L_{\rm X} \propto L_r^{2.11\pm0.26}$) and to the non-fossil sample ($L_{\rm X} \propto L_r^{1.86\pm0.10}$) are both within error of the G14 fits. And again we emphasize that even without the changes made here, although numerically our fits differ from those of G14, the interpretation is the same: fossil systems follow the same $L_{\rm X}$–$L_r$ scaling as non-fossil systems, supporting our conclusion that on the global scale, fossil systems have optical and X-ray properties congruent with those of normal groups and clusters.

Accumulation of multiple differences in data and methodology explain the differences in conclusions between our study and those of earlier studies (KPJ07; Proctor et al. 2011) that find discrepancies in the optical and X-ray scaling relations for fossil and non-fossils. We have compared fossil and non-fossil optical luminosities measured from the same photometric catalogue and band, avoiding the need to make approximative luminosity estimates for comparisons between samples. We have also used optical luminosities defined within the same fiducial radius, thus ensuring a more equal comparison between data pulled from multiple catalogues. Additionally, our large sample size of fossils reduces the effect of noise to ensure a more reliable comparison between the fossil and non-fossil samples.

We note, however, that our best-fitting parameters for both the fossil and non-fossil samples have large errors. Thus, a study of fossil scaling relations could be greatly improved in the future by larger and more homogeneous data sets. Furthermore, our results probe the relations of clusters and high-mass groups, and consequently it is possible differences in the scaling relations exist in the low-mass end (Desjardins et al. 2014; Khosroshahi et al.

2014).

## 2.9 Summary and conclusions

We have presented a detailed study of the X-ray properties of 10 candidate fossil galaxy systems using the first pointed X-ray observations of these objects. In particular, *Suzaku* XIS data have been used to measure their global X-ray temperatures and luminosities and to estimate the masses of these galaxy clusters. We determine 6 of our 10 objects are dominated in the X-ray by thermal bremsstrahlung emission and thus we are able to measure the global temperatures and luminosities of their ICM. This sample of six objects has temperatures of $2.8 \leq T_{\rm X} \leq 5.3$ keV, luminosities of $0.8 \times 10^{44} \leq L_{\rm X,bol} \leq 7.7 \times 10^{44}$ erg s$^{-1}$, and occupies the cluster regime in plotted scaling relations.

Using our newly determined fossil cluster ICM X-ray properties, we combine our fossil sample with fossils in the literature to construct the largest fossil sample yet assembled. This sample is compared with a literature sample of normal groups and clusters, where significant effort has been made to homogenize the global $L_{\rm X}$, $T_{\rm X}$, $L_r$, and $\sigma_v$ data for the fossil and non-fossil samples.

Plotting the $L_{\rm X}$–$T_{\rm X}$, $L_{\rm X}$–$\sigma_v$, $L_{\rm X}$–$L_r$, and $T_{\rm X}$–$\sigma_v$ relations shows no difference between the properties of fossils and normal groups and clusters. Furthermore, we provide the first fits to three of these relations which reveals the relations of fossils systems agree within error to the relations of normal groups and clusters. Our work indicates that on the global scale, fossil systems are no different than non-fossil systems. However, the distinguishing large magnitude gap in the bright end of the fossil system luminosity function is still unexplained and thus further studies are necessary to characterize the properties of these objects and understand their nature.

## 2.10 Appendix: Testing FGS24 for SWCX contamination

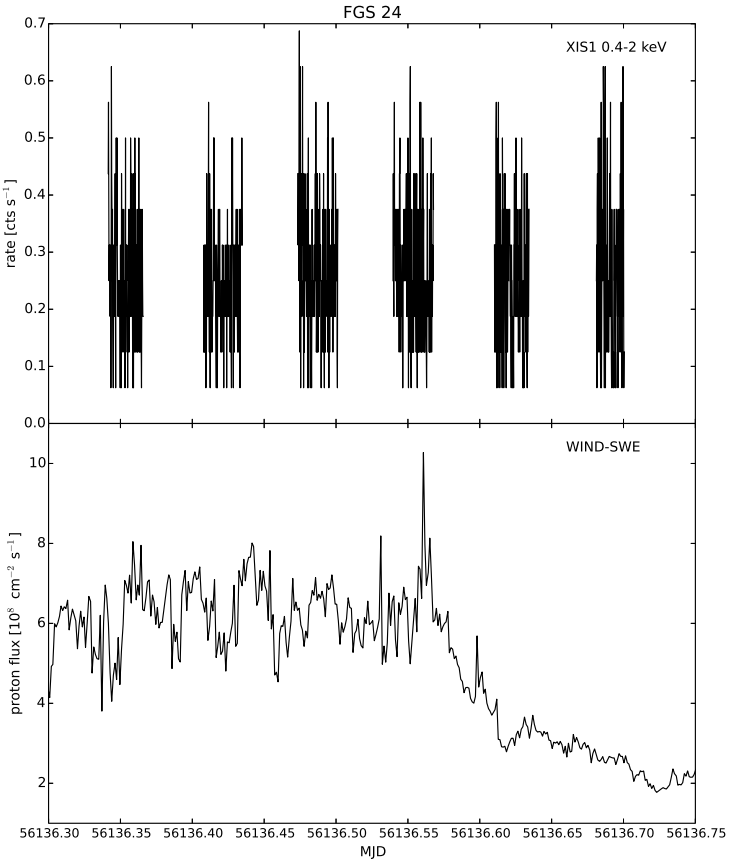


**Figure 2.6** : Top: the observed XIS1 light curve for FGS24. Bottom: the WIND-SWE proton flux light curve plotted for the same time span. Proton flux has been found to be correlated to SWCX. The elevated proton flux levels during the FGS24 observation may potentially cause significant SWCX contaminating emission.

The NASA WIND-SWE proton flux light curve displays elevated flux levels greater than $4\times10^8$ cm$^{-2}$ s$^{-1}$ during a significant portion of the FGS24 observation (Fig. 2.6) which indicates SWCX photons may contaminate the lower $E < 1$ keV region of the spectrum (see Section 2.4.2). To test for evidence of this contamination, we repeat the spectral analysis of Section 2.6.1 for the time intervals where the flux was less than $4 \times 10^8$ cm$^{-2}$ s$^{-1}$. These results are recorded in Table 2.7 and we find these results are consistent within error with those of using the full timespan of the observation (Table 2.4).

Table 2.7 : Best fit spectral parameters during a low proton flux time interval for FGS24.

| FGS | $r_{ap,src}$ | APEC | | | | POWERLAW | | | APEC+POWERLAW | | | | | |
|---|---|---|---|---|---|---|---|---|---|---|---|---|---|---|
| | | $kT_{apec}$ [keV] | $Z_{apec}$ [$Z_\odot$] | $norm^a_{apec}$ [$10^{-3}$] | $\chi^2$/d.o.f ($\chi^2_r$) | $\Gamma_{PL}$ | $norm^b_{PL}$ [$10^{-4}$] | $\chi^2$/d.o.f ($\chi^2_r$) | $kT_{apec}$ [keV] | $Z_{apec}$ [$Z_\odot$] | $norm^a_{apec}$ [$10^{-3}$] | $\Gamma_{PL}$ | $norm^b_{PL}$ [$10^{-4}$] | $\chi^2$/d.o.f ($\chi^2_r$) |
| 24 | 2.7' | $4.96^{+1.59}_{-0.91}$ | $0.5^{+0.48}_{-0.38}$ | $4.4^{+0.6}_{-0.6}$ | 68/35 (1.95) | $1.87^{+0.14}_{-0.13}$ | $8.7^{+1.0}_{-1.0}$ | 67/36 (1.86) | $0.19^{+6.67}_{-0.18}$ | 0.3 | $9.6^{+1102.2}_{-11.9}$ | 1.8 | $8.2^{+0.7}_{-5.0}$ | 66/35 (1.9) |

[a] $\text{norm}_{\text{apec}} = \frac{10^{-14}}{4\pi[D_A(1+z)]^2} \int n_e n_H dV \text{cm}^{-5}$

[b] $\text{norm}_{\text{PL}}$ has units of photons $\text{keV}^{-1}$ $\text{cm}^{-2}$ $\text{s}^{-1}$ $\text{arcmin}^{-2}$ at 1 keV

## 2.11 Appendix: Characterizing the Suzaku XRT PSF

We determine a radial model for the *Suzaku* XRT PSF to complete our image analysis in Section 2.5.2. Our PSF characterization employs archival observations of the X-ray point source SS Cyg observed for an effective 52 ks between 2005 November 18 and 19 (*Suzaku* sequence number 400007010). We clean the SS Cyg event files following the same procedure applied to our *Suzaku* observations (see Section 2.3).

The PSF is characterized using the radial profile of the stacked XIS0+XIS1+XIS3 image of SS Cyg that has been extracted in the 0.5–10 keV energy range and normalized to 1 (Fig. 2.7). The average PSF full width at half-maximum (FWHM) is found to be $\sim 35$ arcsec. Our PSF model consists of the sum of two exponentials, as recommended by Sugizaki et al. (2009), and thus the model fit to the SS Cyg brightness profile is:

$$S(r) = A_1 \mathrm{e}^{c_1(r-r_{0,1})} + A_2 \mathrm{e}^{c_2(r-r_{0,2})} + k, \tag{2.6}$$

where the constant $k$ accounts for the background. The best-fitting parameters for this model are recorded in Table 2.8.

Table 2.8 : Best-fitting model to the radial brightness profile of SS Cyg.

| Component | Parameter | Value | Units |
|---|---|---|---|
| exp1 | $A_1$ | $0.46^{+0.16}_{-0.45}$ | counts arcsec$^{-2}$ |
| | $c_1$ | $-2.5^{+0.01}_{-0.01}$ | $10^{-2}$ arcsec$^{-1}$ |
| | $r_{0,1}$ | $0.9^{+115.4}_{-61.6}$ | arcsec |
| exp2 | $A_2$ | $0.54^{+2.57}_{-0.54}$ | counts arcsec$^{-2}$ |
| | $c_2$ | $-9.2^{+0.1}_{-0.1}$ | $10^{-2}$ arcsec$^{-1}$ |
| | $r_{0,2}$ | $6.0^{+38.9}_{-174.7}$ | arcsec |
| background | $k$ | $9.2^{+0.1}_{-0.1}$ | $10^{-4}$ counts arcsec$^{-2}$ |
| $\chi^2$/d.o.f($\chi^2_r$) | | 405/53 (7.6) | |

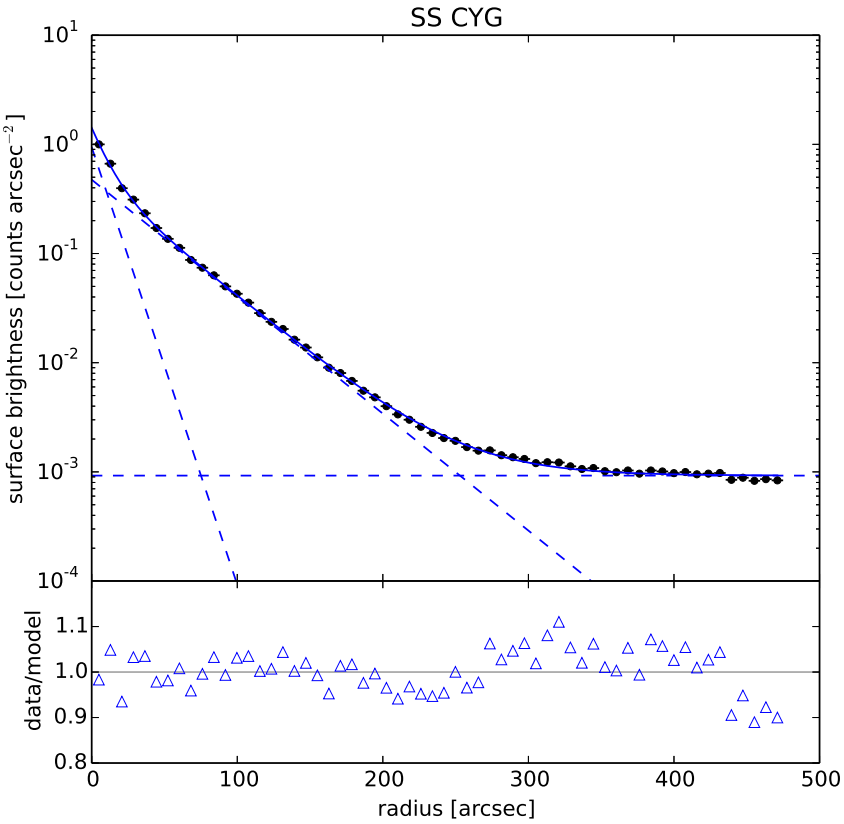


**Figure 2.7** : Stacked and normalized XIS0+XIS1+XIS3 radial brightness profile for point source SS Cyg in the 0.5–10 keV band. The best-fitting model, consisting of the sum of two exponentials and a background constant, is plotted in solid blue. Components of the model are plotted with dashed lines, and residuals are plotted as triangles. Best-fitting parameters for the model are recorded in Table 2.8.

## 2.12 Appendix: Notes on the Sample

*FGS03* is a Z14 verified fossil system. The AGN (2MASX J07524421+4556576) associated with the BCG of this system is both confirmed in the optical (Véron-Cetty & Véron 2010) and radio. The radio emission from this object consists of strong bipolar jets extending 57 arcsec (Hess et al. 2012). This AGN has also been identified as a Type I Seyfert (Stern & Laor 2012), and appears to dominate the X-ray emission observed from FGS03. The spectrum of this object is better fit by a power-law ($\chi^2_r = 1.02$) than a thermal model ($\chi^2_r = 1.17$), and no improvement in the fit occurs when a thermal component is

added to the power-law model. Furthermore, our imaging analysis finds a $\beta$-model poorly describes the observed surface brightness profile. Z14 find a velocity dispersion of $\sigma_v = 259$ km s$^{-1}$, the smallest dispersion of the S07 catalogue. Such a low velocity dispersion is typically associated with a cool ICM temperature, which would explain why there appears to be very little thermal emission when compared to a very bright AGN.

*FGS04* is a fossil candidate and has the coolest measured ICM of our sample ($T_{\rm X}$ = 2.81 keV). The BCG of this system contains the blazar NVSS J080730+340042 (Massaro et al. 2009) and in the radio, Hess et al. (2012) find bipolar jets originating from this source. We do not see evidence of contribution from this object in the spectral analysis - the spectrum of FGS04 is fit significantly better by a thermal model than a power-law (compare a $\chi^2_r$ of 1.14 to 1.43).

*FGS09* is a fossil candidate system at $z = 0.125$. A background $z = 0.73$ AGN (QSO B1040+0110; RA=10:43:03.84, Dec.=+00:54:20.42) is located 15 arcsec from the peak X-ray coordinates of FGS09. This AGN is confirmed in the optical (Véron-Cetty & Véron 2010) and the radio (Hess et al. 2012) bands. Based on our surface brightness profile and spectral analyses, this AGN is significantly contributing to the observed projected X-ray emission of FGS09. A large reduced chi-squared of $\chi^2_r$=5.7 is found for the $\beta$-model fit to the radial brightness profile. And, a power-law model ($\chi^2_r = 0.92$) fits the spectrum of FGS09 much better than the thermal model ($\chi^2_r = 1.08$).

*FGS14* is a confirmed fossil system and is the largest, hottest, and most X-ray luminous cluster in our sample, with $r_{500} = 1$ Mpc, $T_{\rm X} = 5.3$ keV, and $L_{\rm X} = 7.7 \times 10^{44}$ erg s$^{-1}$. Hess et al. (2012) detected radio-loud emission from two central sources; however, we did not see evidence of X-ray bright non-thermal emission in our spectral tests.

*FGS15* is a rejected fossil candidate (Z14). There are a number of contaminating sources in the XIS FOV of this source. A radio-loud AGN with an asymmetric jet is

associated with the BCG of this system (Hess et al. 2012). Within 40 arcsec of the peak system X-ray, the background ($z = 0.45$) quasar [VV2010] J114803.2+565411 has been identified optically and in the radio (Véron-Cetty & Véron 2010; Hess et al. 2012). Of the two visually distinguishable point sources excluded in our analysis, the object closest to the centre of the system is spatially consistent with the QSO [VV2010] J114755.9+564948 at $z = 4.32$ (Véron-Cetty & Véron 2010). The further south removed point source is located at (RA=11:48:08.38, Dec.=+56:48:18.64). The closest known spatial match to this object is the radio source NVSS J114838+565327 located ∼2 arcmin away. Our surface brightness profile analysis reveals that a $\beta$-model ($\chi^2_r$=5.2) poorly fits the observed emission, and additionally the best-fitting spectral model of FGS15 is a power-law. For this object, it is possible multiple AGN are contributing to the observed emission; however, as noted by Z14, FGS15 could also be a filament due to its small number of constituent galaxies with large differences in velocity.

*FGS24* is a rejected fossil candidate. No associated AGN were identified in the literature. However, the spectrum of FGS24 is better fit by a power-law than a thermal model (compare a $\chi^2_r$ of 1.33 to 1.38). FGS24 was observed during a period of potentially strong SWCX emission. While we found the best-fitting spectral parameters of the full observation match those of the isolated time interval of low proton flux, it is possible SWCX contamination is occurring even during this interval, obscuring the emission from FGS24.

*FGS25* is a non-fossil galaxy cluster (Z14). It is the second hottest cluster in our sample with $T_{\rm X} = 3.92$ keV and a corresponding estimated mass of $M_{500} = 2.4 \times 10^{14}$ $M_\odot$. Hess et al. (2012) find a radio-loud central point source in this cluster; however, our spectral analysis indicates no point source contribution as the FGS25 spectrum is much better described by a thermal model ($\chi^2_r = 0.96$) than a power-law model ($\chi^2_r = 1.26$).

*FGS26* is a Z14 confirmed fossil with $T_{\rm X} = 3.3$ keV and $L_{\rm X} = 0.8 \times 10^{44}$ erg s$^{-1}$. We find no associated significant non-thermal signatures in the spectrum.

*FGS27* is a confirmed fossil with measured global properties of $T_{\rm X} = 3.3$ keV and $L_{\rm X} = 3.4 \times 10^{44}$ erg s$^{-1}$. Our spectral analysis does not indicate contribution of significant non-thermal emission.

*FGS30* is a confirmed fossil with measured global properties of $T_{\rm X} = 3.4$ keV and $L_{\rm X} = 3.06 \times 10^{44}$ erg s$^{-1}$. A radio-loud AGN (2MASX J17181198+5639563) is associated with its bright central galaxy (Hess et al. 2012). The spectrum of FGS30 is better described by the thermal model ($\chi^2_r = 1.05$) in comparison to the power-law model ($\chi^2_r = 1.41$).

*Acknowledgments.*

This research has made use of data obtained from the *Suzaku* satellite, a collaborative mission between the space agencies of Japan (JAXA) and the USA (NASA). We thank the anonymous referee for valuable comments, K. Hamaguchi and K. Pottschmidt at the *Suzaku* Helpdesk for useful advice on multiple aspects of our analysis, and D. Eckert for helpful discussions and for suggesting the flickering pixels issue as an explanation for the excess in the 0.5–0.7 keV range.

Support for this research was provided by NASA Grant No. NNX13AE97G, and by the University of Wisconsin-Madison Office of the Vice Chancellor for Research and Graduate Education with funding from the Wisconsin Alumni Research Foundation. FG acknowledges the financial contribution from contract PRIN INAF 2012 ('A unique dataset to address the most compelling open questions about X-ray galaxy clusters') and the contract ASI INAF NuSTAR I/037/12/0. ED gratefully acknowledges the support of the Alfred P. Sloan Foundation. MG acknowledges funding from MIUR PRIN2010-2011 (J91J12000450001). JALA has been partly funded from MINECO AYA2013-43188-

P. EMC is partially supported by Padua University through grants 60A02-4807/12, 60A02-5857/13, 60A02-5833/14, and CPDA133894. JMA acknowledges support from the European Research Council Starting Grant (SEDmorph; PI V. Wild).

**References**

Aguerri, J. A. L., Girardi, M., Boschin, W., et al. 2011, A&A, 527, A143

Akritas, M. G., & Bershady, M. A. 1996, ApJ, 470, 706

Anders, E., & Grevesse, N. 1989, Geochim. Cosmochim. Acta, 53, 197

Arnaud, M., Pointecouteau, E., & Pratt, G. W. 2005, A&A, 441, 893

Bahcall, N. A., & Kulier, A. 2014, MNRAS, 439, 2505

Barnes, J. E. 1989, Nature, 338, 123

Böhringer, H., Voges, W., Huchra, J. P., et al. 2000, ApJS, 129, 435

Böhringer, H., Schuecker, P., Guzzo, L., et al. 2004, A&A, 425, 367

Buote, D. A., Gastaldello, F., Humphrey, P. J., et al. 2007, ApJ, 664, 123

Cavaliere, A., & Fusco-Femiano, R. 1976, A&A, 49, 137

—. 1978, A&A, 70, 677

Cravens, T. E. 2000, ApJ, 532, L153

Cypriano, E. S., Mendes de Oliveira, C. L., & Sodré, Jr., L. 2006, AJ, 132, 514

Dariush, A., Khosroshahi, H. G., Ponman, T. J., et al. 2007, MNRAS, 382, 433

Dariush, A. A., Raychaudhury, S., Ponman, T. J., et al. 2010, MNRAS, 405, 1873

Desjardins, T. D., Gallagher, S. C., Hornschemeier, A. E., et al. 2014, ApJ, 790, 132

Doe, S., Nguyen, D., Stawarz, C., et al. 2007, in Astronomical Society of the Pacific Conference Series, Vol. 376, Astronomical Data Analysis Software and Systems XVI, ed. R. A. Shaw, F. Hill, & D. J. Bell, 543

Donahue, M., Horner, D. J., Cavagnolo, K. W., & Voit, G. M. 2006, ApJ, 643, 730

D'Onghia, E., Sommer-Larsen, J., Romeo, A. D., et al. 2005, ApJ, 630, L109

Eckmiller, H. J., Hudson, D. S., & Reiprich, T. H. 2011, A&A, 535, A105

Eisenstein, D. J., Annis, J., Gunn, J. E., et al. 2001, AJ, 122, 2267

Ettori, S., Gastaldello, F., Leccardi, A., et al. 2010, A&A, 524, A68

Fabian, A. C., & Barcons, X. 1992, ARA&A, 30, 429

Fujimoto, R., Mitsuda, K., Mccammon, D., et al. 2007, PASJ, 59, 133

Girardi, M., Giuricin, G., Mardirossian, F., Mezzetti, M., & Boschin, W. 1998, ApJ, 505, 74

Girardi, M., Manzato, P., Mezzetti, M., Giuricin, G., & Limboz, F. 2002, ApJ, 569, 720

Girardi, M., & Mezzetti, M. 2001, ApJ, 548, 79

Girardi, M., Aguerri, J. A. L., De Grandi, S., et al. 2014, A&A, 565, A115

Harrison, C. D., Miller, C. J., Richards, J. W., et al. 2012, ApJ, 752, 12

Hess, K. M., Wilcots, E. M., & Hartwick, V. L. 2012, AJ, 144, 48

Hogg, D. W. 1999, ArXiv Astrophysics e-prints, arXiv:astro-ph/9905116

Hudson, D. S., Mittal, R., Reiprich, T. H., et al. 2010, A&A, 513, A37

Ishibashi, W., & Courvoisier, T. J.-L. 2010, A&A, 512, A58

Ishisaki, Y., Maeda, Y., Fujimoto, R., et al. 2007, PASJ, 59, 113

Jones, L. R., Ponman, T. J., & Forbes, D. A. 2000, MNRAS, 312, 139

Jones, L. R., Ponman, T. J., Horton, A., et al. 2003, MNRAS, 343, 627

Kalberla, P. M. W., Burton, W. B., Hartmann, D., et al. 2005, A&A, 440, 775

Kawaharada, M., Okabe, N., Umetsu, K., et al. 2010, ApJ, 714, 423

Kelly, B. C. 2007, ApJ, 665, 1489

Khosroshahi, H. G., Gozaliasl, G., Rasmussen, J., et al. 2014, MNRAS, 443, 318

Khosroshahi, H. G., Maughan, B. J., Ponman, T. J., & Jones, L. R. 2006, MNRAS, 369, 1211

Khosroshahi, H. G., Ponman, T. J., & Jones, L. R. 2007, MNRAS, 377, 595

Kuntz, K. D., & Snowden, S. L. 2000, ApJ, 543, 195

Kushino, A., Ishisaki, Y., Morita, U., et al. 2002, PASJ, 54, 327

Lovisari, L., Reiprich, T. H., & Schellenberger, G. 2015, A&A, 573, A118

Massaro, E., Giommi, P., Leto, C., et al. 2009, A&A, 495, 691

Maughan, B. J., Giles, P. A., Randall, S. W., Jones, C., & Forman, W. R. 2012, MNRAS, 421, 1583

Méndez-Abreu, J., Aguerri, J. A. L., Barrena, R., et al. 2012, A&A, 537, A25

Miller, E. D., Rykoff, E. S., Dupke, R. A., et al. 2012, ApJ, 747, 94

Milosavljević, M., Miller, C. J., Furlanetto, S. R., & Cooray, A. 2006, ApJ, 637, L9

Navarro, J. F., Frenk, C. S., & White, S. D. M. 1997, ApJ, 490, 493

Osmond, J. P. F., & Ponman, T. J. 2004, MNRAS, 350, 1511

Pointecouteau, E., Arnaud, M., & Pratt, G. W. 2005, A&A, 435, 1

Ponman, T. J., Allan, D. J., Jones, L. R., et al. 1994, Nature, 369, 462

Ponman, T. J., & Bertram, D. 1993, Nature, 363, 51

Popesso, P., Biviano, A., Böhringer, H., & Romaniello, M. 2007, A&A, 464, 451

Pratt, G. W., & Arnaud, M. 2005, A&A, 429, 791

Pratt, G. W., Croston, J. H., Arnaud, M., & Böhringer, H. 2009, A&A, 498, 361

Proctor, R. N., de Oliveira, C. M., Dupke, R., et al. 2011, MNRAS, 418, 2054

Rasmussen, J., & Ponman, T. J. 2007, MNRAS, 380, 1554

Santos, W. A., Mendes de Oliveira, C., & Sodré, Jr., L. 2007, AJ, 134, 1551

Serlemitsos, P. J., Soong, Y., Chan, K.-W., et al. 2007, PASJ, 59, 9

Stern, J., & Laor, A. 2012, MNRAS, 423, 600

Sugizaki, M., Kamae, T., & Maeda, Y. 2009, PASJ, 61, 55

Sun, M., Voit, G. M., Donahue, M., et al. 2009, ApJ, 693, 1142

Tawa, N., Hayashida, K., Nagai, M., et al. 2008, PASJ, 60, 11

Uchiyama, Y., Maeda, Y., Ebara, M., et al. 2008, PASJ, 60, 35

Véron-Cetty, M.-P., & Véron, P. 2010, A&A, 518, A10

Vikhlinin, A., Kravtsov, A., Forman, W., et al. 2006, ApJ, 640, 691

Voevodkin, A., Borozdin, K., Heitmann, K., et al. 2010, ApJ, 708, 1376

von Benda-Beckmann, A. M., D'Onghia, E., Gottlöber, S., et al. 2008, MNRAS, 386, 2345

Wu, X.-P., Xue, Y.-J., & Fang, L.-Z. 1999, ApJ, 524, 22

Yoshino, T., Mitsuda, K., Yamasaki, N. Y., et al. 2009, PASJ, 61, 805

Zarattini, S., Barrena, R., Girardi, M., et al. 2014, A&A, 565, A116

Zarattini, S., Aguerri, J. A. L., Sánchez-Janssen, R., et al. 2015, A&A, 581, A16

Zhang, Y.-Y., Andernach, H., Caretta, C. A., et al. 2011, A&A, 526, A105

# Chapter 3

# Are fossil groups early-forming galaxy systems?

*A version of this chapter has previously appeared in the* Astrophysical Journal

Kundert, A., D'Onghia, E., & Aguerri, J. A. L. 2017, ApJ, 845, 45

## Abstract

Using the Illustris cosmological simulation, we investigate the origin of fossil groups in the $M_{200} = 10^{13} - 10^{13.5} M_{\odot}/h$ mass regime. We examine the formation of the two primary features of fossil groups: the large magnitude gap between their two brightest galaxies, and their exceptionally luminous brightest group galaxy (BGG). For fossils and non-fossils identified at $z = 0$, we find no difference in their halo mass assembly histories at early times, departing from previous studies. However, we do find a significant difference in the recent accretion history of fossil and non-fossil halos; in particular, fossil groups show a lack of recent accretion and have in majority assembled 80% of their $M_{200}(z = 0)$ mass before $z \sim 0.4$. For fossils, massive satellite galaxies accreted during this period have enough time to merge with the BGG by the present day, producing a more massive central galaxy. In addition, the lack of recent group accretion prevents replenishment of the bright satellite population, allowing for a large magnitude gap to develop within the past few Gyr. We thus find that the origin of the magnitude gap and overmassive BGG of fossils in Illustris depends on the recent accretion history of the groups and merger history of the BGGs after their collapse at $z \sim 1$. This indicates that selecting galaxy groups by their magnitude gap does not guarantee obtaining either early-forming galaxy systems or undisturbed central galaxies.

## 3.1 Introduction

Fossil galaxy systems have long been thought to be dynamically evolved due to both a central galaxy that dominates the total optical luminosity of the group as well as a large difference in brightness between their two brightest satellites. Barnes (1989) proposed that within a Hubble time, satellites within a compact group will merge with the central galaxy due to dynamical friction, to produce a singular bright massive central galaxy in the center of a group-sized dark matter halo. And indeed, the first identification of one of such systems was made by Ponman et al. (1994), finding that the group RX J1340.6+4018 was an apparently isolated early-type galaxy surrounded by a X-ray halo with similar luminosity as a galaxy group.

The first observational definition for fossil groups (FGs), proposed by Jones et al. (2003), selected galaxy systems with an X-ray luminosity exceeding $L_{\rm X} \geq 10^{42} h_{50}^{-2}$ erg s$^{-1}$, and a magnitude gap greater than 2 mags in the $R$-band within half the projected virial radius. The $L_{\rm X}$ requirement was motivated to select group and cluster mass systems, and the 2 mag or greater magnitude gap criterion selected the most extreme end of the observed magnitude gap distribution. Furthermore, calculating the gap within half the virial radius ensured $L^*$ galaxies initially at this distance have had time to merge with the central galaxy within a Hubble time. Using this definition, fossil systems have been observed at all masses (see Cypriano et al. 2006; Mendes de Oliveira et al. 2006; Aguerri et al. 2011; Zarattini et al. 2014). Additionally, the galaxy luminosity functions of fossils identified in this way indicate their galaxy population depends on their magnitude gap. In particular, FGs have been found to show luminosity functions with a fainter characteristic magnitude as well as a slightly shallower faint-end slope (Zarattini et al. 2015), possibly due to a deficit of dwarf

galaxies (D'Onghia & Lake 2004).

Initial observations by Jones et al. (2000, 2003) indicated fossil BGGs had experienced no major mergers within the past 4 Gyr, and, in combination with the idea that $L^*$ galaxies had merged with the central galaxy, suggested fossil groups had built up their mass at an early epoch. Thus it was expected that both the halo and the BGG of fossil groups were old, and these systems have been evolving passively since their formation to the present day. However, this picture of dynamically evolved fossil groups has become less clear as larger samples of fossil groups have been studied.

The BGGs of fossil systems are among the brightest and most massive galaxies in the Universe (Méndez-Abreu et al. 2012). In addition, there is a relation between the brightness of the central galaxies and the magnitude gap of the systems. Systems with larger magnitude gaps show brighter central galaxies (e.g., Zarattini et al. 2014); and moreover, the fraction of optical luminosity contained in the central galaxies of fossil systems is larger than in non-fossils (Harrison et al. 2012; Zarattini et al. 2014). However, the BGGs in fossil systems follow the same scaling relations as non-fossil BGGs (Méndez-Abreu et al. 2012); and, no differences between fossil and non-fossil BGGs have been found in works related with stellar population properties (e.g., La Barbera et al. 2009; Trevisan et al. 2017). Studies focused on spatially resolved stellar population parameters, such as age and metallicity gradients, confirm that the BGG population of fossil systems are not a homogeneous class of objects. Additionally, the mass of fossil BGGs has been growing through merger events active until recent cosmic epochs (see e.g., Eigenthaler & Zeilinger 2013; Proctor et al. 2014).

The scaling relations describing the intracluster medium (ICM) of fossil and non-fossil systems have been a matter of debate in the literature. Some works have claimed that fossil systems are different to non-fossils in their optical luminosity (Proctor et al.

2011; Khosroshahi et al. 2014), X-ray temperature (Khosroshahi et al. 2007), or the central concentration parameter of the dark matter halo (e.g., Sun et al. 2004). Nevertheless, these differences are not confirmed by studies of large samples of FGs (e.g., Voevodkin et al. 2010; Harrison et al. 2012; Girardi et al. 2014; Kundert et al. 2015; Pratt et al. 2016).

The galaxy substructure of fossil groups has also been analyzed in several studies in the literature. The absence of galaxy substructure is considered an indication of the dynamical relaxation of the system, which would be expected if fossil groups are truly dynamically old. Aguerri et al. (2011) analyzed one FG finding no significant galaxy substructure. Nevertheless, the study from Zarattini et al. (2016) on a larger sample of fossils, found that FGs show similar amounts of galaxy substructure as non-FGs. In addition, no differences have been found on the large-scale structure around fossil systems. Thus, some of them appear to be isolated structures, while in contrast others are embedded in denser environments (e.g., Adami et al. 2007, 2012; Pierini et al. 2011).

In the present work we analyze the properties of fossils identified in the Illustris cosmological simulation. Our aim is to examine the properties of the groups selected from the simulation as a function of their magnitude gap in order to understand their dynamical evolution. We will focus our study on the the evolution of the magnitude gap of the systems, the formation and evolution of the BGGs, and the mass assembly history of the group halos.

The structure of this paper is as follows: Section 3.2 is a brief overview of the Illustris simulation, with our sample of selected groups described in Section 3.3. The results are presented in Section 3.4 including an examination of the evolution of the magnitude gap (Sec. 3.4.1), and the properties of the brightest group galaxies (Sec. 3.4.2) and the group halos (Sec. 3.4.3). The discussion and conclusions of the paper are given in Sections 3.5

and 3.6, respectively.

## 3.2 The Illustris Simulation

The Illustris Project comprises a suite of cosmological simulations of varying resolution with hydrodynamics performed on a moving-mesh using AREPO (Springel 2010). For our analysis of the evolution of fossil groups we make use of Illustris-1, the highest resolution simulation containing baryons in the Illustris suite. Illustris-1 contains $1820^3$ dark matter (DM) particles of mass $4.4 * 10^6 M_\odot/h$, and initially $1820^3$ gas cells of average mass $8.9 * 10^5 M_\odot/h$. The gravitational softening length for DM particles is 1.42 co-moving kpc for the duration of the simulation. For stellar particles, the gravitational softening length is 0.71 kpc at $z = 0$, and fixed to the DM softening length at $z \geq 1$. Gas cells and DM, stellar, and black hole particles are evolved within a periodic box of side length 75 co-moving Mpc/$h$ from initial cosmological conditions at $z = 127$ to $z = 0$, with 136 snapshots recorded between $z = 47$ and the present.

The full-physics galaxy formation model of Illustris includes subgrid prescriptions for star formation and evolution; gas chemical enrichment with cooling and heating; black hole seeding and growth; and feedback from supernovae and AGN. Free-parameters in the feedback model were tuned to match observations, such as the evolution of the cosmic star formation rate density, in preliminary smaller volume test simulations (Vogelsberger et al. 2013). The output galaxy population produced in Illustris reproduces a number of observations including the galaxy luminosity function at $z = 0$ (Vogelsberger et al. 2014), as well as the galaxy stellar mass function between $z = 0 - 7$ (Genel et al. 2014), in addition to others.

We utilize the halo and subhalo catalogues provided by the Illustris team (Nelson et al. 2015), with relevant properties described here in brief. Group halos have been identified

in the dark matter distribution using a friends-of-friends (FOF) algorithm (Davis et al. 1985) with a linking length 0.2 times the average interparticle separation. Within FOF group halos of at minimum 32 DM particles, gravitationally bound subhalos are identified from the total particle distribution using the SUBFIND algorithm (Springel et al. 2001; Dolag et al. 2009). Group centers and subhalo centers are set to be the coordinates of their most bound particle. The most massive subhalo in a group halo is considered the central subhalo. A FOF group's $R_{200}$ is defined to be the radius that encloses an average total particle density equal to 200 times the critical density. The $M_{200}$ of a group is calculated from the total mass of all baryons and dark matter enclosed within $R_{200}$.

SUBLINK merger trees have been constructed for Illustris by Rodriguez-Gomez et al. (2015). We trace the evolution of groups by following the main progenitor branch (MPB) of their $z = 0$ central subhalos, and the properties of the groups these MPB subhalos inhabit at a given snapshot. For our analysis, we select groups at $z = 0$ with a central subhalo whose MPB has been identified as centrals of their FOF groups at previous snapshots out to at least $z = 0.1$. This ensures we are able to robustly track the evolution of the groups during the recent epoch.

We focus our analysis on subhalos with a total bound stellar mass exceeding $\log(M_*[M_\odot/h]) \geq 8$, for the purpose of requiring $\sim$100 stellar particles per galaxy. This cut in the stellar mass of subhalos produces a completeness limit in magnitude of $M_r = -16$ mag, as calculated from the summed luminosities of all bound subhalo stellar particles.

Illustris was run using WMAP-9 cosmological parameters (Hinshaw et al. 2013). Complete details of the Illustris simulations and the galaxy formation model are described in Vogelsberger et al. (2014) and Vogelsberger et al. (2013), respectively. Throughout this paper, we have made use of the publicly available online Illustris database (Nelson et al.

2015).

## 3.3 The Sample

To understand the dynamical evolution of fossil groups, we examine the formation of the magnitude gap, $\Delta m_{12}$, defined by the difference in $r$-band brightness between the first-ranked, $m_1$, and second-ranked, $m_2$, galaxies. The division between fossils (FGs) and non-fossils (nFGs) has traditionally been set at a gap of 2 mags, where fossils have a gap of $\Delta m_{12}(\mathrm{FG}) \geq 2$, and non-fossils have a gap of $\Delta m_{12}(\mathrm{nFG}) = 0 - 2$. We examine the evolution of the gap determined within both a volume with radius $0.5R_{200}$ centered around the BGG, and within a volume with radius $R_{200}$.

We restrict our analysis of the formation of the gap to groups with mass $M_{200} = 10^{13} - 10^{13.5} M_{\odot}/h$. Observationally, groups with this mass are expected to meet the $L_{\mathrm{X}}$ requirement of Jones et al. (2003), see e.g. Eckmiller et al. (2011), although perhaps not all groups of this mass will be virialized. We do not rely on the X-ray luminosity, as is used in observational studies, because in Illustris the gas mass fraction within the inner regions of groups in our mass regime has been found to be a factor of 3-10 times lower than compared to observations, as noted in Genel et al. (2014). The upper limit of our $M_{200}$ selection is set to ensure a large enough sample size of both fossils and non-fossils. In the right panel of Fig. 3.1, we show the distribution of magnitude gap and $M_{200}$ calculated for all FOF groups with mass $M_{200} \geq 10^{13} M_{\odot}/h$. As can be seen above $10^{13.5} M_{\odot}/h$, which we do not include in our analysis, there are few non-fossils available for comparison to fossils, particularly for fossils and non-fossils defined by their gap within $0.5R_{200}$. Thus we find the mass regime $M_{200} = 10^{13} - 10^{13.5} M_{\odot}/h$ is best for both examining the formation of the gap in a narrow group mass regime, as well as for comparing a significant sample size of fossils and non-fossils.

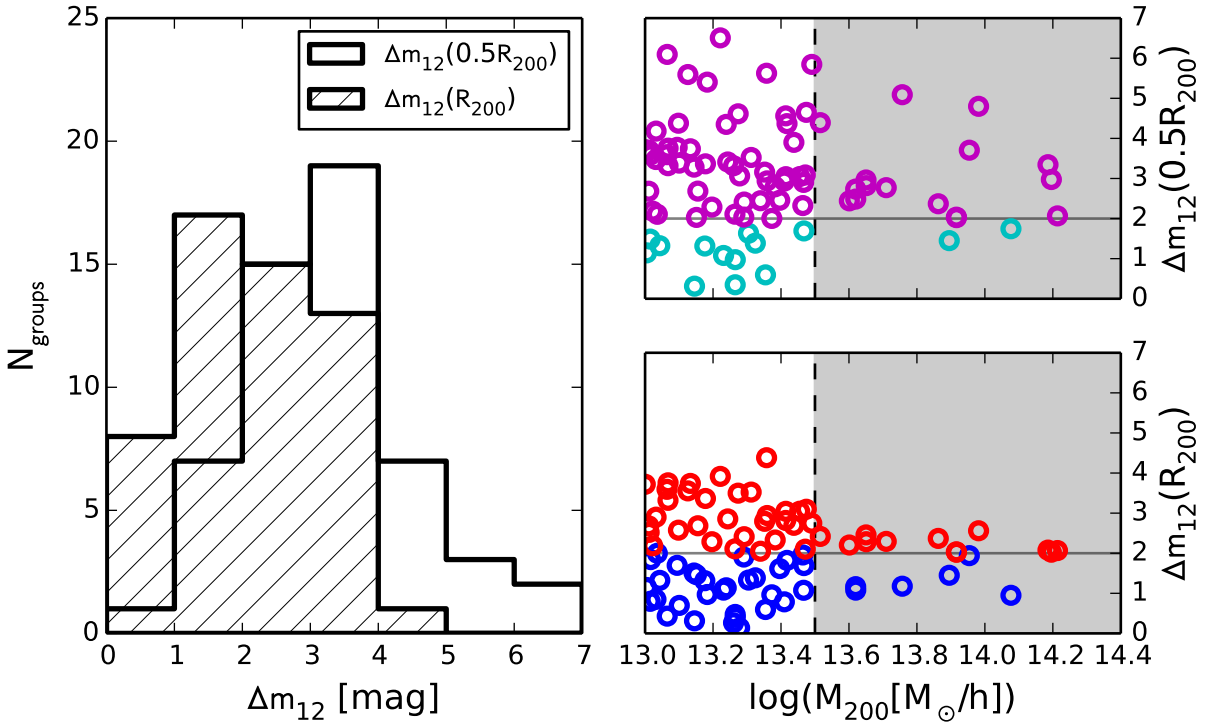


**Figure 3.1** : *Left:* Magnitude gap distribution for Illustris groups with $\log(M_{200}[M_\odot/h])$=13-13.5; shown for $\Delta m_{12}$ calculated within $0.5R_{200}$ (solid histogram) and within $R_{200}$ (hatched histogram). *Right:* Relation between magnitude gap and $M_{200}$. The shaded region is not used in our analysis, but is shown here to demonstrate the overall trend of magnitude gap and mass. Cyan and magenta circles represent non-fossils and fossils, respectively, identified by their gap within $0.5R_{200}$. Blue and red circles represent non-fossils and fossils, respectively, identified by their gap within $R_{200}$.

Our final sample of groups ($M_{200} = 10^{13} - 10^{13.5} M_\odot/h$) identified at $z = 0$ consists of 46 FG($0.5R_{200}$) and 8 nFG($0.5R_{200}$), defined by their gap within $0.5R_{200}$; as well as 29 FG($R_{200}$) and 25 nFG($R_{200}$), defined by their gap within $R_{200}$. The properties of these subsamples are recorded in Table 3.1, including average group $M_{200}$ mass, $R_{200}$ radius, and number of member galaxies.

Fig. 3.1, left panel, shows the distribution of the magnitude gap values calculated for our sample of groups. For the gap calculated within $R_{200}$, we find a peak at $\Delta m_{12}(R_{200}) \sim 1.5$, with 54% of groups classified as FG($R_{200}$). Analytically, as predicted

Table 3.1 : Sample Properties

| Subsample | $\Delta m_{12}$ | $N_{\rm groups}$ | $\log(M_{200})$ | $R_{200}$ [Mpc] | $N_{\rm gal}(R_{200})$ | $N_{\rm gal}(0.5R_{200})$ |
|---|---|---|---|---|---|---|
| nFG($0.5R_{200}$) | 0-2 | 8 | 13.2 ± 0.2 | 0.41 ± 0.05 | 20 ± 11.2 | 7 ± 4.4 |
| FG($0.5R_{200}$) | $\geq 2$ | 46 | 13.3 ± 0.2 | 0.42 ± 0.05 | 19 ± 9.1 | 7 ± 3.4 |
| nFG($R_{200}$) | 0-2 | 25 | 13.2 ± 0.2 | 0.42 ± 0.05 | 20 ± 8.3 | 7 ± 3.9 |
| FG($R_{200}$) | $\geq 2$ | 29 | 13.3 ± 0.2 | 0.42 ± 0.05 | 19 ± 10.3 | 7 ± 3.3 |

*Note.* Properties of subsamples based on the magnitude gap within $0.5R_{200}$ and $R_{200}$ for groups in the mass regime $\log(M_{200}[M_\odot/h])$=13-13.5. $M_{200}$, $R_{200}$, and the number of galaxies, $N_{\rm gal}$, are average values for the subsample.

by the Press-Schechter formalism, 5-40% of groups are expected to have magnitude gaps larger than 2 mags as calculated in a 500 kpc projected radius, with the distribution peak at $\Delta m_{12} \sim 1$ for groups of mass log(M)=13.5 (Milosavljević et al. 2006); we thus find a comparable magnitude gap distribution within $R_{200}$ as has been predicted. However, we find the peak of the gap distribution defined within $0.5R_{200}$ occurs at $\Delta m_{12}(0.5R_{200}) \sim 3$, producing a relative abundance of 80% fossils. In comparison, the FG($0.5R_{200}$) abundance is estimated from observations to be 8-20% of groups with $\log(L_{\rm X,bol}[\rm erg\ s^{-1}]) \geq 42$ (Jones et al. 2003).

Differences between the Illustris gap distribution and those observationally found within $0.5R_{200}$ might arise for a few reasons: (1) The central galaxies in Illustris are overmassive and overbright, compared to observations, as a result of the simulation feedback prescription (Vogelsberger et al. 2013; Genel et al. 2014); (2) Overmerging of satellite galaxies within the central regions of the groups is a known problem in simulations (Katz & White 1993); (3) We do not employ the X-ray luminosity criterion that has been applied to previous observational studies. The overabundance of Illustris fossils, as compared to observations, has also been noted and discussed in Raouf et al. (2016).

We also see in Fig. 3.1, a number of extreme gap, $\Delta m_{12}(0.5R_{200}) \geq 4$, groups exist in our FG($0.5R_{200}$) subsample. These very large gap groups have a $m_2(z=0)$ galaxy that

is too faint to meet the completeness limit of many observational studies, and as a result these type of extreme gap objects have rarely been observed (although see Zarattini et al. 2014). However, 15/16 of these extreme gap groups have at higher redshift had a bright satellite pass within $0.5R_{200}$, that has not merged, but has moved outside of this region at $z = 0$ due to the path of its orbit. And indeed 15/46 of all FG($0.5R_{200}$) have had a current satellite within 2 magnitudes of the brightness of the central galaxy pass within $0.5R_{200}$ in the past without merging, indicating they would have been classified as non-fossil at other snapshots and are by chance currently identified as fossil in the present snapshot.

We also here note that the magnitude gap of an individual group is a highly transitory feature. The infall of new bright satellites accreted by the group will act to decrease the magnitude gap, while mergers of bright satellite galaxies with the BGG will cause the gap to increase. Additionally, the orbits of satellite galaxies within the group will produce a variance in the gap unrelated to mergers or infall, causing the gap to vary on short timescales particularly when the gap is calculated within half of $R_{200}$. The average maximum variance in $\Delta m_{12}(0.5R_{200})$ is $\sim 2$ mag since $z \sim 0.1$. While for $\Delta m_{12}(R_{200})$ it is $\sim 0.7$ mag. It is clear that with a variance of 2 mags within the past Gyr for groups defined by their $\Delta m_{12}(0.5R_{200})$ gap, there will also be a large variance in the properties of subsamples sorted by this metric at $z = 0$.

Thus while the magnitude gap is traditionally defined within $0.5R_{200}$ (Jones et al. 2003), we find an overabundance of FG($0.5R_{200}$) compared to observations and additionally find $\Delta m_{12}(0.5R_{200})$ is highly affected by the orbits of its satellites which obscures information about the dynamical state of groups characterized in this way. Most of our tests in our later analysis (Section 3.4) indeed show no statistical difference between FG($0.5R_{200}$) and nFG($0.5R_{200}$). On the other hand, while $\Delta m_{12}(R_{200})$ is less typically used, the abundance of FG($R_{200}$) are in order with predictions and observations, and we would expect

little effect due to orbits, and as a result a less transient gap characteristic. We therefore mostly rely on comparing groups divided into samples by their $R_{200}$ gap to understand the physical processes driving the evolution of the magnitude gap. We will primarily depend on the results of this subsample for our understanding of the dynamical state of fossils, but also present the results within $0.5R_{200}$ following observational convention.

## 3.4 Results

### 3.4.1 Evolution of the magnitude gap

Fossil groups are characterized by both their large magnitude gap as well as an overluminous central galaxy (Jones et al. 2003). In Fig. 3.2 we investigate how the evolution of these two characteristics are related. In the upper row of Fig. 3.2, we present the evolution of $\Delta m_{12}(z)$ within $R_{200}$ (left) and $0.5R_{200}$ (right) for fossils and non-fossils defined by their gap at $z = 0$. To further understand the $\Delta m_{12}(z)$ evolution, we also include in the middle rows the evolution of $m_1(z)$ and $m_2(z)$, the brightness of the first- and second-ranked galaxies identified at each redshift. Because the magnitude gap and $m_2(z)$ galaxy brightness are transitory properties for individual groups, particularly within $0.5R_{200}$, we display the magnitude gap and brightness of $m_1(z)$ and $m_2(z)$ averaged over a timespan of 1 Gyr in the first three rows. In the bottom row, we show the averaged fraction of a group's mass contained in the BGG's stellar component, which for convenience we refer to as $f^*(\mathrm{BGG})=M_{*,\mathrm{BGG}}/M_{200,\mathrm{group}}$. This $f^*(\mathrm{BGG})$ quantity is useful for comparing the relative mass of the BGG for its halo mass. We divide these plots into three redshift regimes: $z \geq 1$, $z = 0.3 - 1$, and $z \leq 0.3$, during which we observe different phases in the evolution of the groups.

Prior to $z \sim 1$, all groups have similar magnitude gaps and $f^*(\mathrm{BGG})$; this epoch

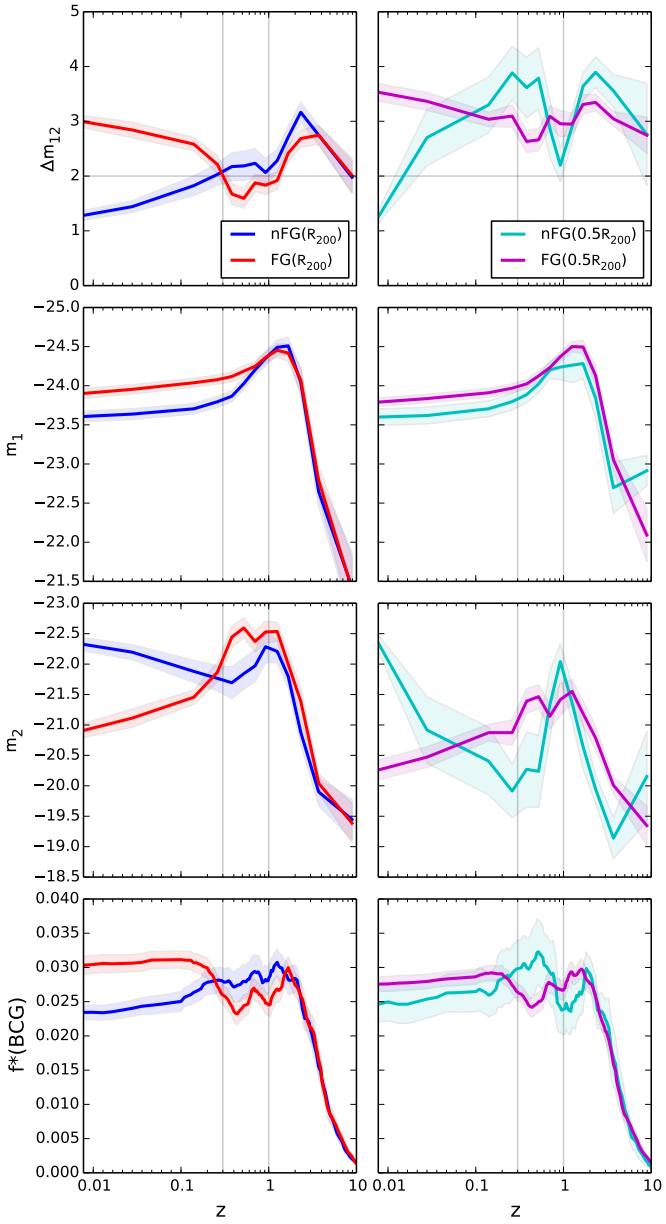


**Figure 3.2** : Average evolution of properties of fossils and non-fossils identified at $z = 0$ and defined by $\Delta m_{12}(R_{200})$ (*left*) and $\Delta m_{12}(0.5R_{200})$ (*right*). *First row:* magnitude gap calculated between first- and second-ranked galaxies at each redshift. Plotted values have been averaged over 1 Gyr intervals to reduce scatter due to the high degree of transience of the gap. *Second row:* brightness of first-ranked galaxy identified at each redshift, $m_1(z)$. *Third row:* brightness of second-ranked galaxy identified at each redshift, $m_2(z)$. *Fourth row:* ratio of the BGG stellar mass to group $M_{200}$ at each redshift, i.e. $f^*(\mathrm{BGG})=M_{*,\mathrm{BGG}}(z)/M_{200,\mathrm{group}}(z)$. $1\sigma$ errors calculated from 1000 bootstrap resamplings are shown.

marks the time period when these groups are still in the process of assembling the majority of their halo mass. During $z \leq 1$, we can clearly see the evolution of the magnitude gap and the evolution of $f^*$(BGG) are related: groups with large magnitude gaps also have large $f^*$(BGG). Between $z \sim 0.3 - 1$, groups identified as FG($z = 0$) are shown to have a smaller gap and lower $f^*$(BGG) ratio than their nFG($z = 0$) counterparts. After $z \sim 0.3$, we see these trends reverse such that by the present day FG($z = 0$) have a larger magnitude gap and greater $f^*$(BGG) than nFG($z = 0$). We thus see that the characteristically large magnitude gap of fossils identified at $z = 0$ has formed only in the past few Gyr, and furthermore both fossils and non-fossils have evolved in their magnitude gap and ratio of BGG mass to halo mass since $z \sim 1$.

These trends support the idea of a 'fossil phase' as proposed by von Benda-Beckmann et al. (2008); fossils identified at $z = 0$ were non-fossils at high redshift, while $z = 0$ non-fossils were previously fossils. Indeed we find all $z = 0$ identified fossils have been previously non-fossils, while all $z = 0$ non-fossils have been previously fossil. In general, the average FG($R_{200}$)($z = 0$) was last non-fossil $\sim$3 Gyr ago, while nFG($R_{200}$)($z = 0$) were on average fossil $\sim$2 Gyr ago. And importantly, we find the relative overmassiveness of the BGG followed with large magnitude gap systems, such that when $z = 0$ non-fossils had a large magnitude gap between $z = 0.3 - 1$, they also had a relatively more massive $f^*$(BGG). Thus we would expect a sample of fossils identified at higher redshifts would also have a more massive BGG than non-fossils identified at the same redshift, although the magnitude gap will likely evolve by the present day.

### 3.4.2 Properties of the BGG

To understand how fossils obtain their characteristic overmassive BGG, in this section we investigate BGG scaling relations, stellar mass assembly history, and merger history.

#### 3.4.2.1 Scaling relations

Observationally, the central galaxies of fossil groups have been found to be more luminous and more massive than the central galaxies in non-fossil groups of the same global X-ray luminosity and temperature (Harrison et al. 2012; Zarattini et al. 2014). Furthermore, the centrals of fossil groups have been found to reside on the most massive end of the Faber-Jackson relation (Méndez-Abreu et al. 2012). The group scaling relations of total optical luminosity ($L_r$) and bolometric X-ray luminosity ($L_{\rm X}$) are consistent for both fossil and normal groups (Harrison et al. 2012; Girardi et al. 2014; Kundert et al. 2015), indicating a similar amount of baryonic mass. However a significant fraction of a fossil group's total optical luminosity is contributed by its central galaxy, suggesting, in combination with the $L_r$-$L_{\rm X}$ relations and large magnitude gap, that fossils have their stellar mass distributed differently than non-fossils.

Qualitatively matching these observational studies, we indeed find that the fossil BGGs in Illustris are more massive than non-fossil BGGs, and this characteristic is reflected in the distributions of BGG $r$-band brightness, peak circular velocity, and central velocity dispersion (Fig. 3.3).

In Fig. 3.4, left panel, we present the scaling relations of BGG stellar mass and group $M_{200}$, along with the least squares best-fit relation. It can be clearly seen that the BGGs of FG($R_{200}$) are more massive than the BGGs of nFG($R_{200}$) residing in halos of the same mass, qualitatively matching the observed scaling relations results. Furthermore, a two-sample Kolmogorov-Smirnov (KS) test on the ratio of the BGG stellar mass to the group $M_{200}$, $f^*$(BGG)=$M_*$(BGG)/$M_{200}$(group), strongly indicates the $f^*$(BGG) of FG($R_{200}$) and nFG($R_{200}$) follow a different distribution ($p_{\rm KS} = 0.001$). In Fig. 3.4, right panel, we also find the magnitude gap and the BGG stellar mass are correlated for the gap calculated

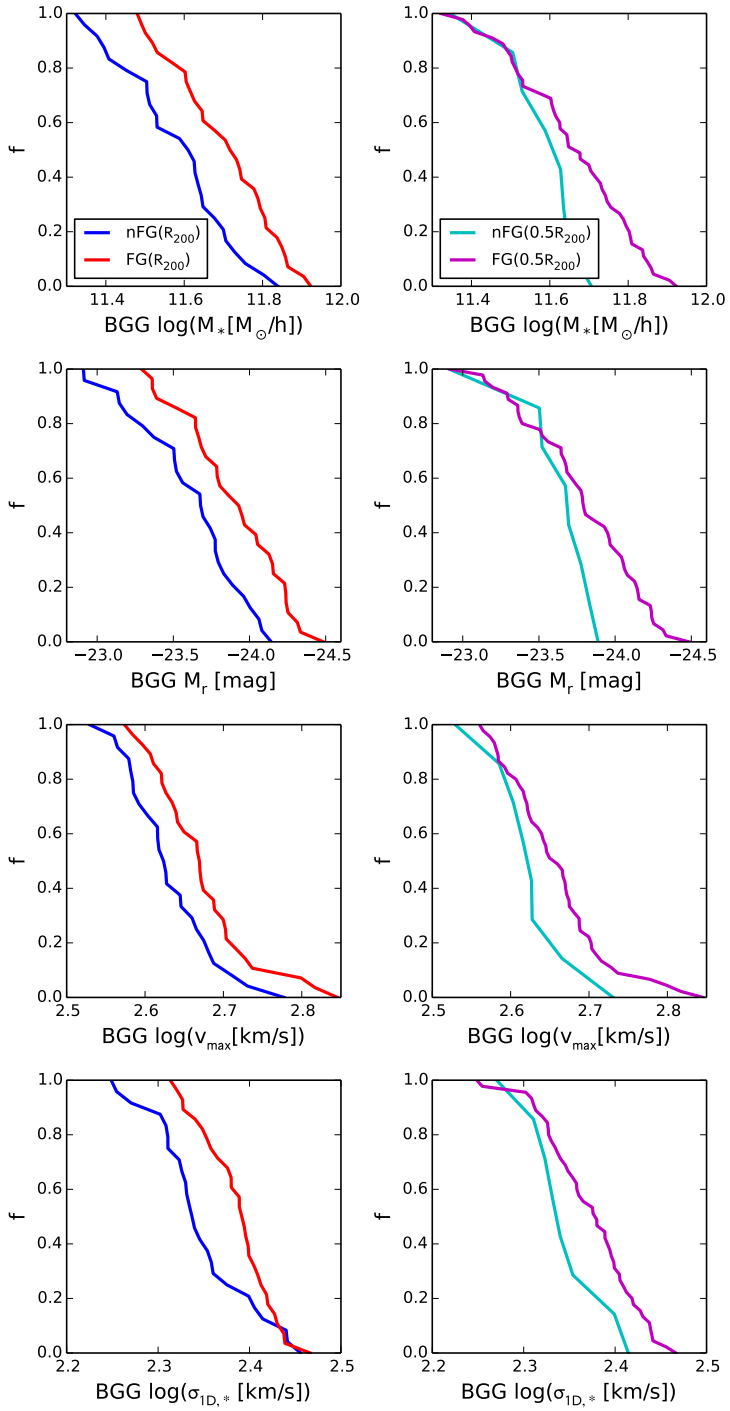


**Figure 3.3** : Distribution of BGG stellar mass, $r$-band magnitude, peak rotation curve circular velocity, and 1D velocity dispersion. Here the velocity dispersion has been calculated for the stellar particles within the stellar half-mass radius of the BGG.

within $R_{200}$, (Spearman $\rho = 0.45$, $p = 0.0007$), with the largest gap groups possessing the most massive BGGs. This suggests the mechanisms which produce an overmassive FG($R_{200}$) BGG are related to the physical processes that produce the magnitude gap, in good agreement with observations (e.g., Harrison et al. 2012; Zarattini et al. 2014).

However, as also revealed in Fig. 3.4, comparing fossils and non-fossils defined by their $\Delta m_{12}(0.5R_{200})$ gap does not produce statistically different results. A two-sample KS test of the ratio of BGG stellar mass and group $M_{200}$ for nFG($0.5R_{200}$) and FG($0.5R_{200}$) shows no difference in their distributions with $p_{\rm KS} = 0.69$. And in testing for correlation

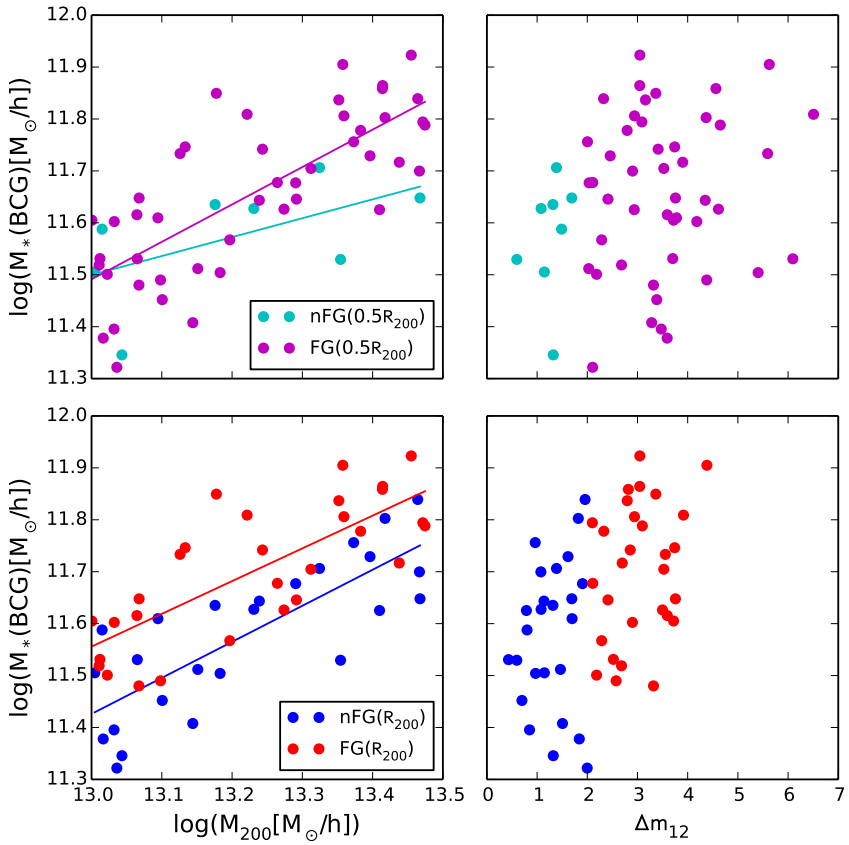


**Figure 3.4** : *Left*: Stellar mass of BGG compared to the $M_{200}$ mass of the group in which it resides. Fossil($R_{200}$) BGGs are found to be more massive than non-fossil($R_{200}$) BGGs for the same group mass. *Right*: A positive trend is found between the magnitude gap $\Delta m_{12}(R_{200})$ and BGG stellar mass: the most massive central galaxies reside in the largest magnitude gap systems.

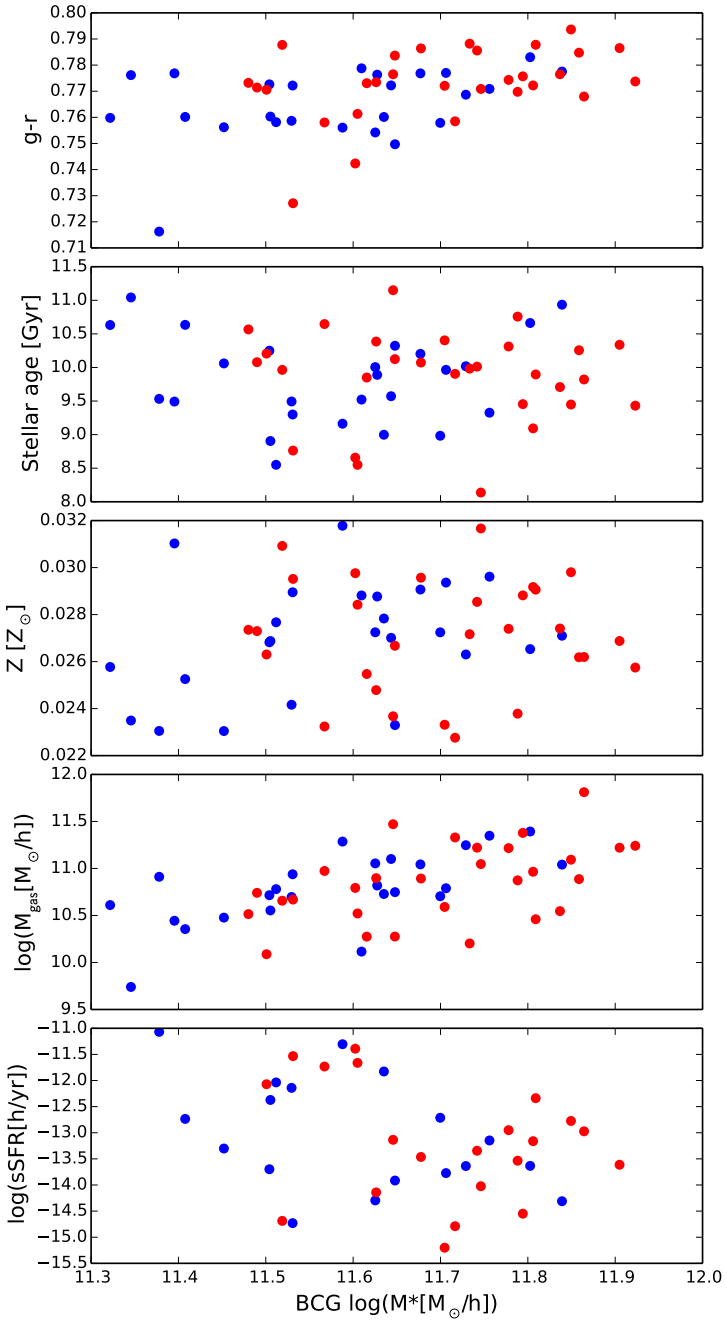


**Figure 3.5** : Average mass-weighted $z = 0$ properties for BGGs. Fossil($R_{200}$) BGGs, shown in red, and non-fossil($R_{200}$) BGGs, shown in blue, are similar in observable properties.

between $\Delta m_{12}(0.5R_{200})$ and $M_{200}$, the Spearman test returns $\rho = 0.18$, $p = 0.19$. This further supports $\Delta m_{12}(0.5R_{200})$ is highly affected by random chance, i.e., the location of satellite galaxies along their orbital paths as discussed in Section 3.4.1. It will thus be difficult to disentangle the effects driving how FG($0.5R_{200}$) BGGs become overmassive and overluminous.

Despite the large $f^*$ of FG($R_{200}$) BGGs, in Fig. 3.5 we find no obvious difference in the color, stellar age and metallicity, total gas mass, and specific star formation rate (sSFR) of the central galaxies of the same stellar mass. All BGGs have a log(sSFR[$M_\odot$/yr])≤-11, which is typically considered to be quenched at $z = 0$. As might be expected, no differences are found when comparing the observational properties of BGGs separated by $\Delta m_{12}(0.5R_{200})$.

#### 3.4.2.2 BGG stellar mass assembly history

Given that fossil BGGs are overmassive and overluminous for their group $M_{200}$, we here examine how these galaxies build up their mass over time. In Fig. 3.6, we show the average stellar mass assembly history (bottom) of the central galaxies, as well as the assembly history normalized by the final $z = 0$ stellar mass (top).

The average evolution of the BGG stellar mass shows fossil central galaxies experience significant growth over the range $z \sim 0.1 - 1$ relative to non-fossil BGGs. Indeed between $z = 0 - 1$, FG($R_{200}$) BGGs increase in mass on average by a factor of $2.5 \pm 0.20$, compared to a factor of $1.9 \pm 0.14$ shown by nFG($R_{200}$) BGGs. However, we note that while fossil BGGs are on average more massive, they are still less than a factor of 2 more massive than the nFG BGGs at $z = 0$.

The normalized BGG stellar mass assembly history reveals FG($R_{200}$) BGGs have assembled 50% of their final stellar mass by $z_{50}(\mathrm{BGG}, *) = 1.0 \pm 0.1$, while for nFG($R_{200}$)

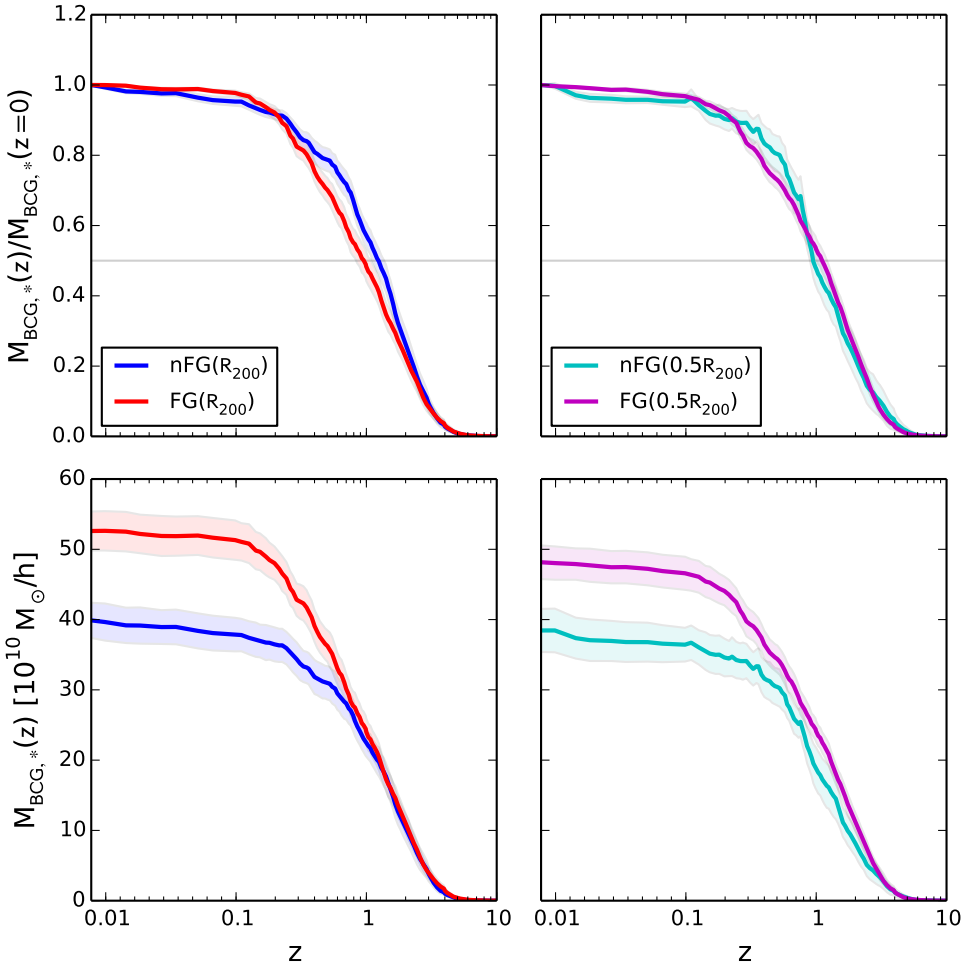


**Figure 3.6** : *Top*: Average normalized stellar mass assembly history for central galaxies. *Bottom*: Average stellar mass assembly history for central galaxies. $1\sigma$ errors calculated from 1000 bootstrap resamplings are shown.

BGGs we find $z_{50}(\mathrm{BGG},*) = 1.3 \pm 0.1$ (Table 3.2). Thus by this metric fossil BGGs have more recently assembled their stellar component, which is complementary to finding increased mass growth of the fossil BGGs after $z \sim 1$. For FG($0.5R_{200}$) and nFG($0.5R_{200}$), we find no differences in the rate at which the stellar component is assembled, but do find FG($0.5R_{200}$) BGGs grow more in mass after $z \sim 1$ compared to nFG($0.5R_{200}$), similar to our finding for FG($R_{200}$).

Table 3.2 : BGG mass assembly

| Subsample | $z_{50}$(BGG,*) | $N_{major}$ | $z_{LMM}$ |
|---|---|---|---|
| nFG($0.5R_{200}$) | $1.1 \pm 0.1$ | $2.9 \pm 0.3$ | $0.7 \pm 0.1$ |
| FG($0.5R_{200}$) | $1.2 \pm 0.1$ | $3.2 \pm 0.2$ | $1.0 \pm 0.2$ |
| nFG($R_{200}$) | $1.3 \pm 0.1$ | $2.7 \pm 0.2$ | $1.1 \pm 0.2$ |
| FG($R_{200}$) | $1.0 \pm 0.1$ | $3.5 \pm 0.3$ | $0.8 \pm 0.2$ |

*Note.* Average BGG stellar mass assembly time $z_{50}$(BGG,*), number of major mergers $N_{major}$, and redshift of last major merger $z_{LMM}$. $1\sigma$ errors have been bootstrapped.

#### 3.4.2.3 BGG merger history

Differences in the stellar mass assembly history of fossil and non-fossil BGGs are likely to result from differences in their merger histories. In Fig. 3.7, we show the major merger history of the BGGs, both in the evolution of the cumulative number of major mergers as well as the time of the last major merger. We here consider a major merger as a merger between galaxies with stellar mass ratios $M_{*,\mathrm{satellite}}/M_{*,\mathrm{BGG}} \geq 0.25$. Following Rodriguez-Gomez et al. (2015), the merger ratio between galaxies is calculated from the mass of both galaxies at the snapshot when the secondary galaxy is at its most massive. This avoids numerical effects and the transfer of mass shortly prior to when the merger of the galaxies occurs.

For FG($R_{200}$) and nFG($R_{200}$) BGGs, we find a difference in major merging history. Fig. 3.7 shows that FG($R_{200}$) BGGs will experience $\sim 1$ more major merger than nFG($R_{200}$) BGGs. The distribution of the redshift of the last major merger, $z_{\mathrm{lmm}}$, is also shifted to more recent times for FG($R_{200}$) BGGs as also shown in Fig. 3.7. Additionally, $\sim 50\%$ of FG($R_{200}$) BGGs experience 2 or more major mergers between $z = 0 - 1$, compared to 20% of nFG($R_{200}$) BGGs. No significant difference is found in the number of major mergers for FG($0.5R_{200}$) and nFG($0.5R_{200}$) BGGs.

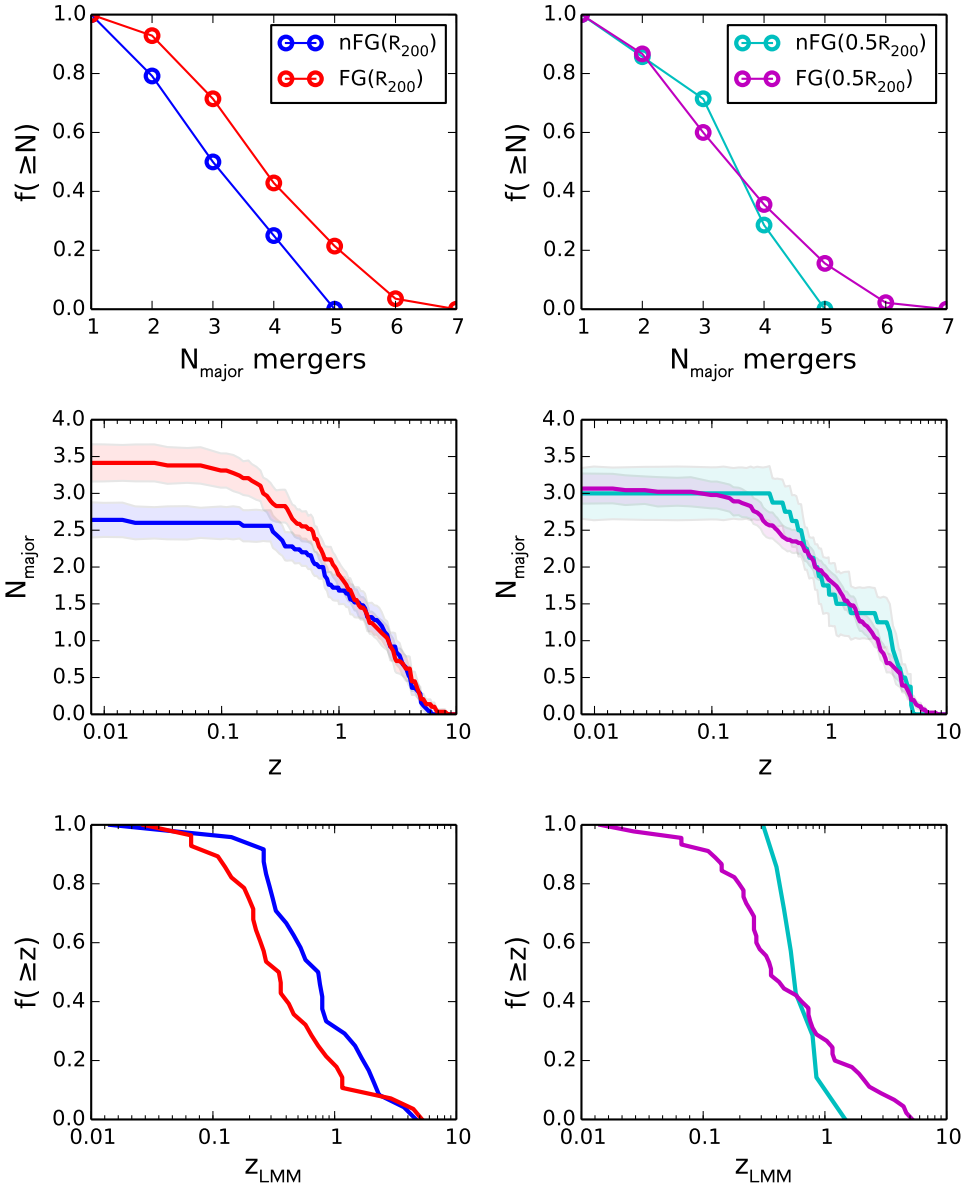


**Figure 3.7** : *Top row*: distribution of the total number of major mergers experienced by the BGGs at $z = 0$. *Middle row*: average number of cumulative major mergers across $z$. *Bottom row*: distribution of the redshift of the last major merger of the BGGs.

In Fig. 3.8, we examine the amount of mass the BGGs acquire through merging(major+minor), major merging, minor merging, and in situ star formation according to the Illustris stellar assembly catalog of Rodriguez-Gomez et al. (2016). In this catalog, star particles bound to $z = 0$ galaxies are traced back and categorized by their origin location.

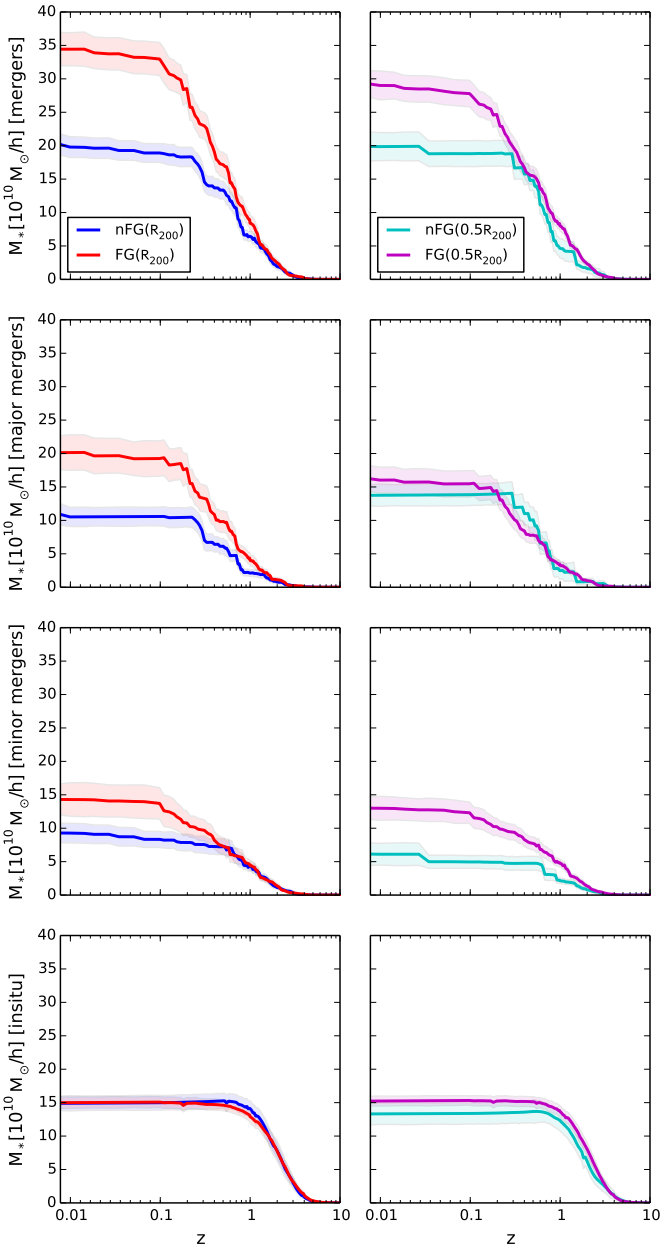


**Figure 3.8** : The average BGG stellar mass at each redshift originating from mergers (*first row*), major mergers (*second row*), minor mergers (*third row*), and in situ formation (*fourth row*). $1\sigma$ errors from 1000 bootstrap resamplings are shown.

For a given galaxy, in situ stars were formed from gas cells bound to the main progenitor branch of the galaxy, while star particles acquired from mergers were identified as having formed in a progenitor that has merged with the galaxy's main progenitor branch.

FG($R_{200}$) BGGs build up on average 64% of their stellar mass through mergers (major+minor), compared to 50% of mass acquired through mergers for nFG($R_{200}$) BGGs. This $\sim 15$ percentage point difference is due to a $\sim 10$ percentage point greater contribution from major merging and a $\sim 5$ percentage point difference in minor merging for FG($R_{200}$) BGGs over nFG($R_{200}$) BGGs. On the other hand, in situ star formation contributes a similar amount of stellar mass for both FG($R_{200}$) and nFG($R_{200}$) BGGs. Thus mergers, and especially major mergers, seem primarily responsible for elevating the mass of FG($R_{200}$) BGGs over their nFG($R_{200}$) BGG counterparts between $z \sim 0.1 - 1$.

The stellar mass contribution results for the groups defined by their $\Delta m_{12}(0.5R_{200})$ gap are less clear. Fig. 3.8 suggests the main difference between FG($0.5R_{200}$) BGGs and nFG($0.5R_{200}$) BGGs is in the mass acquired through minor merging, however we note that the FG($0.5R_{200}$) BGGs and nFG($0.5R_{200}$) BGGs also have similar masses for the same group $M_{200}$ (see Fig. 3.4).

In summary, we have found $\Delta m_{12}(R_{200})$ improves the identification of BGGs that are relatively overmassive for their group $M_{200}$. FG($R_{200}$) BGGs are statistically more massive and more luminous than nFG($R_{200}$) BGGs in group halos of the same $M_{200}$. FG($R_{200}$) BGGs assemble 50% of their final stellar mass somewhat later than nFG($R_{200}$) BGGs, and additionally are more likely to have a more recent major merger. The larger $f^*$ of FG($R_{200}$) BGGs is attributable to a greater amount of mass acquired through merging between $z = 0.1 - 1$, with increased contribution from major merging providing the most significant boost to the mass of the fossil BGG compared to the non-fossil BGG. While we have shown that there are indeed statistical differences in how and when the stellar

mass of FG($R_{200}$) and nFG($R_{200}$) BGGs is assembled, these differences do not produce any noticeable variations in observational properties such as color, stellar age, or sSFR.

### 3.4.3 Group mass assembly history

Given the difference in the BGG mass assembly of fossils and non-fossils shown in the previous section, we might expect a difference in how the groups assemble their halo mass. Here we examine the mass assembly history of the groups. Fig. 3.9 shows the average group $M_{200}$ assembly history normalized by the $M_{200}(z = 0)$ mass. The mass assembly history of the groups was determined by tracing back the BGG($z = 0$) main progenitor branch and using the associated group $M_{200}(z)$ at each redshift. Snapshots where the BGG($z = 0$) main progenitor was not identified as the BGG($z = 0$) of its group were excluded, and the missing $M_{200}(z)$ were estimated from linear interpolation. We compute a two-sample KS test on the fraction of mass assembled for the non-fossil and fossil sample at each redshift (top x-axis), as well as for the distribution in redshift at which a particular fraction of $M_{200}(z = 0)$ is assembled (right y-axis). We find the mass assembly histories of fossils and non-fossils are similar at early times, but show an apparent divergence occurring after $z \sim 1$.

In the literature, the redshift at which a halo builds up 50% of its final $M_{200}(z = 0)$ mass, $z_{50}$, has been frequently used as a metric for the formation time of the halo (e.g., Li et al. 2008). And historically, previous fossil studies have particularly been interested in this time of halo assembly. We find that all groups in our sample on average form at $z_{50} \sim 1$, although there is a wide range of $z_{50}$ times spanning $z_{50} = 0.1 - 2$. Unlike previous studies of the mass assembly history of fossil groups (e.g., Dariush et al. 2007; Díaz-Giménez et al. 2008; Dariush et al. 2010), we find no significant difference in the $z_{50}$ formation times with the KS test returning $p_{\rm KS} \sim 0.8$ for both FG($R_{200}$) and nFG($R_{200}$), as well as FG($0.5R_{200}$)

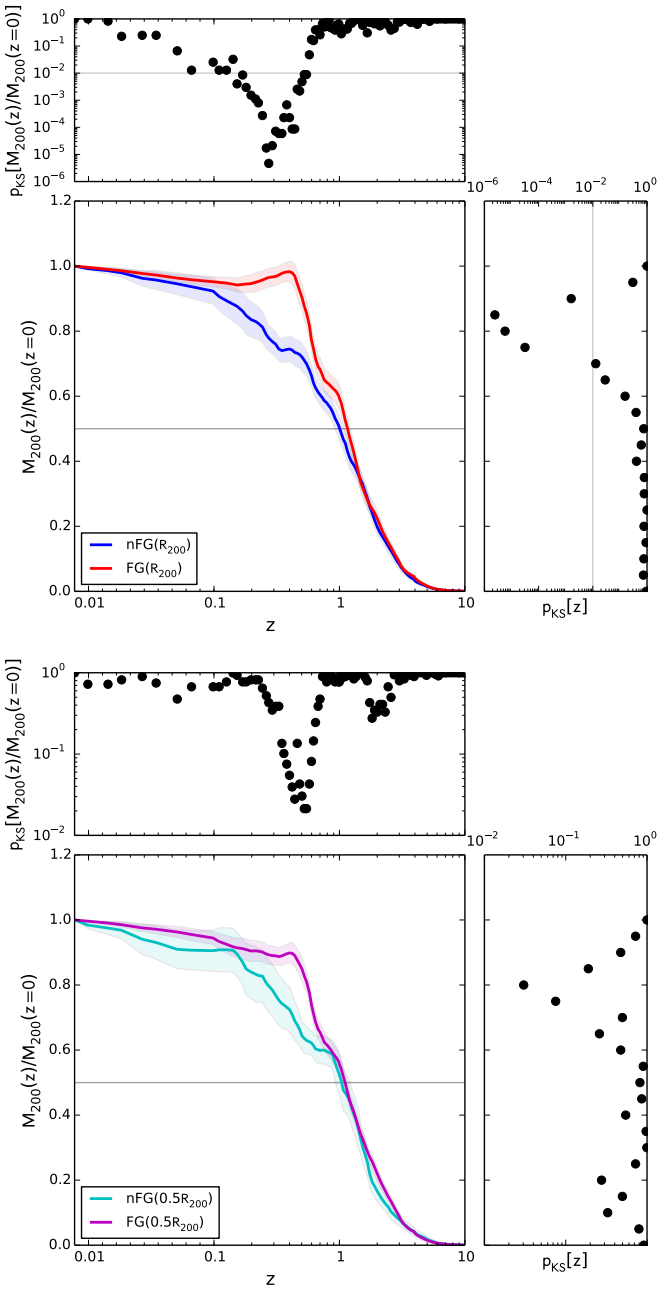


**Figure 3.9** : The average normalized group $M_{200}$ mass assembly history of fossils and non-fossils. $1\sigma$ errors from 1000 bootstrap resamplings are shown. *Top x-axis side panel*: the two-sample KS test between non-fossils and fossils for the fraction of mass assembled at a given redshift. *Right y-axis side panel*: the two-sample KS test between non-fossils and fossils for the redshift at which some fraction of the final $M_{200}$ is assembled, with $p_{\rm KS} = 0.01$ marked with a solid line. FG($R_{200}$) and nFG($R_{200}$) are different in their assembly epochs of $z_{70}$-$z_{90}$ with $p_{\rm KS} \leq 0.01$, and are different ($p_{\rm KS} \leq 0.01$) in the fraction of mass assembled between ∼2-5 Gyrs ago.

and nFG($0.5R_{200}$).

However, the difference in the recent accretion history of fossils and non-fossils is particularly clear for $z_{80}$, the redshift at which these groups acquire 80% of their final mass, as can be seen from the KS test in Fig. 3.9. On average $z_{80} = 0.58 \pm 0.05$ for FG($R_{200}$) and $z_{80} = 0.25 \pm 0.04$ for nFG($R_{200}$), with the KS test yielding $p_{\rm KS} = 6 * 10^{-6}$ on the $z_{80}$ distributions. A similar trend is also found for FG($0.5R_{200}$) and nFG($0.5R_{200}$) with $p_{\rm KS} = 3 * 10^{-2}$ for $z_{80}$ (Table 3.3).

In Fig. 3.10, we show the cumulative distribution function of $z_{50}$, for comparison to previous fossil studies, and $z_{80}$, which we find in Illustris to be the most divergent mass assembly time for fossils and non-fossils. It is clear from this figure, that the steep increase in $M_{200}(z)/M_{200}(z=0)$ shown in Fig. 3.9 for fossils between $z = 0.4 - 0.8$, is a result of a large fraction of the fossil sample reaching $z_{80}$ in this window. In contrast, the distribution of non-fossil $z_{80}$ times extends over $z = 0 - 0.8$ with the majority of non-fossils reaching $z_{80}$ between $z = 0 - 0.4$. In general, we find $z \sim 0.4$ to be a dividing line in the distribution of $z_{80}$ for FG($R_{200}$) and nFG($R_{200}$): $\sim$80% of fossils reach $z_{80}$ before $z \sim 0.4$, while $\sim 80\%$ of non-fossil reach $z_{80}$ after this time. Qualitatively, these results are also found with less significance for FG($0.5R_{200}$) and nFG($0.5R_{200}$).

A lack of recent halo accretion, as indicated by an early $z_{80}$, may indeed be

Table 3.3 : Mass assembly times of Illustris groups

| Subsample | $z_{50}$(group, $M_{200}$) | $z_{80}$(group, $M_{200}$) |
|---|---|---|
| nFG($0.5R_{200}$) | $0.85 \pm 0.16$ | $0.24 \pm 0.05$ |
| FG($0.5R_{200}$) | $1.02 \pm 0.06$ | $0.45 \pm 0.04$ |
| nFG($R_{200}$) | $0.90 \pm 0.08$ | $0.25 \pm 0.04$ |
| FG($R_{200}$) | $1.07 \pm 0.07$ | $0.58 \pm 0.05$ |

*Note.* Average redshift at which the groups assemble 50% and 80% of their final $M_{200}(z=0)$ mass. $1\sigma$ errors have been bootstrapped.

fundamental for the formation of a large gap within $R_{200}$ at the present day. In our mass regime, bright satellites originally were accreted as centrals of other groups, and their arrival is therefore associated with mass build up for the primary group. Thus an early $z_{80}$ ensures that no bright satellites fall in to the group, maintaining any gap that forms through mergers. While for non-fossils, the recent growth of their halos is related to the arrival of their brightest current satellites $m_2(z = 0)$. For non-fossils, $z_{80}$ must occur within the last few Gyr such that accreted bright satellites do not have time yet to merge with

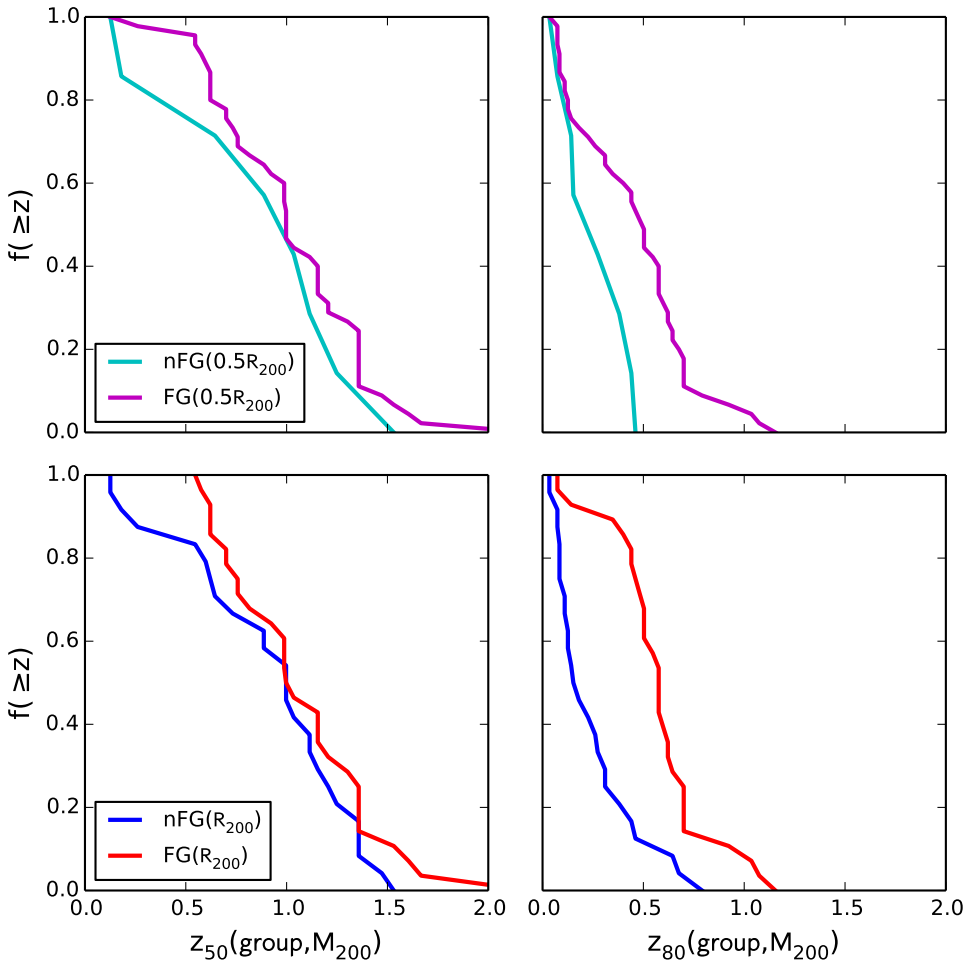


**Figure 3.10** : Distribution of group $z_{50}$ (*left*) and $z_{80}$(*right*) assembly times. Fossils and non-fossils are found to have a similar $z_{50}$, the redshift at which 50% of the final $z = 0$ $M_{200}$ mass is assembled. $z_{80}$, the redshift at which 80% of the final $z = 0$ halo mass is assembled, is significantly earlier for fossils than non-fossils, with most FG($R_{200}$) reaching $z_{80}$ before $z \sim 0.4$.

the central, while $z_{80}$ must occur early enough for fossils such that any bright satellites accreted during this time of halo mass growth have had time to merge by the present day.

We also here note that although we only find a difference in the recent accretion history of fossils and non-fossils, we also find fossils are associated with overmassive BGGs (Fig. 3.4), suggesting overmassive BGGs may also be associated with an early $z_{80}$ and not with $z_{50}$ as has been previously thought. As a direct check of the relation between halo assembly and the overmassiveness of the BGG, we select the most extreme 20% of the distribution of $z_{50}$ times for our groups to check for association with $f^*$(BGG). By a two-sample KS test on the $f^*$(BGG) values of the earliest and latest forming halos we find $f^*$(BGG) for extreme early and late $z_{50}$ are not distinct ($p_{\rm KS} = 0.7$). Comparatively, selecting the most extreme $z_{80}$ shows deviating distributions of $f^*$(BGG) ($p_{\rm KS} = 0.01$), where groups with an early $z_{80}$ are associated with an overmassive BGG. Thus we truly find overmassive BGGs are associated with early $z_{80}$ and thus lack of recent group accretion, instead of an early halo formation time. This can also explain properties of the evolution in $f^*$(BGG)($z$) shown in Fig. 3.2. While the average $f^*$(BGG)($z$) of fossils does indeed grow due to mergers in the past few Gyr, it is equally important that the average $f^*$(BGG)($z$) of non-fossils has decreased over this time due to recent halo-halo mergers contributing to the group $M_{200}$.

In summary, we find the main difference in the mass assembly history of fossils and non-fossil groups is with respect to the recent accretion history, instead of an early formation time as has been found in other studies. Particularly we find fossils on average reach $z_{80}$ at an earlier epoch than non-fossils, indicating a lack of recent accretion. This difference in $z_{80}$ suggests a difference in the local environment of FG($z = 0$) and nFG ($z = 0$) groups over the past few Gyr, namely that present day fossil groups may exist in a relatively less dense environment which has prevented recent infall of new massive satellites. And indeed,

this would be in agreement with previous studies of the environment in which fossil groups reside (Adami et al. 2007; Dariush et al. 2010; Cui et al. 2011; Díaz-Giménez et al. 2011).

## 3.5 Discussion

### 3.5.1 Comparison to other simulations

The initial Jones et al. (2003) formation scenario for the magnitude gap proposed a difference in the halo mass assembly history of fossil and non-fossil groups: the large magnitude gap of fossils formed as a result of early accreted massive satellites merging with the central galaxy, boosting the luminosity and mass of the central while depleting the bright end of the satellite population. Thus, testing how the magnitude gap relates to halo age has been of great interest to many theoretical fossil studies.

The mass assembly of fossil clusters ($M_{vir} \sim 10^{14} M_{\odot}$) was first investigated by D'Onghia et al. (2005), and later the mass assembly of fossils in the low mass group regime ($M_{200} = 10^{13} - 10^{13.5} M_{\odot}/h$) was examined using the Millennium simulation (Dariush et al. 2007, 2010; Gozaliasl et al. 2014) as well as using other N-body cosmological simulations (von Benda-Beckmann et al. 2008; Deason et al. 2013).

When examining the full mass assembly history of group halos, Dariush et al. (2007, 2010) and Gozaliasl et al. (2014) find fossils on average have assembled more of their final halo mass at nearly every redshift. Particularly they find the initial mass build up of fossils and non-fossils is different, including a difference in $z_{50}$ which is also returned by von Benda-Beckmann et al. (2008) and Deason et al. (2013). While according to these simulations the halo formation time on average is earlier for fossil systems, there is also a considerable amount of scatter relating halo formation time and the magnitude gap of the group. Indeed many early forming systems are missed by selecting large magnitude gap

groups and a non-significant amount of fossils also have a recent formation time (e.g. see Dariush et al. 2010; Deason et al. 2013; Raouf et al. 2014).

Our result of finding no difference in the $z_{50}$ of fossils and non-fossils in Illustris may then be related to the sample size of available Illustris groups in our selected mass regime compared to the much larger sample sizes of groups in the Millennium simulation used by the previous fossil studies. Given the large scatter previously reported in these studies, it is possible that by chance the distribution of $z_{50}$ for fossils is similar to the distribution for non-fossils in Illustris. The relative abundance of early-forming fossils will thus need to be examined in future larger cosmological simulations with hydrodynamics, such as the IllustrisTNG (Pillepich et al. 2017). However, even with our smaller sample size, we find $z_{80}$ is significantly different for fossils and non-fossils in Illustris. Thus we expect that with larger sample sizes, fossil groups should show also a lack of recent accretion as important to the formation of the magnitude gap. Nevertheless, an earlier $z_{80}$, as we find, or an earlier $z_{50}$, as has been found in other studies, suggests fossil groups assemble some portion of their halo mass at an earlier epoch than non-fossils, following the original Jones et al. (2003) idea.

We also find support for the idea of a 'fossil phase' (von Benda-Beckmann et al. 2008) whereby groups only temporarily exist with a large magnitude gap due to recent mergers of satellites with the central without recent infall of new satellites, in good agreement with previous studies of simulated fossils (von Benda-Beckmann et al. 2008; Dariush et al. 2010; Gozaliasl et al. 2014; Kanagusuku et al. 2016). As can be seen in our Fig. 3.2, we find that the large magnitude gap characterizing fossil groups at $z = 0$ has only formed within the past few Gyrs.

Thus the picture of fossil group formation we find in Illustris relies on both the early accretion of massive satellites in addition to the lack of recent accretion of new bright

satellites, both indicated by an early $z_{80}$. The early assembly of some fraction of a fossil group's halo mass allows enough time for $L*$ satellites to merge by the present day due to dynamical friction, producing a massive and luminous central galaxy. In combination, the lack of recent accretion for the halo ensures no new bright satellites replace those that have already merged and the gap formed through merging is preserved.

### 3.5.2 Observational implications

We find BGG properties consistent with what has been found in previous observational and theoretical studies, despite finding no difference in the $z_{50}$ group formation time of fossils and non-fossils. This may be because differences in group assembly have little effect on the assembly and properties of the BGG's stellar component; even large differences in the large-scale environment in which a halo forms do not show differences in BGG growth rate (Jung et al. 2014), and differences in the the group halo formation time have not been found to produce observable differences in the stellar age or properties of their BGGs (Deason et al. 2013).

We find no significant difference in the observational properties of fossil and non-fossil BGGs including color, sSFR, and stellar age. This is in good agreement with observational studies that find fossil BGGs seem to have typical properties of other ellipticals of the same mass, including the age and metallicity of stellar populations (La Barbera et al. 2009; Harrison et al. 2012; Eigenthaler & Zeilinger 2013) and number of globular clusters (Alamo-Martínez et al. 2012). Additionally observed fossil BGGs follow the Fundamental Plane, Kormendy relation, and Faber-Jackson relation (Méndez-Abreu et al. 2012).

There is also some recent evidence that fossil BGGs are not evolving passively, or at least not more passively than the BGGs of non-fossil groups. Evidence for recent fossil BGG activity includes: radio-loud AGN (Hess et al. 2012), surface brightness profiles that

deviate from a Sersic profile in the NIR (Méndez-Abreu et al. 2012) and optical (Alamo-Martínez et al. 2012), apparent shell features (Eigenthaler & Zeilinger 2012), unrelaxed X-ray isophotes (Miller et al. 2012), tidal tails (Zarattini et al. 2016), and ongoing merging in HST imaging (Ulmer et al. 2005). This is in line with the more recent last major merger and recent significant growth of the BGG due to merging we find for fossils, and as has been found in other theoretical studies as well (e.g. Díaz-Giménez et al. 2008; Kanagusuku et al. 2016).

Observations of the halo concentration parameter and X-ray scaling relations of fossil groups have often been interpreted with respect to the $z_{50}$ formation time found for fossils in previous simulation studies. Groups with an early $z_{50}$ are expected to have more concentrated halos for a given mass (e.g., Neto et al. 2007), and early-forming groups have been speculated to follow different scaling relations (e.g., Jones et al. 2003; Khosroshahi et al. 2007). However, a wide range of concentration parameters have been measured for fossil groups (e.g., Khosroshahi et al. 2004, 2006, 2007; Démoclès et al. 2010; Pratt et al. 2016), and fossil groups seem to follow the same scaling relations as normal groups (e.g., Harrison et al. 2012; Girardi et al. 2014; Kundert et al. 2015). These observations might be understood then if there is no difference in the $z_{50}$ of fossils and non-fossils, as we find here with Illustris. Furthermore, while we propose an early group $z_{80}$ is important for the development of the large magnitude gap of fossils at the present day, an early $z_{80}$, reflecting a lack of recent accretion, would be unlikely to affect the halo concentration or scaling relations.

## 3.6 Summary and conclusions

We investigate the formation of the optical magnitude gap for galaxy groups with mass $M_{200} = 10^{13} - 10^{13.5} M_{\odot}/h$ in the Illustris cosmological simulation. Our analysis relies

on studying the properties of fossil groups ($\Delta m_{12} \geq 2$) and non-fossils ($\Delta m_{12} = 0 - 2$) defined by their gap within $0.5R_{200}$ and $R_{200}$. The evolution of the groups is examined between $z = 0 - 10$ with particular focus on the BGG stellar mass assembly and merger history, and assembly of the $M_{200}$ group mass. No significant difference between FG and nFG defined by their gap within $0.5R_{200}$ is found, and thus we base our interpretation of the physical processes driving the formation of the gap on our analysis of FG and nFG defined by their gap within $R_{200}$.

Within $R_{200}$, approximately $\sim 0.4$ Mpc for our groups, the average gap of $\Delta m_{12}(R_{200}) \sim 1$ is consistent with Press-Schechter predictions. In agreement with observations, we find fossils have in general a more massive and more luminous central galaxy in comparison to non-fossils of the same group $M_{200}$, and additionally we find a significant correlation between the gap and the stellar mass of the BGG, implying both features are related and may have an origin due to the same process.

Our primary findings on the evolution of fossil group properties include:

- The magnitude gap, $\Delta m_{12} \geq 2$, of fossils identified at $z = 0$ on average forms $\sim 3$ Gyr ago, and is coincident with fossil BGGs becoming overmassive for their group $M_{200}$ mass compared to non-fossil BGGs on average. We furthermore find groups with a large magnitude gap at any redshift appear to also have a relatively more massive BGG than small magnitude gap groups.

- Fossil BGGs become more massive than non-fossil BGGs due to increased mass acquired through mergers between $z = 0.1 - 1$. Fossil BGGs are more likely to experience a greater number of major mergers, and more recently experience a major merger as compared to non-fossil BGGs. On average fossil BGGs have assembled $\sim 60\%$ of their mass at $z = 0$ from mergers, with the greatest contribution originating

from major mergers.

- While fossil BGGs both assemble 50% of their final stellar mass and experience their last major merger $\sim 1$ Gyr more recently than non-fossil BGGs, no difference is found in the observational properties of these BGGs including stellar ages, metallicities, and star formation rates.

- The group mass assembly of fossils and non-fossils differs in only the recent group accretion history, particularly as indicated by differences in the distribution of $z_{80}(M_{200})$ assembly times. $\sim 80\%$ of fossil groups reach $z_{80}$ before $z = 0.4$, while $\sim 80\%$ of non-fossil groups reach $z_{80}$ after this epoch. Unlike studies of fossils in other simulations, we find no difference in the $z_{50}(M_{200})$ of our groups, and in general no difference in the mass assembly histories of the groups at early times.

The primary difference between fossils and non-fossils is thus the mass assembly history of the group. The large magnitude gap and massive BGG of fossils is due to the merging of early arriving massive satellites, and lack of recent infall of new massive satellites over the past few Gyr. In Illustris, we find the magnitude gap of a group does not provide information on the dynamical state of the system, nor the age of the BGG, but instead seems primarily associated with the recent accretion history of the group within the past few Gyr.

*Acknowledgments.*

AK received support from the Chandra-NASA Archive Grant AR6-17015X. ED gratefully acknowledges the support of the Alfred P. Sloan Foundation. JALA was funded by the MINECO (grant AYA2013-43188-P).

The Illustris simulations were run on the Odyssey cluster supported by the FAS

Science Division Research Computing Group at Harvard University. We thank the Illustris collaboration for making their data and catalogs publicly available.

**References**

Adami, C., Russeil, D., & Durret, F. 2007, A&A, 467, 459

Adami, C., Jouvel, S., Guennou, L., et al. 2012, A&A, 540, A105

Aguerri, J. A. L., Girardi, M., Boschin, W., et al. 2011, A&A, 527, A143

Alamo-Martínez, K. A., West, M. J., Blakeslee, J. P., et al. 2012, A&A, 546, A15

Barnes, J. E. 1989, Nature, 338, 123

Cui, W., Springel, V., Yang, X., De Lucia, G., & Borgani, S. 2011, MNRAS, 416, 2997

Cypriano, E. S., Mendes de Oliveira, C. L., & Sodré, Jr., L. 2006, AJ, 132, 514

Dariush, A., Khosroshahi, H. G., Ponman, T. J., et al. 2007, MNRAS, 382, 433

Dariush, A. A., Raychaudhury, S., Ponman, T. J., et al. 2010, MNRAS, 405, 1873

Davis, M., Efstathiou, G., Frenk, C. S., & White, S. D. M. 1985, ApJ, 292, 371

Deason, A. J., Conroy, C., Wetzel, A. R., & Tinker, J. L. 2013, ApJ, 777, 154

Démoclès, J., Pratt, G. W., Pierini, D., et al. 2010, A&A, 517, A52

Díaz-Giménez, E., Muriel, H., & Mendes de Oliveira, C. 2008, A&A, 490, 965

Díaz-Giménez, E., Zandivarez, A., Proctor, R., Mendes de Oliveira, C., & Abramo, L. R. 2011, A&A, 527, A129

Dolag, K., Borgani, S., Murante, G., & Springel, V. 2009, MNRAS, 399, 497

D'Onghia, E., & Lake, G. 2004, ApJ, 612, 628

D'Onghia, E., Sommer-Larsen, J., Romeo, A. D., et al. 2005, ApJ, 630, L109

Eckmiller, H. J., Hudson, D. S., & Reiprich, T. H. 2011, A&A, 535, A105

Eigenthaler, P., & Zeilinger, W. W. 2012, A&A, 540, A134

—. 2013, A&A, 553, A99

Genel, S., Vogelsberger, M., Springel, V., et al. 2014, MNRAS, 445, 175

Girardi, M., Aguerri, J. A. L., De Grandi, S., et al. 2014, A&A, 565, A115

Gozaliasl, G., Khosroshahi, H. G., Dariush, A. A., et al. 2014, A&A, 571, A49

Harrison, C. D., Miller, C. J., Richards, J. W., et al. 2012, ApJ, 752, 12

Hess, K. M., Wilcots, E. M., & Hartwick, V. L. 2012, AJ, 144, 48

Hinshaw, G., Larson, D., Komatsu, E., et al. 2013, ApJS, 208, 19

Jones, L. R., Ponman, T. J., & Forbes, D. A. 2000, MNRAS, 312, 139

Jones, L. R., Ponman, T. J., Horton, A., et al. 2003, MNRAS, 343, 627

Jung, I., Lee, J., & Yi, S. K. 2014, ApJ, 794, 74

Kanagusuku, M. J., Díaz-Giménez, E., & Zandivarez, A. 2016, A&A, 586, A40

Katz, N., & White, S. D. M. 1993, ApJ, 412, 455

Khosroshahi, H. G., Gozaliasl, G., Rasmussen, J., et al. 2014, MNRAS, 443, 318

Khosroshahi, H. G., Jones, L. R., & Ponman, T. J. 2004, MNRAS, 349, 1240

Khosroshahi, H. G., Maughan, B. J., Ponman, T. J., & Jones, L. R. 2006, MNRAS, 369, 1211

Khosroshahi, H. G., Ponman, T. J., & Jones, L. R. 2007, MNRAS, 377, 595

Kundert, A., Gastaldello, F., D'Onghia, E., et al. 2015, MNRAS, 454, 161

La Barbera, F., de Carvalho, R. R., de la Rosa, I. G., et al. 2009, AJ, 137, 3942

Li, Y., Mo, H. J., & Gao, L. 2008, MNRAS, 389, 1419

Mendes de Oliveira, C. L., Cypriano, E. S., & Sodré, Jr., L. 2006, AJ, 131, 158

Méndez-Abreu, J., Aguerri, J. A. L., Barrena, R., et al. 2012, A&A, 537, A25

Miller, E. D., Rykoff, E. S., Dupke, R. A., et al. 2012, ApJ, 747, 94

Milosavljević, M., Miller, C. J., Furlanetto, S. R., & Cooray, A. 2006, ApJ, 637, L9

Nelson, D., Pillepich, A., Genel, S., et al. 2015, ArXiv e-prints, arXiv:1504.00362

Neto, A. F., Gao, L., Bett, P., et al. 2007, MNRAS, 381, 1450

Pierini, D., Giodini, S., Finoguenov, A., et al. 2011, MNRAS, 417, 2927

Pillepich, A., Springel, V., Nelson, D., et al. 2017, ArXiv e-prints, arXiv:1703.02970

Ponman, T. J., Allan, D. J., Jones, L. R., et al. 1994, Nature, 369, 462

Pratt, G. W., Pointecouteau, E., Arnaud, M., & van der Burg, R. F. J. 2016, A&A, 590, L1

Proctor, R. N., de Oliveira, C. M., Dupke, R., et al. 2011, MNRAS, 418, 2054

Proctor, R. N., Mendes de Oliveira, C., & Eigenthaler, P. 2014, MNRAS, 439, 2281

Raouf, M., Khosroshahi, H. G., & Dariush, A. 2016, ApJ, 824, 140

Raouf, M., Khosroshahi, H. G., Ponman, T. J., et al. 2014, MNRAS, 442, 1578

Rodriguez-Gomez, V., Genel, S., Vogelsberger, M., et al. 2015, MNRAS, 449, 49

Rodriguez-Gomez, V., Pillepich, A., Sales, L. V., et al. 2016, MNRAS, 458, 2371

Springel, V. 2010, MNRAS, 401, 791

Springel, V., White, S. D. M., Tormen, G., & Kauffmann, G. 2001, MNRAS, 328, 726

Sun, M., Forman, W., Vikhlinin, A., et al. 2004, ApJ, 612, 805

Trevisan, M., Mamon, G. A., & Khosroshahi, H. G. 2017, MNRAS, 464, 4593

Ulmer, M. P., Adami, C., Covone, G., et al. 2005, ApJ, 624, 124

Voevodkin, A., Borozdin, K., Heitmann, K., et al. 2010, ApJ, 708, 1376

Vogelsberger, M., Genel, S., Sijacki, D., et al. 2013, MNRAS, 436, 3031

Vogelsberger, M., Genel, S., Springel, V., et al. 2014, MNRAS, 444, 1518

von Benda-Beckmann, A. M., D'Onghia, E., Gottlöber, S., et al. 2008, MNRAS, 386, 2345

Zarattini, S., Barrena, R., Girardi, M., et al. 2014, A&A, 565, A116

Zarattini, S., Aguerri, J. A. L., Sánchez-Janssen, R., et al. 2015, A&A, 581, A16

Zarattini, S., Girardi, M., Aguerri, J. A. L., et al. 2016, A&A, 586, A63

# Chapter 4

# Mass profiles of fossil galaxy systems in the *Chandra* archive: a mass modeling analysis of RX J1159.8+5531

# Abstract

The characteristic extreme magnitude gap between a fossil group's central galaxy and brightest satellite galaxy has been proposed to indicate fossil groups collapsed early. This would allow enough time for massive satellites to merge with the central galaxy and would suggest fossil groups have since been passively evolving to the present. We aim to test this relaxed and early forming origin scenario by examining the properties of fossil systems with archival *Chandra* observations. Here we present the analysis of the first system in this archival sample, RX J1159.8+5531. For this fossil system we measure radial profiles of intracluster medium temperature and gas density. The total mass profile is constructed out to $R_{500}$ using a surface brightness determined gas density profile and a spectral analysis determined temperature profile, along with optical constraints on the stellar mass profile of the massive central galaxy of the system. We find RX J1159.8+5531 shows relaxed properties such as a cool core and smooth X-ray isophotes centered on the central galaxy. From our mass modeling analysis, we find this system has a total mass of $M_{\rm tot,500} = 6.69^{+0.45}_{-0.42} * 10^{13} M_{\odot}$ and is described by a mass profile with a concentration parameter of $c_{500} = 5.4^{+0.47}_{-0.48}$. From these values we find the dark matter halo of RX J1159.8+5531 is more concentrated than expected for its mass in comparison to halos in simulations. This suggests RX J1159.8+5531 is indeed an example of a relaxed and early-forming fossil system.

## 4.1 Introduction

Fossil galaxy systems are groups and clusters with more than a two magnitude gap in brightness between their central galaxy and brightest satellite galaxy within half the virial radius (Jones et al. 2003). The very luminous fossil central galaxy and lack of bright satellite galaxies has been interpreted to form as the result of massive satellite galaxies merging with the central galaxy due to dynamical friction (Barnes 1989; Ponman et al. 1994). Various origin scenarios have been proposed to explain the features of fossil systems such as an early formation time, a transient relaxed stage, or an unusual mass assembly history.

The first observations of a sample of fossil groups found these systems showed relaxed X-ray isophotes, indicating no recent group scale mergers, as well as no signs of disturbed features or star formation occurring for the central galaxies, indicating the last major merger with the central galaxies occurred long ago (Jones et al. 2003). These features were interpreted to suggest fossils assembled their mass at early times, and at the present are old and evolved systems representing the end stage of galaxy evolution. Studies of the Millennium simulation have indeed shown fossils have a greater probability for assembling half of their final $z = 0$ mass at higher redshifts than non-fossil systems (Dariush et al. 2007, 2010).

Fossils may also only be a transient relaxed stage in the mass assembly of a group (von Benda-Beckmann et al. 2008; Kanagusuku et al. 2016; Kundert et al. 2017). In this scenario, the magnitude gap of present day fossils has formed a few Gyr ago as the result of both mergers of satellites with the central and lack of recent group-scale mergers to replenish the satellite population; while, on the other hand, the magnitude gap of fossils

identified at higher redshifts has been filled in from recent satellite infall by the present.

It is also possible some fossils, in particular fossil clusters, have formed from mergers of poor galaxy systems or lower mass fossil groups (Harrison et al. 2012). For example, the merger of a fossil group with a poor cluster will likely produce a fossil cluster (Schirmer et al. 2010). As another example, the Cheshire Cat lensing system represents the ongoing merging between two fossil groups, and when the central galaxies of these groups merge in a Gyr, the Cheshire Cat will become a fossil cluster (Irwin et al. 2015).

One observational tool to understand the mass assembly history of a galaxy system is through the mass concentration parameter of its dark matter halo profile (Navarro et al. 1996, 1997). The concentration of a halo is set at the time of the halo's collapse (Navarro et al. 1997; Wechsler et al. 2002). This produces a relation between concentration and mass where low mass halos have a higher concentration from assembly at earlier times than more massive halos which are less concentrated and assemble at later times. Furthermore, at a given halo mass, more concentrated halos have collapsed earlier (Neto et al. 2007).

The concentration parameter is thus a useful tool to compare the relative formation times of observed galaxy systems and offers a method to test the origin scenario by which fossil systems form. In this paper we measure the mass profile and mass concentration parameter of the fossil system RX J1159.8+5531 using archival *Chandra* observations. In Section 4.2, intracluster medium density and temperature profiles are determined using imaging and spectral data. The mass profile modeling process is described in Section 4.3 and the concentration parameter of RX J1159.8+5531 is discussed in Section 4.4.

Table 4.1 : RX J1159.8+5531 observation properties

| Cluster | ObsID | Instrument | Exposure [ks] | RA* | DEC* | z |
|---|---|---|---|---|---|---|
| RX J1159.8+5531 | 4964 | ACIS-S | 75.11 | 11:59:52.171 | +55:32:05.68 | 0.0809 |

* Cluster central X-ray coordinates as determined through soft-band imaging analysis (Sec. 4.2.2)

## 4.2 Data analysis

### 4.2.1 Data processing and calibration

RX J1159.8+5531 was identified as a fossil system in the catalog of Voevodkin et al. (2010). This group has an associated archival *Chandra* observation taken in February 2004 with an ACIS-S3 pointing. In Table 4.1 we show general information about this observation.

After downloading the archival observation for RX J1159.8+5531, event files were re-processed with `chandra_repro` according to the default settings with VFAINT background cleaning taken into account.

Point sources were identified for the full chip array by applying `wavdetect` to a broad-band 0.5-7 keV image with a corresponding PSF map constructed with `mkpsfmap` at an effective energy of 2.3 keV and encircled-energy fraction of 0.393. Two point sources were detected at the center of RX J1159.8+5531. However, these central point sources were not identified with `wavdetect` using a 5-10 keV image, and the spectra of these point sources were individually analyzed and found to be well described by a thermal plasma model. With this justification these central identified point sources were retained in the data analysis.

The light curve for this observation was extracted in the 0.5-7 keV range from a source and point-source free region on the S1 chip. Flares were identified and removed with `deflare` using three sigma clipping. Cleaned event files were then extracted for the full chip array using the good time intervals from the light curve and these event files were

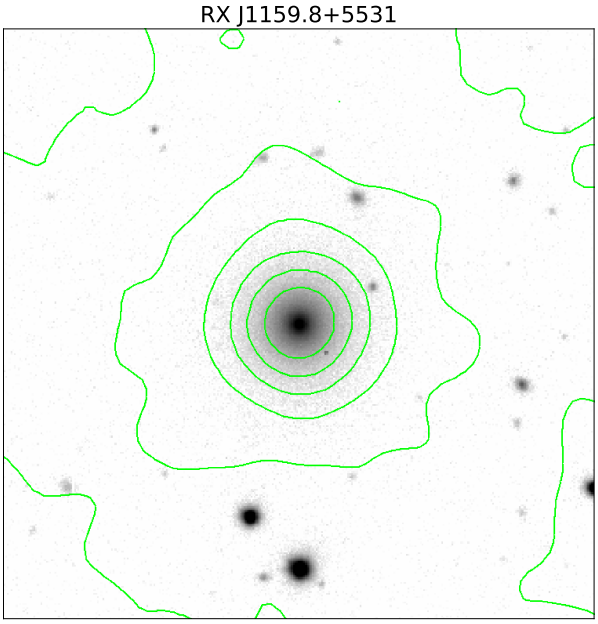


**Figure 4.1** : The inner $< 100$ kpc cluster core of RX J1159.8+5531 with X-ray contours over an optical SDSS $r$-band image. Contours have been determined from a 0.5-2 keV *Chandra* image of the cluster after removing point sources, correcting for exposure, and smoothing with a Gaussian of kernel radius $\sim 5$ arcsec.

used for the remainder of the analysis.

### 4.2.2 Imaging analysis

In Fig. 4.1, we show X-ray contours overlaid on an $r$-band optical image of the cluster core within 100 kpc of the bright central galaxy. The optical data was taken from Sloan Digital Sky Survey (SDSS) Data Release 12 (Alam et al. 2015). The X-ray contours were produced from a *Chandra* data image extracted in the 0.5-2 keV band that has been exposure corrected, interpolated after point sources removed, and using `aconvolve` smoothed with a Gaussian of 10 pixels ($\sim$ 5 arcsec). We find RX J1159.8+5531 shows relaxed X-ray emission centered on the central galaxy. The X-ray peak in this smoothed soft band image is recorded in Table 4.1.

### 4.2.3 Spectral analysis

To perform a radial profile analysis of RX J1159.8+5531, we began by identifying concentric annular regions with $\sim$ 2000 source counts in the 0.5-7 keV regime centered on the coordinates of peak surface brightness on the S3 chip. For the purpose of the creation of these regions, source counts were estimated by subtracting a CIAO `blanksky` background image re-scaled to match the counts of our target observation in the 9-12 keV band which provides a good estimate of the particle background. To extend our profile analysis out to $R_{500}$, we also placed an annulus with partial azimuthal coverage on the neighboring S2 chip. In total we created 9 regions, as shown in Fig. 4.2, that were used for our radial spectral analysis.

For each established annular region, we extracted both a source spectrum and a corresponding stowed background spectrum. All extracted spectra were grouped into bins of 20 counts. A weighted ARF and RMF for each annular region were produced with `specextract`.

The photons in each annular region consist of emission from the intracluster medium (ICM), X-ray photon background, and particle background. The contribution of all of these emission components in each annulus were determined through modeling in XSPEC.

#### 4.2.3.1 ICM model

The ICM of the cluster was modeled as an absorbed thermal plasma: $wabs \times apec_{\rm ICM}$. The neutral hydrogen column density parameter in *wabs* was set to the weighted average value as determined by the LAB Survey (Kalberla et al. 2005) towards the coordinates of the source (Table 4.1). For the $apec_{\rm ICM}$ model, the abundance, temperature, and normalization were left as free parameters to be fit.

#### 4.2.3.2 Photon background model

The X-ray photon background consists of emission from the local hot bubble (LHB), Milky Way halo (MWH), and the cosmic X-ray background (CXB). The combined model of these components was modeled as: $apec_{\rm LHB} + wabs(\ apec_{\rm MWH} + powerlaw_{\rm CXB}\ )$. For the $apec_{\rm LHB}$ and $apec_{\rm MWH}$ components, we fix the abundance $Z = 1Z_{\odot}$ and redshift $z = 0$. The temperature of $apec_{\rm LHB}$ was fixed to 0.1 keV and the temperature of $apec_{\rm MWH}$ was frozen

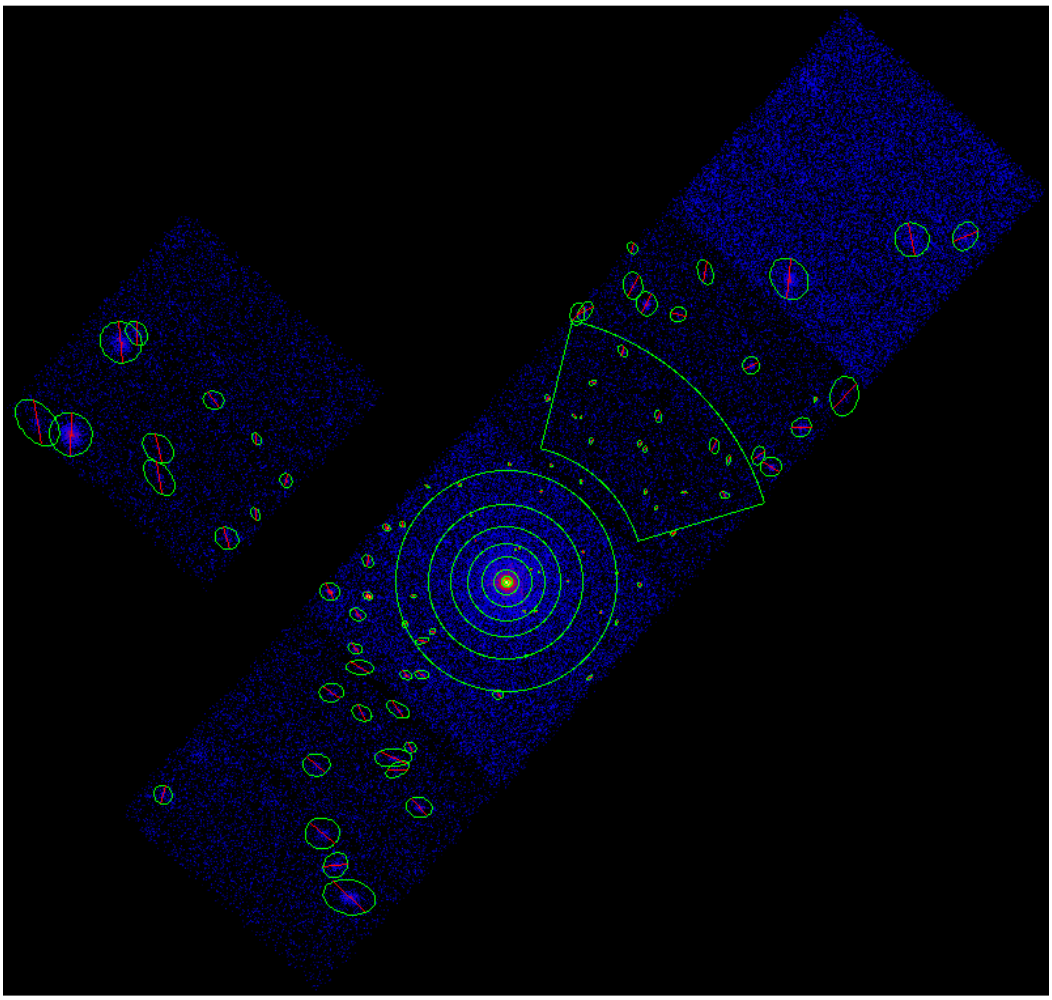

**Figure 4.2** : Placement of spectral analysis regions on the full observed chip array. Excluded point sources are also shown.

at 0.25 keV. For the $powerlaw_{\rm CXB}$ component, we fixed $\Gamma = 1.412$. The normalizations of the components of this background model were left free, but tied by an area scaling factor between annuli.

#### 4.2.3.3 Particle background model

The particle background was constrained using the stowed background observations available in the CALDB. Stowed data sets are available in three epochs - we used the epoch corresponding to the date closest to when the source observation was taken.

The stowed data sets were reprocessed and reprojected to match the event files of the observations. Spectra were then extracted from the reprojected stowed data sets in the same region as the annular regions in the original data. The stowed spectra were modeled with a broken powerlaw to account for the particle background, and two gaussians centered on 1.77 keV and ∼2.2 keV, with line widths fixed to 0, to account for the instrumental background (Humphrey & Buote 2006). The stowed spectra were not convolved with the ARF.

#### 4.2.3.4 Fitting and deprojection

The spectra of all annuli were fit simultaneously using XSPEC. Particle background model parameters were linked between the source and stowed spectra for a given annulus, but independent of other annuli. The photon background normalizations were tied by an area scaling factor for all annuli. All $apec_{\rm ICM}$ free parameters were initially left independent of other annuli, but the abundance parameter was frozen or linked to a neighboring annulus if it could not be constrained.

After the best-fitting projected source model parameter values were found, the XSPEC `deprojct` mixing model was applied to the ICM model to fit for the deprojected

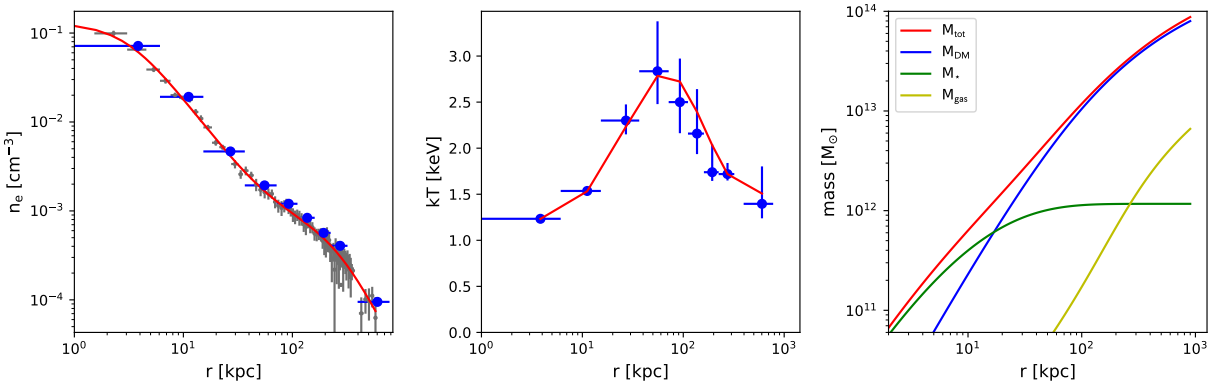


**Figure 4.3** : *Left*: Deprojected electron number density profile. $n_e$ values were determined from the spectral analysis (blue points) and from a conversion of surface brightness counts to density (grey points). The red line shows the best fitting model. *Middle*: Deprojected temperature profile. Blue points show the observed temperature profile measured from spectral analysis. The red line shows the non-parametric model temperature resulting from our mass modeling procedure. *Right*: Final estimate of the total mass profile of the cluster (red), showing the contributions of DM (blue), stars (green), and gas (yellow).

values of $apec_{\rm ICM}$ temperature, metal abundance, and normalization. The resulting deprojected gas density and temperature profiles are shown in Fig. 4.3.

### 4.2.4 Gas density profile

#### 4.2.4.1 Surface brightness counts to gas density

We constructed a gas density profile from the surface brightness counts of the cluster image in addition to determining a density profile from our spectral analysis. The gas density profile calculated from surface brightness enabled us to produce a profile with many more bins than were possible than with determining density through only the spectral analysis.

Our surface brightness profile was determined using an image of the cluster extracted in the 0.5-2 keV band, which is ideal for maximizing the counts from the cluster ICM compared to the background. For our background image, we used the `blanksky` image

appropriate for the observation of the cluster. The `blanksky` image was normalized to the count rate of the cluster image in the 9-12 keV band and then extracted in the 0.5-2 keV band. As a check we confirmed the background flux of our scaled `blanksky` background image was consistent with the background flux of our photon and particle background models determined in the spectral analysis.

Using `PROFFIT` (Eckert et al. 2011), a vignetting corrected surface brightness profile for the cluster image was calculated. A background surface brightness profile from the background image was subtracted from the source profile to return the surface brightness profile of the cluster ICM, which was then grouped such that each bin had 200 counts.

The ICM surface brightness profile was deprojected following the onion-peeling method of Kriss et al. (1983) to produce a volume emission density profile. To turn the volume emission density profile into electron density, we computed a scaling factor from the normalization of our spectral analysis $apec_{\rm ICM}$ model to a count rate. This conversion factor was computed for each bin of our spectral analysis, and then applied to the corresponding volume emission data points contained within the same radial bin. In this way we consider the effects of temperature and metal abundance gradients on the emission measure which can be important in the group mass regime.

#### 4.2.4.2 Fitting the gas density profile

We fit four different models to the density profile derived from surface brightness:

- beta model (Cavaliere & Fusco-Femiano 1976, 1978):

$$n_e = n_{e,0}\ (1 + (r/r_c)^2)^{-\frac{3}{2}\beta} \tag{4.1}$$

- cusped beta model (Humphrey et al. 2009):

$$n_e = n_{e,0}\ (r/r_c)^{-\alpha}\ (1 + (r/r_c)^2)^{-\frac{3}{2}\beta + \frac{1}{2}\alpha} \tag{4.2}$$

- double beta model:

$$n_e = n_{e,1}(n_{e,0,1}, r_{c,1}, \beta_1) + n_{e,2}(n_{e,0,2}, r_{c,2}, \beta_2) \tag{4.3}$$

- tied double beta model where $\beta_1 = \beta_2$:

$$n_e = n_{e,1}(n_{e,0,1}, r_{c,1}, \beta) + n_{e,2}(n_{e,0,2}, r_{c,2}, \beta) \tag{4.4}$$

We utilized the python `sherpa` package (Freeman et al. 2001; Doe et al. 2007) to fit Eqs. 4.1- 4.4 using the Levenberg-Marquardt $\chi^2$ minimization procedure. The best-fitting model was then selected by the model producing the lowest $\chi^2_r$ with fully constrained parameters.

The parameters of the resulting best-fit model to the deprojected gas density profile are recorded in Table 4.2. In Fig. 4.3 we show the density profile derived from the spectral analysis (blue points), the density profile derived from the surface brightness analysis (grey points), and the best-fitting model to the density profile derived from the surface brightness analysis (red line).

Table 4.2 : Gas density model

| Cluster | Model | $n_{e,0,1}$ [$10^{-1}$ cm$^{-3}$] | $r_{c,1}$ [kpc] | $\beta_1$ | $n_{e,0,2}$ [$10^{-3}$ cm$^{-3}$] | $r_{c,2}$ [kpc] | $\beta_2$ | $\chi^2$/dof ($\chi^2_r$) |
|---|---|---|---|---|---|---|---|---|
| RXJ1159 | Eq. 4.3 | $1.30^{+0.11}_{-0.10}$ | $3.17^{+0.33}_{-0.28}$ | $0.56^{+0.03}_{-0.02}$ | $0.67^{+0.17}_{-0.09}$ | $267^{+29}_{-94}$ | $0.96^{+1.05}_{-0.31}$ | 43.2/70(0.62) |

## 4.3 Mass modeling

### 4.3.1 The temperature model

The total mass profile of RX J1159.8+5531 was determined using the backwards fitting, semi-parametric, mass modeling method described in Ettori et al. (2013). This method solves for the free-parameters of the total mass profile by estimating a non-

parametric model for the observed temperature profile. This method relies on first assuming hydrostatic equilibrium:

$$\frac{d[n_{\rm gas}(r)\ kT(r)]}{dr} = \frac{-G\ M_{\rm grav}(r)}{r^2}(\mu m_p n_{\rm gas}(r)) \tag{4.5}$$

which is then solved for temperature at some radius $r$ :

$$kT(r) = \frac{kT(R_{\rm ref})\ n_e(R_{\rm ref})}{n_e(r)} - \frac{\mu m_p G}{n_e(r)} \int_{R_{\rm ref}}^{r} \frac{n_e(r')M_{\rm grav}(r')}{r'^2} dr' \tag{4.6}$$

For the total mean molecular weight $\mu$, we assume the ICM is fully ionized with cosmic abundance levels of hydrogen X=0.75 and helium Y=0.25, which results in a value of $\mu = 0.6$.

The reference radius $R_{\rm ref}$ can nominally be selected from any of the radial positions in our spectral analysis profile of the cluster; however, in practice the reference radius is typically selected to be the outermost point of the spectral profile (e.g., Ettori et al. (2010)). For RX J1159.8+5531 our spectral analysis profile extends beyond the source chip (S3) to the neighboring S2 chip. Since the error bars for the temperature determined in this annulus are large, we define our reference radius to be the outermost annulus on the source chip S3. $kT(R_{\rm ref})$ corresponds to the measured deprojected temperature value at $R_{\rm ref}$ from our spectral analysis profile, and $n_e(R_{\rm ref})$ corresponds to our value of the deprojected gas density profile at $R_{\rm ref}$.

Solving for $kT(r)$, then requires two parametric models: a model for the electron number density $n_e(r)$, and a model for the total enclosed gravitating mass $M_{\rm grav}(r)$. The model for the electron number density was taken as the best-fitting model fit to the deprojected $n_e$ profile derived from surface brightness counts as described in Sec. 4.2.4 and with parameters included in Table 4.2. In Sec. 4.3.2 we describe our model for $M_{\rm grav}(r)$.

### 4.3.2 The total gravitating mass model

Our model for a cluster's total gravitating mass profile consists of the sum of the cluster's dark matter halo, stellar mass of the cluster's central galaxy, and gas mass of the ICM:

$$M_{\rm grav}(r) = M_{\rm DM}(r) + M_{\star}(r) + M_{\rm gas}(r) \tag{4.7}$$

#### 4.3.2.1 Dark matter mass profile

The contribution of the cluster's dark matter halo to the total gravitating mass was modeled with the NFW profile (Navarro et al. 1997):

$$\begin{aligned} M_{\rm DM}(r) &= 4\pi\ \rho_{\rm crit}(z)\ \delta_{\rm char}(c)\ R_s^3 \\ &* \left[\ln(1+(r/R_s)) - \frac{r/R_s}{1+(r/R_s)}\right] \end{aligned} \tag{4.8}$$

where

$$\delta_{\rm char}(c_\Delta) = \frac{\Delta}{3}\frac{c_\Delta^3}{\ln(1+c_\Delta) - c_\Delta/(1+c_\Delta)} \tag{4.9}$$

Here $\Delta$ refers to the overdensity of the halo such that within a radius $R_\Delta$, the mean density of the halo corresponds to $\rho(R_\Delta) = \Delta\rho_{\rm crit}(z)$ where $\rho_{\rm crit}(z)$ is the critical density of the universe at the redshift of the cluster (Mo et al. 2010). The free-parameters of the NFW profile, the mass concentration parameter $c_\Delta$ and the scale radius $R_s$, remain to be returned from our fit for the total mass profile.

#### 4.3.2.2 Stellar mass profile

We also consider the contribution to the total gravitating mass from the stellar mass of the central galaxy. The stellar mass density of the BCG was modeled using a deprojected

form of the Sersic profile (Lima Neto et al. 1999):

$$\rho_\star(r) = \rho_{\star,0} \left(\frac{r}{a}\right)^{-p} \exp\left[-\left(\frac{r}{a}\right)^{1/n}\right] \tag{4.10}$$

where $p(n) = 1 - 0.6097n^{-1} + 0.05463n^{-2}$ and $a(R_e, n) = R_e \exp[n(\ln(n^{-1}) - 0.695) + 0.1789]$. From Eq. 4.10, the resulting stellar mass profile of the BCG is expressed as:

$$M_*(r) = 4\pi\ n\ \rho_{\star,0}\ a^3\ \gamma\left[(3-p)n, \left(\frac{r}{a}\right)^{1/n}\right] \tag{4.11}$$

where $\gamma$ is the lower incomplete gamma function.

The parameters of the stellar mass profile include the effective radius $R_e$, the Sersic index $n$, and the normalization of the stellar mass density profile $\rho_{\star,0}$. The values of the BCG $R_e$ and $n$, recorded in Table 4.3, were collected from the Simard et al. (2011) pure Sersic decomposition analysis of galaxies observed in SDSS DR7 (Abazajian et al. 2009). For the normalization $\rho_{\star,0}$, we allow this to be a free-parameter in our fit for the total mass profile of the cluster.

Table 4.3 : Central galaxy properties

| Cluster | BCG | $R_e$ [kpc] | n |
|---|---|---|---|
| RX J1159.8+5531 | SDSS J115952.16+553205.5 | 11.72 | 2.6 |

Notes: Effective radius $R_e$ and Sersic index $n$ are collected from the Simard et al. (2011) pure Sersic decomposition of galaxies in SDSS.

#### 4.3.2.3 Gas mass profile

The profile used to describe the distribution of ICM mass directly follows from integrating the gas density profile over a spherical volume:

$$M_{\rm gas} = \int 4\pi r^2 \rho_{\rm gas}(r)\ dr \tag{4.12}$$

We implement the analytic forms of the integrated gas models as follows:

- beta model

$$M_{\rm gas}(r) = \frac{4}{3}\pi r^3 n_{e,0} * {}_2F_1\left[\frac{3}{2}, \frac{3}{2}\beta; \frac{5}{2}; -\left(\frac{r}{R_c}\right)^2\right] \tag{4.13}$$

- cusped beta model

$$\begin{aligned} M_{\rm gas}(r) = \frac{4}{\alpha - 3}\pi r^3 * n_{e,0} * \left(\frac{r}{R_c}\right)^{-\alpha} \\ * {}_2F_1\left[\frac{3-\alpha}{2}, \frac{3}{2}\beta_1; 1 + \frac{3-\alpha}{2}; -\left(\frac{r}{R_{c,1}}\right)^2\right] \end{aligned} \tag{4.14}$$

- double beta model

$$\begin{aligned} M_{\rm gas}(r) = \frac{4}{3}\pi r^3 * \Bigg( n_{e,0,1} * {}_2F_1\left[\frac{3}{2}; \frac{3}{2}\beta_1, \frac{5}{2}; -\left(\frac{r}{R_{c,1}}\right)^2\right] \\ + n_{e,0,2} * {}_2F_1\left[\frac{3}{2}; \frac{3}{2}\beta_2, \frac{5}{2}; -\left(\frac{r}{R_{c,2}}\right)^2\right]\Bigg) \end{aligned} \tag{4.15}$$

- tied double beta model - which follows the same form as the double beta $M_{\rm gas}(r)$ profile, with $\beta_1 = \beta_2$

where ${}_2F_1[a, b; c; z]$ is a hypergeometric function.

### 4.3.3 MCMC

The free parameters of the model $T(r)$ profile in Eq. 4.6 come from the dependency of the model on the total gravitating mass (Eq. 4.7) and consist of the NFW concentration $c$, the NFW scale radius $R_s$, and the normalization of the Sersic stellar mass model $\rho_{\star,0}$. The fit for these parameters was performed through a Markov chain Monte Carlo (MCMC) analysis using the python package `emcee` (Foreman-Mackey et al. 2013). We use `emcee` to run the affine-invariant ensemble sampler of Goodman & Weare (2010).

For each set of unique values of ($c$, $R_s$, $\rho_{\star,0}$) at each step in the MCMC chain the modeled temperature profile was estimated by calculating $T(r)$ of Eq. 4.6 at all radial positions of our observed spectral temperature profile. The quality of the estimated temperature model for each step in the chain was then evaluated using a Gaussian log likelihood function of the form:

$$\ln(p) = -\frac{1}{2}\sum_{n}\left[\frac{(T_{\mathrm{spec},n} - T_{\mathrm{model},n})^2}{\sigma^2_{T_{\mathrm{spec},n}}} + \ln(2\pi\sigma^2_{T_{\mathrm{spec},n}})\right] \tag{4.16}$$

Uniform prior distributions were established for the model parameters with boundaries of: $1 \leq c \leq 20$, $10\mathrm{kpc} \leq R_s \leq 300\mathrm{kpc}$, and $0.1 \leq \log(\rho_{\star,0}[M_\odot/\mathrm{kpc}^3]) \leq 100$. Initial estimation of the model parameter values was obtained via a maximum likelihood analysis. Using these values, the MCMC walkers were initialized according to a Gaussian distribution ($\sigma = 10^{-4}$) centered about the maximum likelihood estimates. We run the `emcee` sampler for 150 steps with 100 walkers, and a burn-in period of 50 steps. Thus our MCMC chain makes $\sim N_{\mathrm{walkers}} * (N_{\mathrm{steps}} - N_{\mathrm{burnin}}) = 10^4$ independent samples of the posterior distribution.

To check the MCMC chain was sampling the posterior distribution without influence of the initial conditions, the autocorrelation time of each of the model parameters was calculated using `acor`. We ensure the burn-in time was at least a factor of 10 greater than the maximum autocorrelation time for the individual parameters.

The final values for the mass model parameters ($c$, $R_s$, $\rho_{\star,0}$) were calculated as the median of the MCMC sampled distribution, with $1\sigma$ confidence intervals for these parameters assessed as the 16th and 84th percentile values of the sampled distribution.

Given the mass model parameter values of ($c$, $R_s$, $\rho_{\star,0}$) at each step of the MCMC chain, we additionally compute for that step in the chain the value of $R_\Delta$, where $R_\Delta$ corresponds to the radius at which the interior total (DM+baryonic) mass density is a factor $\Delta$ times the critical density at the redshift of the cluster.

With the value for $R_\Delta$, we also then compute the values of $M_{\rm tot}(R_\Delta)$, $M_{\rm DM}(R_\Delta)$, $M_\star(R_\Delta)$, $M_{\rm gas}(R_\Delta)$. The final values and confidence intervals of these quantities are recorded in Table 4.4. For RX J1159.8+5531, our spectral analysis extends to $r_{spec} = 778$ kpc which encloses the $R_{500}$ radius for group. Thus we choose the overdensity of our mass modeling analysis to be $\Delta = 500$.

Table 4.4 : Total mass profile

| Cluster | $r_{\rm spec,out}$ [kpc] | $c_{500}$ | $R_s$ [kpc] | $\log(\rho_{\star,0})$ [$\rm M_\odot\ kpc^{-3}$] | $R_{500}$ [kpc] | $M_{500}$ [$10^{13}\rm M_\odot$] | $M_{\rm DM}(R_{500})$ [$10^{13}\rm M_\odot$] | $M_{\rm gas}(R_{500})$ [$10^{12}\rm M_\odot$] | $M_{\star,\rm BCG}(R_{500})$ [$10^{12}\rm M_\odot$] |
|---|---|---|---|---|---|---|---|---|---|
| RX J1159 | 778 | $5.4^{+0.47}_{-0.48}$ | $107^{+12}_{-10}$ | $10.8^{+0.03}_{-0.03}$ | $602^{+13}_{-13}$ | $6.69^{+0.45}_{-0.42}$ | $6.16^{+0.44}_{-0.41}$ | $4.15^{+0.11}_{-0.11}$ | $1.17^{+0.09}_{-0.08}$ |

## 4.4 Discussion

### 4.4.1 $c - M$ relation

To compare our measurements of concentration and mass for RX J1159.8+5531 we extrapolated our results from $R_{500}$, the extent of our spectral profile, to $R_{200}$ which is used more commonly in the literature for the $c - M$ relation. As noted in Coe (2010), the characteristic overdensity $\delta_{char}$ (Eq. 4.9) of a NFW halo remains the same value at e.g. ($\Delta = 500$, $c_{500}$) as for ($\Delta = 200$, $c_{200}$). This can be used to solve for a linear approximation of concentration at one overdensity in relation to another overdensity. Solving for an expression of $c_{200}$ with respect to $c_{500}$ by maintaining the constancy of $\delta_{char}$ we find the expression

$$c_{200} \sim 1.407 c_{500} + 0.377 \tag{4.17}$$

with less than 0.5% error for $2 < c_{500} < 20$. We use this expression to extrapolate the NFW profile of the dark matter halo out to estimate $c_{200}$ and $M_{200,\rm DM}$, with results recorded in Table 4.5.

In Fig. 4.4 we compare RX J1159.8+5531 to the $c_{200} - M_{200}$ relation at $z = 0$ from the simulations of Dutton & Macciò (2014) which were run with *Planck* cosmological

Table 4.5 : Extrapolated DM profile

| Cluster | $c_{200,\mathrm{DM}}$ | $R_{200,\mathrm{DM}}$ [kpc] | $M_{200,\mathrm{DM}}$ [$10^{13}\mathrm{M}_{\odot}$] |
|---|---|---|---|
| RX J1159.8+5531 | $8.0^{+0.66}_{-0.67}$ | $857^{+22}_{-21}$ | $7.73^{+0.62}_{-0.56}$ |

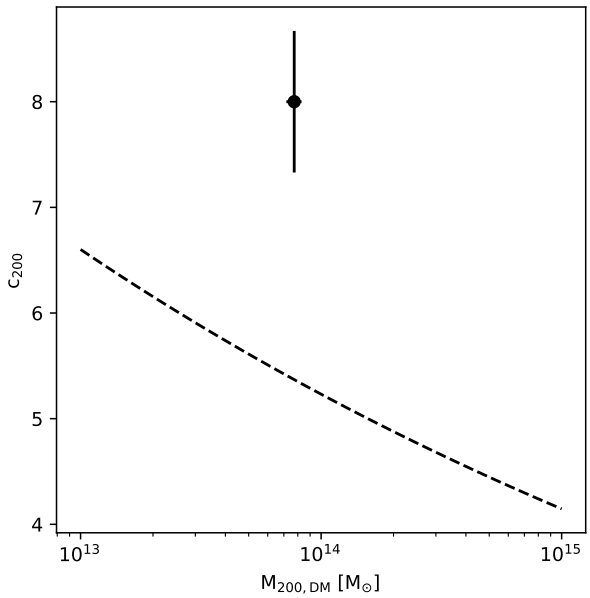


**Figure 4.4** : The concentration and mass of RX J1159.8+5531 compared to the $c - M$ relation in the simulations of Dutton & Macciò (2014).

parameters. We find RX J1159.8+5531 has a concentration placing it above the $c_{200} - M_{200}$ relation for its mass. Given the relation between concentration and formation time, the location of RX J1159.8+5531 with respect to the $c_{200} - M_{200}$ relation suggests this system has assembled its mass relatively earlier than a typical group of a similar mass.

### 4.4.2 A comparison of RX J1159.8+5531 studies

Our values of $c_{500} = 5.4^{+0.47}_{-0.48}$, $M_{500} = 6.69^{+0.45}_{-0.42} * 10^{13} M_{\odot}$ and $c_{200} = 8.0^{+0.66}_{-0.67}$, $M_{200,\mathrm{DM}} = 7.73^{+0.62}_{-0.56} * 10^{13} M_{\odot}$ determined using the semi-parametric, backwards mass modeling method are consistent with other studies that have measured the mass concentration parameter of this system previously. Gastaldello et al. (2007) finds $c_{500} = 5.6 \pm 1.5$ using the same *Chandra* archival observation data and solving for the mass profile using the forward fitting

parametric method. Humphrey et al. (2012) and Buote et al. (2016) both combine *Chandra* data in the central region of the cluster with *Suzaku* data in the outer regions and find mass concentration values of $c_{500} = 5.75 \pm 1.15$ and $c_{200} = 8.4 \pm 1.0$ respectively by solving the equation of hydrostatic equilibrium using expressions for entropy and pressure and applying the forward fitting process. Despite the variation in methods used to determine the mass profile of RX J1159.8+5531, our study and past studies are in good agreement.

Our study of RX J1159.8+5531 adds to the literature in that we have developed our own software to perform the backwards mass modeling routine and we have made our software publicly available under the name `bmpmod`[1]. This software is the first publicly available mass modeling code for X-ray observations of galaxy systems. Furthermore, we implement a MCMC algorithm to solve for the free parameters of the total gravitating mass model which increases the efficiency overwhich parameter space can be explored over traditional implementations of a grid search used with backwards modeling.

### 4.4.3 The magnitude gap of RX J1159.8+5531

Conventionally fossils are defined as having more than a 2 magnitude gap in the $r$-band between their central galaxy and brightest satellite within half the virial radius (Jones et al. 2003). However, many fossil catalogues contain variations on this definition. RX J1159.8+5531 was identified as a fossil system in the catalog of Voevodkin et al. (2010), who find a magnitude gap $\Delta m_{12} = 2.73$ within $0.7R_{500}$. However, the magnitude gap of this system was also measured by Díaz-Giménez et al. (2008) who find $\Delta m_{12} = 1.6$ within $0.5R_{vir}$ and do not consider this system to be a traditional fossil group. Nevertheless, RX J1159.8+5531 displays a large difference in brightness between its first and second ranked galaxies that would still place this system on the extreme end of the observed magnitude

[1]https://github.com/alishakundert/bmpmod

gap distribution (see Fig. 3 of Milosavljević et al. (2006)).

## 4.5 Summary and conclusions

For fossil system RX J1159.8+5531, we have analyzed archival *Chandra* observations to measure radial profiles of ICM temperature and gas density. This system shows relaxed features such as uniform X-ray isophotes centred on the central galaxy, as well as a cool core in the temperature profile.

We calculate the total mass profile of RX J1159.8+5531 through a backwards mass modeling analysis of the temperature and gas density profiles. This system is found to have a total mass of $M_{\rm tot,500} = 6.69^{+0.45}_{-0.42} * 10^{13} M_{\odot}$ and a concentration parameter of $c_{500} = 5.4^{+0.47}_{-0.48}$. Extrapolating our results out to $R_{200}$ we find RX J1159.8+5531 has a concentration above the median expected for its mass indicating this system is relaxed and early forming.

## References


Abazajian, K. N., Adelman-McCarthy, J. K., Agüeros, M. A., et al. 2009, ApJS, 182, 543

Alam, S., Albareti, F. D., Allende Prieto, C., et al. 2015, ApJS, 219, 12

Barnes, J. E. 1989, Nature, 338, 123

Buote, D. A., Su, Y., Gastaldello, F., & Brighenti, F. 2016, ApJ, 826, 146

Cavaliere, A., & Fusco-Femiano, R. 1976, A&A, 49, 137

—. 1978, A&A, 70, 677

Coe, D. 2010, ArXiv e-prints, arXiv:1005.0411

Dariush, A., Khosroshahi, H. G., Ponman, T. J., et al. 2007, MNRAS, 382, 433

Dariush, A. A., Raychaudhury, S., Ponman, T. J., et al. 2010, MNRAS, 405, 1873

Díaz-Giménez, E., Muriel, H., & Mendes de Oliveira, C. 2008, A&A, 490, 965

Doe, S., Nguyen, D., Stawarz, C., et al. 2007, in Astronomical Society of the Pacific Conference Series, Vol. 376, Astronomical Data Analysis Software and Systems XVI, ed. R. A. Shaw, F. Hill, & D. J. Bell, 543

Dutton, A. A., & Macciò, A. V. 2014, MNRAS, 441, 3359

Eckert, D., Molendi, S., & Paltani, S. 2011, A&A, 526, A79

Ettori, S., Donnarumma, A., Pointecouteau, E., et al. 2013, Space Sci. Rev., 177, 119

Ettori, S., Gastaldello, F., Leccardi, A., et al. 2010, A&A, 524, A68

Foreman-Mackey, D., Hogg, D. W., Lang, D., & Goodman, J. 2013, PASP, 125, 306

Freeman, P., Doe, S., & Siemiginowska, A. 2001, in Society of Photo-Optical Instrumentation Engineers (SPIE) Conference Series, Vol. 4477, Astronomical Data Analysis, ed. J.-L. Starck & F. D. Murtagh, 76–87

Gastaldello, F., Buote, D. A., Humphrey, P. J., et al. 2007, ApJ, 669, 158

Goodman, J., & Weare, J. 2010, Communications in Applied Mathematics and Computational Science, Vol. 5, No. 1, p. 65-80, 2010, 5, 65

Harrison, C. D., Miller, C. J., Richards, J. W., et al. 2012, ApJ, 752, 12

Humphrey, P. J., & Buote, D. A. 2006, ApJ, 639, 136

Humphrey, P. J., Buote, D. A., Brighenti, F., et al. 2012, ApJ, 748, 11

Humphrey, P. J., Buote, D. A., Brighenti, F., Gebhardt, K., & Mathews, W. G. 2009, ApJ, 703, 1257

Irwin, J. A., Dupke, R., Carrasco, E. R., et al. 2015, ApJ, 806, 268

Jones, L. R., Ponman, T. J., Horton, A., et al. 2003, MNRAS, 343, 627

Kalberla, P. M. W., Burton, W. B., Hartmann, D., et al. 2005, A&A, 440, 775

Kanagusuku, M. J., Díaz-Giménez, E., & Zandivarez, A. 2016, A&A, 586, A40

Kriss, G. A., Cioffi, D. F., & Canizares, C. R. 1983, ApJ, 272, 439

Kundert, A., D'Onghia, E., & Aguerri, J. A. L. 2017, ApJ, 845, 45

Lima Neto, G. B., Gerbal, D., & Márquez, I. 1999, MNRAS, 309, 481

Milosavljević, M., Miller, C. J., Furlanetto, S. R., & Cooray, A. 2006, ApJ, 637, L9

Mo, H., van den Bosch, F. C., & White, S. 2010, Galaxy Formation and Evolution

Navarro, J. F., Frenk, C. S., & White, S. D. M. 1996, ApJ, 462, 563

—. 1997, ApJ, 490, 493

Neto, A. F., Gao, L., Bett, P., et al. 2007, MNRAS, 381, 1450

Ponman, T. J., Allan, D. J., Jones, L. R., et al. 1994, Nature, 369, 462

Schirmer, M., Suyu, S., Schrabback, T., et al. 2010, A&A, 514, A60

Simard, L., Mendel, J. T., Patton, D. R., Ellison, S. L., & McConnachie, A. W. 2011, ApJS, 196, 11

Voevodkin, A., Borozdin, K., Heitmann, K., et al. 2010, ApJ, 708, 1376

von Benda-Beckmann, A. M., D'Onghia, E., Gottlöber, S., et al. 2008, MNRAS, 386, 2345

Wechsler, R. H., Bullock, J. S., Primack, J. R., Kravtsov, A. V., & Dekel, A. 2002, ApJ, 568, 52

# Chapter 5

# Summary and Conclusions

Fossil groups and clusters of galaxies represent an interesting stage in hierarchical structure growth. They are characterized by an unusual luminosity function, where the central galaxy dominates the optical luminosity of the group and bright and massive satellite galaxies are missing. Understanding how fossils obtain their characteristic properties offers a window into how galaxy systems evolve. In this thesis, I have explored the properties of fossil systems using X-ray observations and simulations with the goal of constraining the nature and origin of these systems.

In Chapter 2, we measured global X-ray luminosities and ICM temperatures for a sample of fossil systems observed with *Suzaku*. These data points were used in conjunction with data from the literature to construct optical and X-ray scaling relations for the largest sample of fossil systems to date. We found no difference in the scaling relations followed by fossils in comparison to non-fossils spanning both the group and cluster mass regimes.

In Chapter 3, the mass assembly histories of groups and their central galaxies were examined in the Illustris cosmological simulation. We found fossil central galaxies experience their last major merger more recently than non-fossil central galaxies. However, no difference was found in the redshift at which fossil and non-fossil groups assemble 50% of their final total group mass which is commonly viewed as the time of halo formation. Although there was no difference in halo mass assembly at early times, a difference was found in the recent group-scale accretion histories where fossils show no significant halo mass growth over the past few Gyr.

In Chapter 4, the mass profile of the fossil group RX J1159.8+5531 was measured from archival *Chandra* observations. This fossil group was found to reside above the concentration-mass relation for dark matter halos in simulations, indicating this system is more concentrated and thus earlier forming than other halos of similar mass.

In interpreting these studies together we find evidence that some fossils indeed

assemble their mass at early times (e.g., RX J1159.8+5531), however, a substantial portion of fossils are relaxed systems, but are not necessarily earlier forming (e.g., fossils in Illustris). The mix of origin scenarios would explain the difficulties in reaching a consensus on fossil properties especially given the small sample sizes available for observational studies. While fossil galaxy systems do not appear to have a uniform origin scenario, fossils seem to be generally relaxed systems that have seen little recent interaction with their environment.